Scientific
Research
Publishing

Journal of Modern Physics

www.scirp.org/journal/jmp

Journal Editorial Board

Scientific Research Publishing

Table of Contents

Volume 10   Number 5   April 2019

Journal of Modern Physics (JMP)
Journal Information

SUBSCRIPTIONS

SERVICES

COPYRIGHT

PRODUCTION INFORMATION

Scientific
Research
Publishing

Effect of Silicon Carbide (SiC) Nanoparticles on the Spectroscopic Properties and Performance of PMMA/PC Polymer Blend

H. M. Alhusaiki-Alghamdi

Department of Physics, Faculty of Science, University of Jeddah, Jeddah, Saudi Arabia
Email: halhusiki@kau.edu.sa

Abstract

Films of polymethyl methacrylate (PMMA)/polycarbonate (PC) polymer blend doped silicon carbide (SiC) nanopowder are synthesized by the casting method. The study for the structural, optical and electrical behavior of PMMA/PC blend without and with low contents (≤0.8 wt%) of SiC is done. The change of the structure is investigated from X-ray spectra. After the addition of SiC, the intensity of the main X-ray halo peak at 2θ = 20.26° of PMMA/PC is decreased, attributed to an interaction between PMMA/PC. It's clear that SiC is causing an increase in the amorphous regions inside the PMMA/PC blend. The peaks related to SiC are not found attributed using a small amount of SiC with complete dissolution of SiC. The shift of the intensity for IR bands has supported an interaction between all components. The values of the optical band gap from UV-Vis spectra using indirect transition are decreased with the increase of SiC. The values of the electrical conductivity are low at low frequency attributed to the charge accumulation at the electrode which takes place. The conductivity is increased as the increase of frequency due to the mobility of charge carriers. Furthermore, the conductivity is increased with the increase of SiC contents. The values of ε' and ε'' are very high at the lower frequency and they decrease when the frequency is increased attributed to the effect. The plot of both Z' and Z'' shows dramatic decrease with the increase of frequency.

Keywords

PMMA/PC Blend, SiC Nanoparticles, XRD, FT-IR, Electrical Properties

1. Introduction

The blend between at least two polymers has given another direction to making

novel materials [1]. It is a basic and conservative system for altering distinctive properties of the polymers. The blend between the polymers is the technique to upgrade and improve some physical properties of the polymers [2] [3]. The blends between the polymers give a new material. This new material has a good property best than individual polymer. Polycarbonate (PC) is a thermoplastic polymer utilized of advanced applications due to their properties, for example, as strong hydrophobicity, high melt viscosity, the sensitivity of mechanical properties, and softness [4] [5]. To enhance the properties of PC blend, fillers including organic as well as inorganic nanoparticles have additionally been used in a wide range [5] [6].

The blend between polymethyl methacrylate (PMMA) and PC is one of the most profoundly examined polymer pairs and it has received considerable research consideration [7]. This fact is attributed to the transportation of PMMA as a commercial polymer and to PC as an ideal polymer choice in the industry due to its characteristics. A couple of researchers have considered the blend between PC and PMMA to utilize in both industry and research [8]. The greater part of the studies has been centered around the examination of the structure which has been found depending on the method of preparation [9] [10] [11].

Silicon carbide nanostructures have specific properties useful for applications in microelectronics and optoelectronics [12] [13] [14]. Actually, SiC has selected due to their properties as a high hardness, semiconductor processing equipment, etc. These characteristics make SiC a perfect possibility for high-power electronic devices. A lot of works are represented on SiC combination since the assembling procedure began. Optically, SiC shows weak release at room temperature by virtue of its backhanded band hole. SiC is used in a wide range as utilized as reinforcement in nanocomposites. Silicon carbide nanocomposites have different advantages as far as their performance for use as special structural materials attribute to their excellent properties [15] [16]. This is accepted to be caused by discouraged non-radiative recombination in the confined clusters. SiC nanostructures have a great wonderful property which searches useful for applications in microelectronics and optoelectronics [17].

The aim of this article is to prepare and characterize polymethyl methacrylate (PMMA) and polycarbonate (PC) polymer blend doped with 0.0, 0.2, 0.4, 0.6 and 0.8 wt.% of silicon carbide (SiC) nanoparticles. The X-ray diffraction (XRD), Fourier transform infrared (FT-IR) spectroscopy, Ultraviolet-visible (UV-Vis) spectroscopy, and AC conductivity are used to characterize and study the enhancements of the structural, optical and electrical properties of PMMA/PC blend without and with low contents of SiC.

2. Experimental Details

2.1. Materials Used

Polymethylmethacrylate (PMMA) has $M_w = 1.5 \times 10^4$ G/mole and commercial

polycarbonate (PC) has $M_w = 2.47 \times 10^4$ G/mole are used as a host material. The MMA and PC are purchased from ACROS Company (New Jersey, USA). The blend samples are synthesis by the solution casting method using chloroform as a common solvent. Silicon carbide (SiC) nanopowder, <100 nm particle size is obtained from Sigma Aldrich company.

2.2. Preparation of the Samples

The amount of both PMMA and PC are dissolved individually in chloroform using the ratio 70:30 wt%, respectively. The silicon carbide (SiC) nanopowder is dissolved and suspended in chloroform with a stirrer by an ultrasonic bath for 20 min. Finally, various concentrations of silicon carbide (0, 0.2, 0.4, 0.6 and 0.8 wt%) is added in the polymer mixture as a dopant and stirred with the sonicator further for another 20 min to confirm the distribution of SiC inside the PMMA/PC blend. The final nanocomposite solution is then cast onto a glass plate to get a nanocomposites film with uniform thickness (150 μm). The films of PMMA/PC-SiC are left to dry at 50°C about 48 h using a vacuum oven.

2.3. Characterization

The X-ray diffraction spectra are measured using a PANalytical X'Pert PROXRD with filtered CuK α-radiation (λ = 1.54056 Å) at 40 kV acceleration and 10 mA currents. The FT-IR spectra are recorded on Nicolet iS10, USA spectrometer having a resolution 4 cm^{-1} in the wavenumber from 4000 to 400 cm^{-1} to examine their structure. Ultraviolet-visible (UV-vis) absorption spectra of polymer films are recorded using (V-570 UV/VIS/NIR, JASCO) in the wavelength range 195 - 1100 nm. The AC electrical studies are done in a frequency range from 10^{-1} to 10^7 Hz, using novo-control technologies broadband dielectric spectroscopy. The possible mechanism of the interaction between the components in PMMA/PC-SiC nanocomposites. Firstly, the interaction between the two polymer is occur through the function groups and then the reaction between the polymer blend and Si$^+$ after breaking of the carboxyl group.
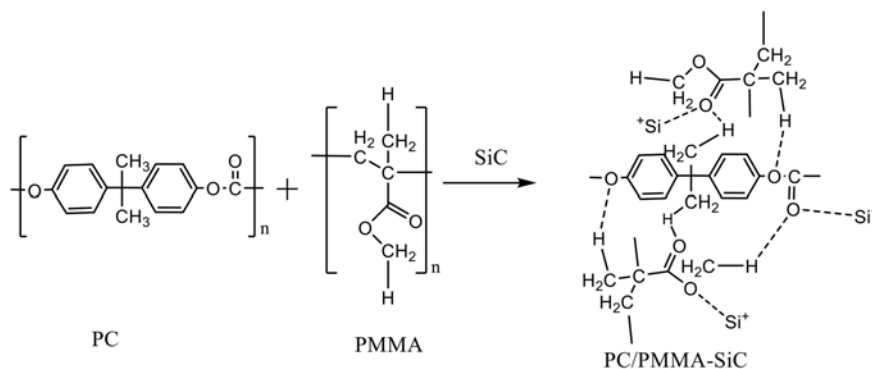
Scheme 1. The possible mechanism of the interaction between the components in PMMA/PC-SiC nanocomposites.

3. Results and Discussion

3.1. The X-Ray Diffraction Analysis

The X-ray diffraction is utilized to study the effect for different amounts (0, 0.2, 0.4, 0.6 and 0.8) of silicon carbide (SiC) on the crystalline structure of pure PMMA/PC. Figure 1 displays the X-ray diffraction for PMMA/PC without and with various concentration of SiC at $2\theta = 5°$ - $75°$. The hump (amorphous nature) is observed in the spectra around $2\theta = 16°$ is attributed to PMMA. The spectrum of pure PMMA/PC blend depicts the characteristic halo peak observed at $2\theta = 20.26°$. After addition of SiC, the intensity of this main peak is decreased and became broader attributed to an interaction between the PMMA/PC and the SiC causes a decrease in the intermolecular interaction as well as the increase of the amorphous regions between the polymeric chains. The amorphous kind of materials causes an increase of the conductivity [18]. The functional group in the blend implied a decrease in the crystallization indicates that there is a compatibility between the silicon carbide and PMMA/PC in amorphous parts in the PMMA/PC matrix. The spectrum of SiC as we see inset in Figure 1, did not observe any peaks related to SiC nanopowder attributed to uses of the small amounts of SiC are under detecting limit and/or good dissolution in amorphous phases of SiC in PMMA/PC matrices.

3.2. FT-IR Measurement

Figure 2 displays the FT-IR spectra of PMMA/PC films blend and PMMA/PC doped different concentrations of SiC nanoparticles at room temperature from 4000 to 400 cm^{-1}. The characteristic absorption bands of PMMA/PC blend are observed. The principal bands of pure PMMA are assigned as: The band at 2954 cm^{-1} is assigned to O-CH_3 bending and the bands at 1732 and 1250 cm^{-1} are assigned to stretching frequency of C = O. The bands at 1446 cm^{-1} and at 987 cm^{-1} are assigned to-CH and -CH_2 bending mode, respectively. Two characteristic bands of PMMA are observed at 1062 cm^{-1} and at 845 cm^{-1}. The main IR bands of PC is assigned as: The band sat 2991 cm^{-1} is due to -CH stretching aromatic ring and at 1770 cm^{-1} is ascribed to stretching carboxyl group (C = O). The band at 1501 cm^{-1} is assigned to C = C-vibration mode and at 1190 cm^{-1} is assigned to asymmetric stretching carbonate group (O–C–O). In general, the FT-IR analysis displays the characteristic carboxyl (C = O) stretching bands of PMMA at 1732 cm^{-1} and of PC at 1770 cm^{-1}, confirming that PMMA-PC blend has been formed [19] [20] [21].

After the addition of SiC inside the polymeric matrix of PMMA/PC blend, the intensity of some IR bands is decreased with no recognizable changes in their position occur is in comparison with the spectra of the pure blend. This suggests that the SiC is homogeneously dispersed inside the polymer blend. Likewise, this decrease happens due to weak physical forces connected between SiC and PMMA/PC than the chemical forces. The increase of SiC helps to occur the interaction between the PMMA/PC as a host material and the SiC. Then, the in-

tensity of C-O, and C–O–C groups is to a great extent limited and results in more disturbance for crystallization and an enhancement for the fraction of amorphous phases as confirmed in X-ray analysis.

3.3. UV-Vis Measurement

The UV-Vis absorption spectra of the composites in from 190 to 800 nm appeared in Figure 3. All the spectra show an appearance of two absorption bands at 241 nm and at 538 nm that corresponds to the characteristic bands of conjugated unsaturation and carbonyl chromophores, respectively ($\pi \to \pi^*$ transition from unsaturated bonds (C = O and/or C = C). The intensity of the edge decreased as increase SiC amount, confirming that responses to the reactions between all components. The decrease in the band intensity which related to C = O is attributed to the photochemical disruption of π bonds, which later causes reduction in the intensity after increase of SiC concentration due to the bonds between oxygen tom and Si^+. The electron in the π bond undergoes photo-excitation from ground to higher energy state ($\pi \to \pi^*$ transition) and cleaves the bond.
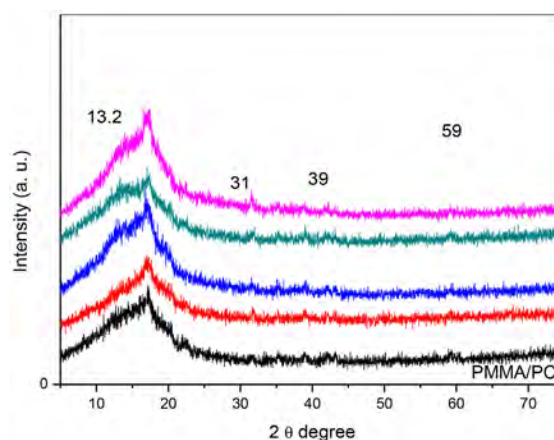
Figure 1. The X-ray diffraction of PMMA/PC doped with SiC nanopowder.
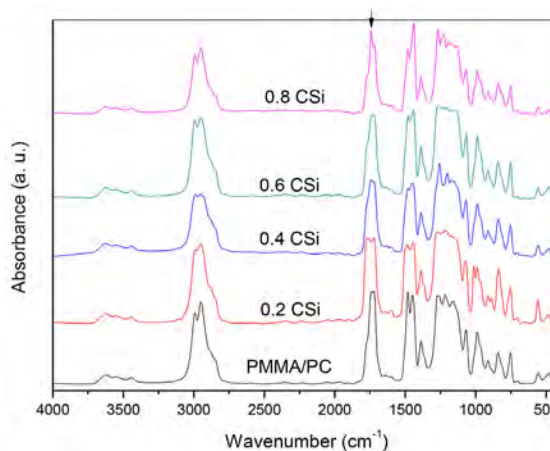
Figure 2. The FT-IR spectra for PMMA/PC doped with SiC nanopowder.
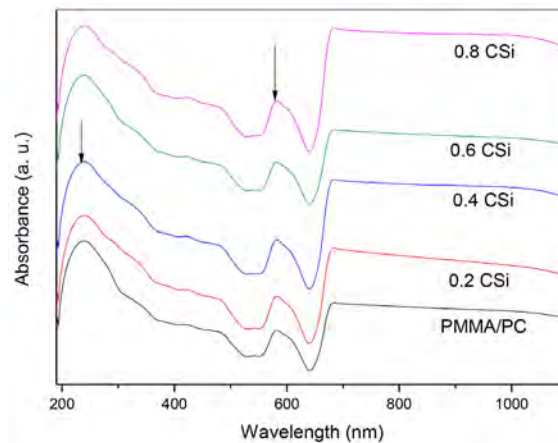
Figure 3. The UV-Vis spectra of PMMA/PC doped with SiC nanopowder.

To study the optical properties of the PMMA/PC-SiC, the optical band gap (E_g) of the prepared nanocomposites is estimated using formula (1) as [22]:

$$(\alpha h\upsilon)^x = B\left(h\upsilon + E_g\right) \tag{1}$$

where, α is the absorption coefficient, $h\upsilon$ is the photon energy (h is Planck's constant, ($\left(\upsilon = \dfrac{c}{\lambda}\right.$, c is speed of light and λ is the wavelength$\left.\right)$), B is a constant, and x = 1/2, 2, 3/2 and 3 corresponding to the allowed indirect, allowed direct, forbidden direct and forbidden indirect transitions, respectively. The values of $\alpha(\nu)$ are determined by the equation:

$$\alpha(\nu) = \frac{2.303A}{d} \tag{2}$$

where A is absorbance. At the edge, the forbidden direct of $h\nu$. The band energy (E_g) can be evaluated from the relation between $(\alpha h\nu)^{3/2}$ and of photon energy ($h\nu$) as seen in **Figure 4**. The estimations of E_g of the samples are dictated using extrapolating of the straight part of the high energy spectra to the $h\nu$-axis at zero, and these values are decreased from 3.88 eV to 3.74 eV with the increase of SiC contents in the PMMA/PC blend. This decrease is expected due to the addition of relatively low energy band gap SiC into the high energy band gap of PMMA/PC. Also, the decrease of E_g attributed to change in the structure of PMMA/PC blend attributed to formation of new bonds between the SiC with blend chains. Another reason for the decrease of E_g is the formation of localized state between HOMO and LUMO bands for PMMA/PC, which modified their extended electronic states.

3.4. The AC Electrical Studies

3.4.1. The AC Electrical Conductivity

The AC electrical conductivity $\sigma(\omega)$ study is performed to incorporate the effect of conduction mechanism and the kinds of charge carriers in the samples. The AC electrical conductivity $\sigma(\omega)$ of the common polymers is calculated using the following empirical equation [23]:
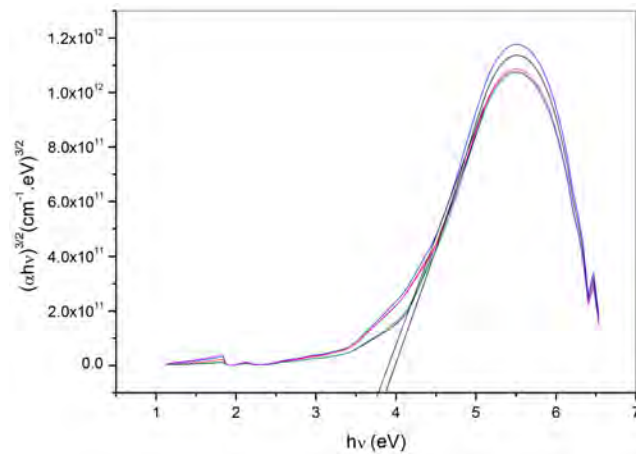
Figure 4. The variation of $(ah\nu)^{3/2}$ depends on the energy $(h\nu)$ of PMMA/PC doped with SiC nanopowder.

$$\sigma(\omega) = \omega \varepsilon_o \varepsilon'' \tag{3}$$

The conductivity of the samples is due to losses of bound charges whereas there should be no such losses under a DC field. Every material will have free charges, and under the applied low frequency, these charges can follow the field and cause conduction current given rise to energy loss. Then the measured AC conductivity is [24]:

$$\sigma_m(\omega) = \sigma_{DC} + \sigma_{AC}(\omega) \tag{4}$$

where σ_{DC} is the *DC* electrical conductivity and σ_{AC} is the true value of *AC* conductivity. **Figure 5** shows the plot between the total electrical conductivity $\sigma(\omega)$ dependence of the frequency Log (f) at room temperature. The values of conductivity are low at low frequency due to the charge accumulation at the electrode interface tacks place which reduces the conductivity. The conductivity is increased as the increase of frequency attributed to the mobility of charge carriers and the hopping of ions from the infinite cluster. As a result, the ion exchange process occurs effectively in the high-frequency region. A relaxation with hopping frequency is observed due to earlier that the conductive species in the samples is effective to the charge carriers. It is observed that the measured electrical conductivity is increased with the increase of SiC contents.

3.4.2. The Dielectric Properties

Figure 6 displays the plot between the angular frequency Log (f) with the dielectric constant (ε') and **Figure 7** illustrates the relation between plot of dielectric loss (ε'') against Log f of pure PMMA/PC blend and the PMMA/PC embedded by 0.0, 0.2, 0.4, 0.6 and 0.8 wt% of SiC nanoparticles at room temperature. The Debye equations give the complex permittivity as the following relation [25] [26]:

$$\varepsilon^* = \varepsilon' - i\varepsilon'' = \varepsilon_\infty + \frac{\varepsilon_s - \varepsilon_\infty}{1 - j\omega\tau} \tag{5}$$
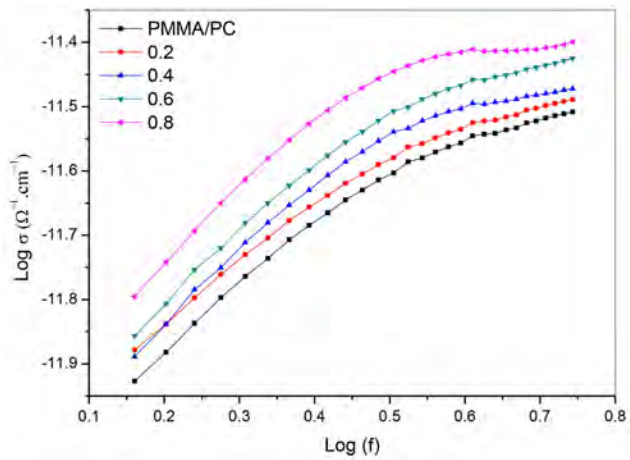
Figure 5. The variation of AC conductivity (Log σ) depends on frequency (Log f) of PMMA/PC doped with SiC nanopowder.

Figure 6. The variation of ε' depends on Log (f) of PMMA/PC doped with SiC nanopowder.

Figure 7. The variation of ε'' depends on Log (f) of PMMA/PC doped with SiC nanopowder.

where ε_∞ and ε_s are the dielectric constant at high frequency and limiting low frequency of dielectric constant, respectively, is the relaxation time $(\tau = RC)$. The real part (ε') and the imaginary part are written as [27]:

$$\varepsilon' = \varepsilon_\infty + \frac{\varepsilon_s - \varepsilon_\infty}{1 + \omega^2 \tau^2} \text{ and } \varepsilon'' = \frac{(\varepsilon_s - \varepsilon_\infty)\omega\tau}{1 + \omega^2 \tau^2} \tag{6}$$

From the two figures, it is observed that both the behavior of (ε') and (ε'') gradually decrease with the increase of the frequency and it reaches to constant values at higher frequencies. Also, the two estimated values of ε' and ε'' are very high at lower frequencies and it decreases with the increase of frequency due to because of polarization effects and because of the dipoles, not start to follow the field variety at higher frequencies. The plots of (ε') and (ε'') as shown in the figures exhibit three regions over the frequency range. In the first region at very low frequencies $(\omega \ll \tau \Rightarrow \varepsilon' = \varepsilon_s)$. Then, the dipoles flow the field and the values of (ε') and (ε'') decrease due to dominant contribution of interfacial polarization effect. The second region $\left(\omega \leq \dfrac{1}{\tau}\right)$, the dipoles begin to lag the field and the relaxation process occurs. At the last region $(\omega \ggg \tau)$, the linearity of ε' is tending to approach steady state which can be assigned to the high frequency limiting permittivity ε_∞ values of the polymers. When $\omega\tau \lll 1$, the estimated values (ε') of is equal to ε_s. Whereas the plot of (ε'') has a little decrease it becomes very low. After adding silica nanoparticles to PMMA/PC blend, the frequency is increased due to the dipole will no longer be able to rotate sufficiently rapidly and the oscillation being to be lag those of the applied field. As frequency increased, the dipole will be completely unable to follow the field and the orientation stopped and the value of ε' is decreased and approach to stable due to interfacial polarization. The decrease of ε'' with increases of the frequency may be attributed to the origin of ε'' is the conduction losses.

3.4.3. Complex Impedance Study

The collective plot of complex impedance Z^* as a function of frequency can be applied to identify whether the long-range or short-range movement of charge carriers is dominant in the relaxation process. To Interpret the dielectric spectra, different formalism such as complex impedance Z^* has been explored. The complex impedance can be evaluated from the following relation [28]:

$$Z^* = Z' + iZ'' \tag{7}$$

where Z' and Z'' are the real and imaginary part of the complex impedance, which described as [29]:

$$Z' = \frac{R}{1 + \omega^2 \tau^2} \text{ and } Z'' = \frac{\omega\tau}{1 + \omega^2 \tau^2} \tag{8}$$

Figure 8 displays the plot between the frequency Log (f) with the real complex impedance (Z') and Figure 9 illustrates the relationship between the plot of imaginary part of the complex impedance (Z'') against Log f of pure PMMA/PC

blend and the PMMA/PC embedded of SiC. As we see in the two figures, the behavior of both Z' and Z'' is gradually decreased with the increase of frequency. This behavior is a general trend of dielectrics materials as a polymer that can be understood by polarization which created related to the ionic exchange of the number of ions by locally displacing in the applied field direction. At lowest frequency, there is a charge accumulation at the interface causing contributions for various interfacial polarizations are watched. The discussion of this behavior is that at a certain point, the space charges can't support and comply with the outside field which causes a decrease in the polarization and there is no charge accumulation at the interface. At low frequencies, the real and imaginary part of the complex impedance depends to the presence of ion center type of polarization in the films and to the interfacial polarization. The complex impedance is high at the low frequency that might be because of space charge polarization. It is because obstructing of charge carriers at the electrodes due to confinement to their movement at the interface. The plots further show a decrease in impedance with the increase in silica content.
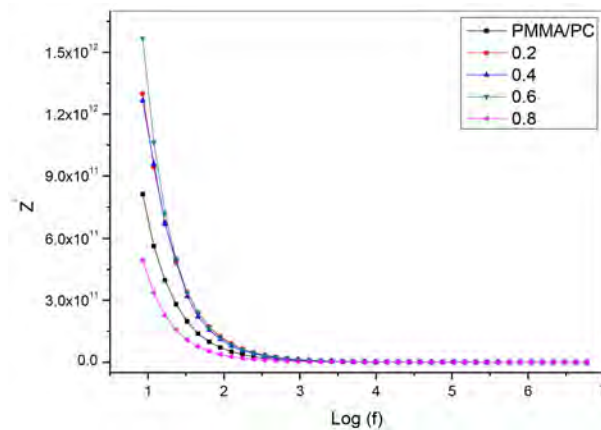
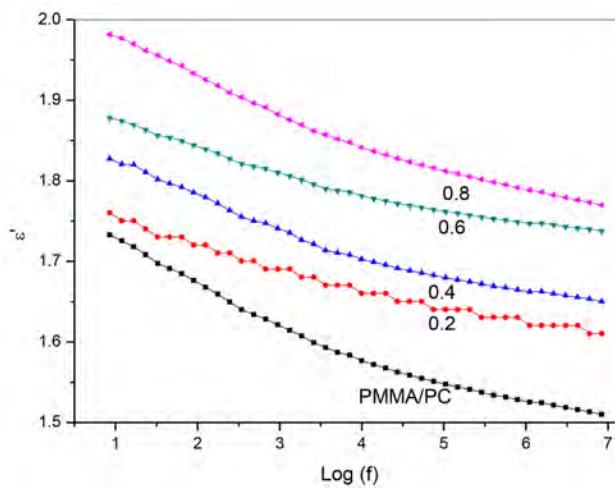**Figure 8.** The variation of Z' depends on Log (f) of PMMA/PC doped with SiC nanopowder.

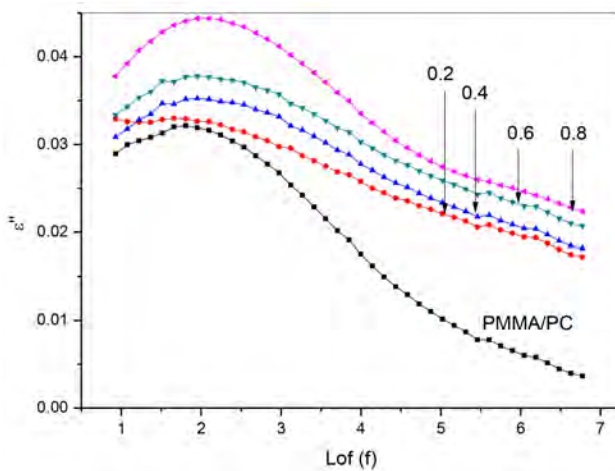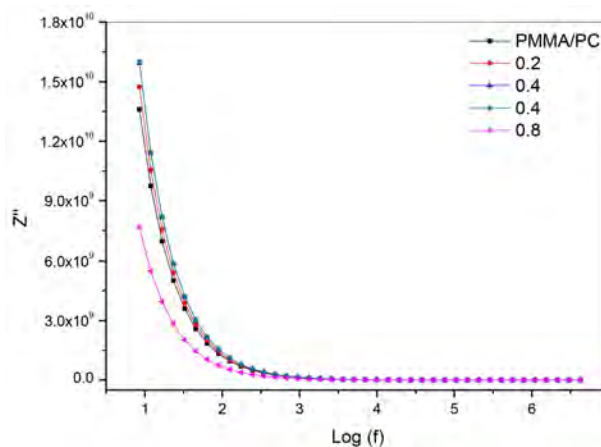**Figure 9.** The variation of Z'' depends on Log (f) of PMMA/PC doped with SiC nanopowder.

4. Conclusion

Composite samples based on PMMA/PC blend doped silicon carbide (SiC) nanoparticles are prepared and investigated. The structure of the composites is studied using X-ray, FT-IR and UV-Vis spectroscopy. The intensity of the main X-ray peak is decreased according to an interaction between PMMA/PC and SiC causing an increase in the amorphous regions. The main characteristic of X-ray peaks which assigned to SiC is not founded in all spectra attributed to use a small amount (≤0.8 wt%) of SiC or due to complete dissolution of SiC inside the polymeric matrices. The shift of intensity in IR band suggested an interaction between PMMA/PC and SiC. The values of the optical band gap from UV-Vis spectra are decreased by increasing SiC due to charge transfer. The AC conductivity is low at low frequency due to the charge accumulation at the electrode interface that takes place, which reduces the conductivity. The conductivity is increased as the increase of frequency attributed to the mobility of charge carriers and the hopping of ions from the infinite cluster. Also, the conductivity is increased with the increase of SiC contents. The values of ε' and ε'' are very high at lower frequencies and it decreases with the increase of frequency because of polarization effects and because of the dipoles, not start to follow the field variety at higher frequencies. The values of both Z' and Z'' are gradually decreased with the increase of frequency. At lowest frequency, there is a charge accumulation at the interface causing contributions for various interfacial polarizations are watched. The real and imaginary parts of the complex impedance are decreased at low frequency depends to the presence of ion center type of polarization in the films and to the interfacial polarization. The complex impedance is high at the low frequency because of space charge polarization. The plots further show a decrease in impedance with the increase in silica content.

Conflicts of Interest

The authors declare no conflicts of interest regarding the publication of this paper.

References

[1] Rajeh, A., Morsi, M.A. and Elashmawi, I.S. (2019) *Vacuum*, **159**, 430-440. https://doi.org/10.1016/j.vacuum.2018.10.066

[2] Pud, A., Ogurtsov, N., Korzhenko, A. and Shapoval, G. (2003) *Progress in Polymer Science*, **28**, 1701-1753. https://doi.org/10.1016/j.progpolymsci.2003.08.001

[3] Zivanovic, S., Li, J., Davidson, P.M. and Kit, K. (2007) *Biomacromolecules*, **8**, 1505-1510. https://doi.org/10.1021/bm061140p

[4] Malik, T.M., Carreau, P.J. and Chapleau, N. (1989) *Polymer Engineering & Science*, **29**, 600-608. https://doi.org/10.1002/pen.760290906

[5] Schauries, D., Mota-Santiago, P., Gilbert, E.P., Kirby, N., Trautmanne, C. and Kluth, P. (2018) *European Polymer Journal*, **108**, 406-411. https://doi.org/10.1016/j.eurpolymj.2018.09.025

[6] Li, Y., Pötschke, P., Pionteck, J. and Voit, B. (2018) *European Polymer Journal*, **108**, 461-471. https://doi.org/10.1016/j.eurpolymj.2018.09.027

[7] Siddiqui, N., Bhardwaj, A., Hada, R., Yadav, V.S. and Goyal, D. (2018) *Vacuum*, **153**, 6-11. https://doi.org/10.1016/j.vacuum.2018.03.036

[8] Ray, S.S. and Bousmina, M. (2005) *Macromolecular Rapid Communications*, **26**, 450-455. https://doi.org/10.1002/marc.200400586

[9] Nishimoto, M., Keskkula, H. and Pault, D.R. (1991) *Polymer*, **32**, 727.

[10] Montaudo, G., Puglisi, C. and Samperi, F. (1998) *Journal of Polymer Science Part A*: *Polymer Chemistry*, **36**, 1873-1884. https://doi.org/10.1002/(SICI)1099-0518(199808)36:11<1873::AID-POLA22>3.0.CO;2-A

[11] Penco, M., Sartore, L., Sciucca, S.D., Landro, L. D. and D'Amore, A. (2007) *Macromolecular Symposia*, **247**, 252-259. https://doi.org/10.1002/masy.200750129

[12] Hu, Z., Liao, X., Diao, H., Kong, G., Zeng, X. and Xu, Y. (2004) *Journal of Crystal Growth*, **264**, 7-12. https://doi.org/10.1016/j.jcrysgro.2003.12.013

[13] Jin, L., Zhang, K., Xu, T., Zeng, T. and Cheng, S. (2018) *Ceramics Internship*, **44**, 20992-20999. https://doi.org/10.1016/j.ceramint.2018.08.134

[14] Luo, Y., Zheng, S., Ma, S., Liu, C. and Wang, X. (2018) *Journal of the European Ceramic Society*, **38**, 5282-5293. https://doi.org/10.1016/j.jeurceramsoc.2018.08.022

[15] Wang, H., Feng, Q., Wang, Z., Zhou, H., Kan, Y., Hu, J. and Dong, S. (2017) *Corrosion Science*, **124**, 131-137. https://doi.org/10.1016/j.corsci.2017.05.016

[16] Chen, J., Jiang, M., Lin, W., Ding, L. and Xin, L. (2018) *Journal of Materials Science*, **53**, 3289-3295. https://doi.org/10.1007/s10853-017-1815-x

[17] Xie, Y., Yang, J., Chen, Y., Liu, X., Zhao, H., Yao, Y. and Cao, H. (2018) *Catalysis Today*, **315**, 223-229. https://doi.org/10.1016/j.cattod.2018.01.013

[18] Elashmawi, I.S., Alatawi, N.S. and Elsayed, N.H. (2017) *Results in Physics*, **7**, 636-640. https://doi.org/10.1016/j.rinp.2017.01.022

[19] Duan, G., Zhang, C., Li, A., Yang, X., Lu, L. and Wang, X. (2008) *Nanoscale Research Letters*, **3**, 118. https://doi.org/10.1007/s11671-008-9123-7

[20] Ghorbel, E., Hadriche, I., Casalino, G. and Masmoudi, N. (2014) *Materials*, **7**, 375-398. https://doi.org/10.3390/ma7010375

[21] Parshin, A.M., Gunyakov, V.A., Zyryanov, V.Y. and Shabanov, V.F. (2013) *International Journal of Molecular Sciences*, **14**, 16303-16320. https://doi.org/10.3390/ijms140816303

[22] Hashim, A., Ali, M. and Rabee, B.H. (2012) *American Journal of Scientific Research*, **69**, 5-9.

[23] Zulfequar, M. and Kumar, A. (1989) *Journal of the Electrochemical Society*, **136**, 1099-1102. https://doi.org/10.1149/1.2096792

[24] Farid, A.M., Atyiaand, H.E. and Hegab, N.A. (2005) *Vacuum*, **80**, 284-294. https://doi.org/10.1016/j.vacuum.2005.05.003

[25] Ray, D.K., Himanshu, A.K. and Sinha, T.P. (2005) *Indian Journal of Pure & Applied Physics*, **43**, 787-793.

[26] Turky, G., Shaaban, S.S. and Schoenhals, A. (2009) *Journal of Applied Polymer Science*, **113**, 2477-2484. https://doi.org/10.1002/app.30046

[27] Choudhary, S. and Sengwa, R.J. (2018) *Current Applied Physics*, **18**, 1041-1058.

https://doi.org/10.1016/j.cap.2018.05.023

[28] Langar, A., Sdiri, N., Elhouichet, H. and Ferid, M. (2017) *Results in Physics*, **7**, 1022-1029. https://doi.org/10.1016/j.rinp.2017.02.028

[29] Mahapatra, T., Halder, S., Bhuyan, S. and Choudhary, R.N.P. (2018) *Journal of Electronic Materials*, **11**, 6663-6670. https://doi.org/10.1007/s11664-018-6583-0

A Non-Relativistic Explanation of the Sagnac Effect

Olivier Serret

ESIM Engineer, Cugnaux, France

Email: o.serret@free.fr

Abstract

More than a century ago, M. Sagnac realized an experiment with light rays, whose results according to him invalidated the theory of Relativity and validated the hypothesis of the Aether. This hypothesis of the ether was not retained by the scientific community, and relativistic explanations were given to the results of the Sagnac experiment. But these relativistic explanations remain open to criticism because they are various and because the prediction may differ depending on whether the observer's frame of reference is at rest or in motion. The neo-Newtonian mechanics proposes a new explanation which leads to demonstrate the formula $\delta L = -\dfrac{P \cdot R \cdot \Omega}{c}$ with P the light path. In order to verify this new interpretation, it is proposed to do again the Sagnac experiment with a slightly different light path, a square-shaped path. The results should be at least 30% lower than those predicted by the theory of Relativity. In which case, the relativistic explanation would be questioned.

Keywords

Sagnac Effect, Relativity Theory, Aether, Ether, Neo-Newtonian Mechanics, Light Path, Gyrolaser

1. Introduction

In 1913 Georges Sagnac performed an experiment (bearing his name) [1]. This experiment consists of highlighting the shift of the central fringe as a function of the speed of rotation of the disc. Today its main application is the gyrolaser, used in aeronautics, launchers and space. For G. Sagnac, his experience proved the existence of aether. Nevertheless, this hypothesis of the aether has been supplanted for a century by the theory of Relativity, but the given relativistic explanations are arduous and disputed by some. The purpose of this article is to show

the paradoxes of the relativistic explanations and then to propose another explanation, that one based on the neo-Newtonian mechanics (which is nothing but the Newtonian mechanics without the principle of equivalence). This article does not deal with optical fiber gyros which fall under a slightly different principle (the optical fiber moves with the disk).

2. Georges Sagnac's Experiment and Measurement

2.1. Georges Sagnac's Experiment

The rotating interferometer comprises the light source and the receiver, a photographic plate that records the interference fringes located at the focus of a telescope. When the light is sent, from a transmitter placed on the rotating disk, in two opposite directions, the center of interference (which corresponds to the median-band at maximum intensity) shifts as a function of the speed of the disk rotation. This measurement is carried out thanks to the photographic receiver installed on the rotating disc. A description of Sagnac experiment is given in **Appendix A**.

2.2. Measurement

- The interferential displacement "z" (from one direction to the opposite direction) is measured to be worth:

$$z = \frac{16\pi NS}{\lambda c} \left[\mathrm{m/m} \right] \tag{1}$$

with values of **Table 1**.

  Numerical application: $z = 0.07$. It is the offset of the fringe into two opposite directions.

- Unlike what is generally practiced today, G. Sagnac defines the displacement of the central fringe between a rotation direction and the opposite direction. By reducing the formula with the fringe shift *FS* (from one direction compared to the state at rest) which is half of the interferential displacement, we get the following formula (**see APPENDIX A**)

$$FS = 4\frac{S\Omega}{\lambda c} \left[\mathrm{m/m} \right] \tag{2}$$

with Ω, speed of rotation, equal to 22π rad/s.

Table 1. Sagnac values.

Symbol	Designation	Value	Unit
N	Number of revolutions per second	2	rps
S	Surface swept by the light beam	0.0866	m²
λ	Wave length	436	nm
c	Light celerity	3×10^8	m/s

Numerical application: $FS = 0.033$. This is the shift of the central fringe with respect to the center. For example, if the projected interferance $\Lambda = 0.5 \, mm$, the Fringe Shift of the center line is 17 μm.

Note: In his article, at the end of paragraph 2 on the optical vortex effect 1, for $N = 2$, G. Sagnac gives as value of the interfrange a value Λ "*of* 0.5 *mm to* 1 *mm*", that is to say from simple to double! What is the precision of Sagnac measurement? Does it mean something else?

- To overcome this uncertainty on interfranges, in this paper we will use the "path difference" δL [m] defined as

$$\delta L = \lambda \cdot FS \tag{3}$$

In Sagnac experiment, $\delta L = 15 \, nm$.

3. Usual Measurement Interpretations

3.1. According to Newtonian Mechanics

Newtonian mechanics is not able to correctly describe this experiment. In which case, the two light beams would meet at the center of the photographic receiver, there would be no movement of the central fringe. Newtonian mechanics cannot explain the Fringe Shift.

3.2. According to Aether Hypothesis

Hyppolyte Fizeau wanted to prove the existence of the aether with the experience of moving water. In the same way, Georges Sagnac wanted to prove the existence of the aether with his experience. The results are consistent with this hypothesis [2] [3] [4]. The trouble is aether is unable to simply explain the negative result of the Michelson and Morley experiment. Anyway, the aether hypothesis has been supplanted by the theory of Relativity which can give explanation to many astrophysical observations.

3.3. According to Relativity Theory

According to the theory of Relativity, the speed of light in the vacuum is a constant whatever the speed of the reference frame is. For Georges Sagnac, first goal of his experience was to invalidate the theory of relativity that could not explain these results with a constant light celerity in both frames. Indeed with the Sagnac experiment, depending on whether one places the observator in the terrestrial reference frame or in the frame of the rotating disk, the meeting of the two opposite light rays would not occur in the same place (see Figure 1). This inconsistency alone should have invalidated the theory of Relativity.

Yet the partisans of Relativity consider that the Sagnac experiment would be on the contrary a new proof of the theory of Relativity. Paul Langevin was the first to provide an explanation involving a "temporal" shift derivating the formula

$$\delta L(\text{Relativity}) = -4 \frac{S \cdot \Omega}{c} \tag{4}$$

Figure 1. Comparison between different hypotheses.

Since then, other relativistic explanations and derivations have been provided (**see APPENDIX B**). To give various interpretations for the same phenomenon appears unclear and even suspicious.

3.4. A Strange Coincidence

- In the experiment carried out by G. Sagnac, the ratio between the surface S and the perimeter P of this particular polygon is equal to:

$$4S \approx P \cdot R \tag{5a}$$

with R radius of the disc.

- In gyroscopic apparatus used in aerospace [5] [6] with an equilateral triangle, the ratio between the surface S and the perimeter P of the triangle is also equal to: (see **Figure 2**)

$$4S = P \cdot R \tag{5b}$$

Nota: in the triangular gyrolaser manufactured by companies, the light beam passes through a resonator (cavity containing an active medium) and that the signal is amplified electronically, filtered, converted into frequency and calibrated. If an indirect link is maintained between the rotational speed and the modification of the signal, the direct link between the speed of rotation and the displacement in meters of the central fringe is masked.
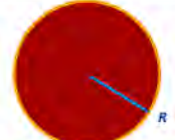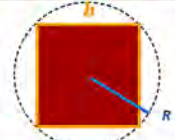
Figure 2. Comparison between Surface and Area.

4. Neo-Newtonian Interpretation

4.1. Neo Newtonian Mechanics

Neo-Newtonian mechanics is similar to Newtonian mechanics except for very high speed:

- The speed of light "c" is practically equal to the asymptotic limit "s". So, $c + v \approx c$.

- The addition or the subtraction of the velocities is done according to the conservation of the momentum. So "$c - v = c - (x * v)$" with $x < 1$. In the case of the light beam, x is close to zero.

- For a synthetic approach to neo-Newtonian mechanics see the Presentation paper [7], and for a detailed approach the **Related Articles** hereafter.

4.2. Neo Newtonian Explication

- It is strange that the Fringe Shift depends on the surface of the figure rather than the path traveled by the light. Thus, neo-Newtonian mechanics proposes, and demonstrates (**see Appendix C**) that the Fringe Shift depends on the path traveled.

    The proposed formula is:

$$\delta L(\text{Neo Newtonian}) = -\frac{P \cdot R \cdot \Omega}{c} \tag{6}$$

- Note that the relativistic derivations are made from the surface of a disk. It is interesting to note that in the case of a circular path, the two approaches give clearly different results (**see Appendix C**):

$$\delta L(\text{Disc / Neo Newtonian}) = \frac{\delta L(\text{Disc / Relativity})}{2} \qquad (7)$$

This could be a way to discriminate both approaches. Unfortunately, it is not possible to make the light rays travel in a perfectly circular path with mirrors. Let us remember that this article does not deal with the drop-down optical fiber gyrometers where the fiber is rotated with the disk.

5. Proposal of Experiment

- Only experiment can help to decide between two interpretations.

It is not possible to simply carry out a real "circular" circulation of the light beams in the vacuum with an infinite number of mirrors. It is here proposed to experiment in a square trajectory (see Figure 3) without resonator nor laser exciter.

- At present time it is difficult to say whether the proponents of Relativity will apply a corrective factor to the square circulation or not. That is why two formulas have been given in the relativistic framework (one by taking up again the formula of the disc, the other by adding a corrective factor proportional to the geometric surface of the square).
- According to Neo-Newtonian, prediction will be done with the single Equation (6).
- Results are in Table 2:

In either case with the square, there is a difference of ($\sqrt{2}/2$ =) 30% to ($\sqrt{2}/\pi$ =) 55% to differentiate the predictions of these two theories. This difference from 30% to 55% is significant and so it would make possible to discriminate between neo-Newtonian and Relativistic predictions.

6. Conclusions

If the Sagnac effect is recognized and today used industrially in gyrolasers for aeronautics and space, its theoretical interpretation remains controversial. For

Table 2. Comparison table between Relativity and Neo-Newtonian predictions.

	Relativity	Neo-Newtonian
General Formula	$\delta L = -4\dfrac{S \cdot \Omega}{c}$	$\delta L = -\dfrac{P \cdot R \cdot \Omega}{c}$
Square	$A(\text{disc}) = \pi R^2$ $S(\text{corrected}) = 2R^2$	$P = 4\sqrt{2}R$
Formula for square	$\delta L = -4\dfrac{\pi R^2 \cdot \Omega}{c}$ $\delta L(\text{corrected}) = -4\dfrac{2R^2 \cdot \Omega}{c}$	$\delta L = -4\dfrac{\sqrt{2} \cdot R^2 \cdot \Omega}{c}$
Example $R = 0.25$ m $\Omega = 2 \times 2\pi$ rd/s	$\delta L = 33$ nm $\delta L(\text{corrected}) = 21$ nm	$\delta L = 15$ nm
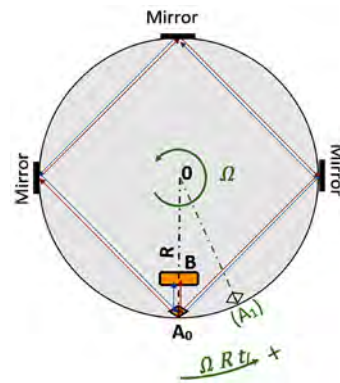
Figure 3. proposed experiment.

the majority of scientists, this would demonstrate the validity of the theory of Relativity, but for some others it invalidates the theory of Relativity and opens the door to other theories such as that of the aether. This was the opinion of Georges Sagnac, the instigator of this experience that bears his name. In this essay, after recalling how neither Newtonian mechanics nor relativistic theory can explain correctly the Sagnac effect, we propose an alternative explanation based on Neo-Newtonian Mechanics (NNM). The Fringe Shift or the difference of light path would not be proportional to the surface swept S but to the light path traveled P. Then we get the formula:

$$\delta L(\text{Neo-Newtonian}) = -\frac{P \cdot R \cdot \Omega}{c}.$$

Neo-Newtonian Mechanics predicts, except in special cases such as the Sagnac's polygon or the equilateral triangle, a different shift from that predicted by the theory of Relativity. For a perfect square path and without resonator nor exciter, it should show a 30% to 55% decrease in the offset. This proposal of experiment, quite similar at first sight to what has already been achieved but nevertheless different, remains to be carried out by a laboratory to discrimeninate both theories.

Conflicts of Interest

The author declares no conflicts of interest regarding the publication of this paper.

References

[1] Sagnac, G. (1914) *J. Phys. Theor. Appl.*, 4, 177-195.
     https://hal.archives-ouvertes.fr/jpa-00241884/document

[2] Su, C.-C. (2000) A Local-Ether Model of Wave Propagation Complying with the Sagnac Correction in the Global Positioning System. *IEEE Antennas and Propagation Society International Symposium. Transmitting Waves of Progress to the Next Millennium.* 2000 *Digest. Held in Conjunction with*: *USNC/URSI National Radio Science Meeting* (*C*), Salt Lake City, UT, 16-21 July 2000, 1570-1573.
     https://ieeexplore.ieee.org/abstract/document/874526

[3] Silvertooth, E.W. (1989) Motion through the Ether. EWW.

http://www.naturalphilosophy.org/pdf/abstracts/abstracts_1248.pdf

[4] Marett, D. (2010) The Premise for Comparing Ether Theories to Relativity Theory. http://www.conspiracyoflight.com/Premise_Ether/Premise_Ether.html

[5] Daussy, C. (2015) Le Gyrolaser. SAGEM. http://paristech.institutoptique.fr/site.php?id=1010&fileid=14007

[6] Bretenaker, F. (2007) Le Gyrolaser. CNRS. http://sfp.in2p3.fr/expo/Conf2010/Lasers/Bretenaker.pdf

[7] Serret, O. (2018) *General Science Journal*, 4. http://www.gsjournal.net/Science-Journals/Research%20Papers-Relativity%20Theory/Download/7499

[8] Rizzi G. and Ruggiero, M.L. (2004) Relativity in Rotating Frames: Relativistic Physics in Rotating Reference Frames. Springer Science, Berlin. https://www.springer.com/la/book/9781402018053

[9] Pascoli, G. (2017) *Comptes Rendus Physique*, **18**, 563-569. https://doi.org/10.1016/j.crhy.2017.10.010

[10] Bouyer, P. (2013) *Gyroscopy and Navigation*, **5**, 20-26. https://link.springer.com/article/10.1134%2FS2075108714010039

[11] Arnoux, C. (1994) Gyrolasers-L'effet Sagnac. http://www.cax.free.fr/sagnac/sagnac.html

[12] Malykin, G. (2000) *Physics-Uspekhi*, **43**. https://iopscience.iop.org/article/10.1070/PU2000v043n12ABEH000830/pdf

[13] Spagnou, P. (2013) Sagnac et l'expérience à contresens. Bibnum. https://journals.openedition.org/bibnum/737#tocto1n4

RELATED ARTICLES about Neo-Newtonian Mechanics (NNM)

	CRITICISMS OF THE THEORY OF THE RELATIVITY
[a] **GPS vs. Relativity**	GPS, Relativity and pop-Science Mythology http://alternativephysics.org/book/GPSmythology.htm
[b] **Lorentz derivation**	Mathematical Inconsistencies in Einstein's Derivation of the Lorentz Transformation" https://www.physicsmyths.org.uk/lorentz.htm *Reply to "A Simple Derivation of the Lorentz Transformation"* http://file.scirp.org/pdf/JMP_2017121915203275.pdf

	THEORY AND EXPERIMENTS
[c] **Lorentz factor**	*How to Demonstrate the Lorentz Factor: Variable Time vs. Variable Inertial Mass* http://file.scirp.org/pdf/JMP_2015022510573131.pdf
[d] **Velocity Addition**	*Velocity Addition Demonstrated from the Conservation of Linear Momenta, an Alternative Expression* http://file.scirp.org/pdf/JMP_2015050609513342.pdf *An improvement of the accuracy of Fizeau's experiment* http://gsjournal.net/Science-Journals/Research%20Papers-Relativity%20Theory/Download/7247
[e] **Force in the Synchrotron**	*Net Force $F = \gamma^3 ma$ at High Velocity* http://file.scirp.org/pdf/JMP_2016042814580505.pdf
[f] **Muons Lifetime**	*Muon Lifetime would depend of its Energy* http://www.mrelativity.net/Papers/51/Muons%20Serret%20Millennium.pdf
[g] **Sagnac effect**	*Present article*

	COSMIC OBSERVATIONS
[h] **Mercury perihelion**	*About the ovoid orbits in general, and perihelion precession of Mercury in particular* (2) http://www.mrelativity.net/Papers/51/Mercury%20Millennium%20Serret%205%20janvier%202018.pdf
[i] **Gravitational light deflection**	*Hipparcos did not measure directly the light bending!* http://gsjournal.net/Science-Journals/Research%20Papers-Mechanics%20/%20Electrodynamics/Download/6998 *Gravitational Light Deflection: could Relativity be Invalidated by GAIA?* http://mrelativity.net/Papers/51/Light%20deflection%20SERRET%20Millennium%20Aout%202018.pdf
[j] **Shapiro time delay**	*Shapiro Time Delay derivates from Refraction* http://www.mrelativity.net/Papers/51/Shapiro%20SERRET%20Millennium%20juillet%202018.pdf
[k] **Dispersion Measurement of Pulsars**	*The Mass of a Photon estimated from the Pulsar Dispersion Measurement* (*DM*) http://gsjournal.net/Science-Journals/Research%20Papers-Relativity%20Theory/Download/7490
[l] **Pioneer Anomaly**	*The Pioneer Anomaly explained by the Processing of the Doppler Effect* http://gsjournal.net/Science-Journals/Research%20Papers-Relativity%20Theory/Download/7330
[m] **Dark Matter**	*The flat rotation curve of our galaxy explained within Newtonian mechanics* https://physicsessays.org/browse-journal-2/product/1240-7-olivier-serret-the-flat-rotation-curve-of-our-galaxy-explained-within-newtonian-mechanics.html
[n] **Dark Energy**	*Gravity vs. Dark Energy, about the Expansion of the Universe* http://file.scirp.org/pdf/JMP_2018011714405269.pdf
[o] **Gravitational waves**	*Gravitational waves or particle radiation?* https://www.physicsessays.org/browse-journal-2/product/1588-12-olivier-serret-gravitational-waves-or-particle-radiation.html

APPENDIX A: G. SAGNAC'S EXPERIMENT
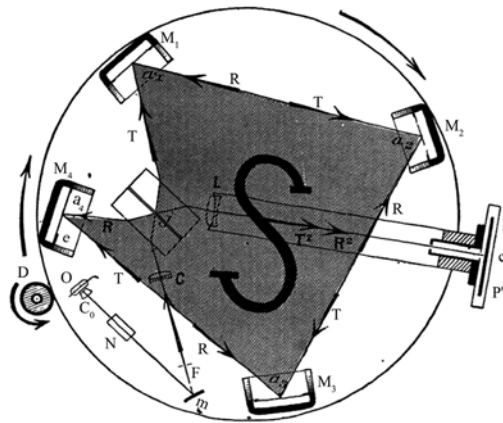
Figure 4. G. Sagnac's experimental setup.

Between two photos of the receiver, one taken with a direction of rotation and the other one in the other direction, Sagnac uses in his experiment (see **Figure 4**) the parameter z defined as the displacement (relative) of the center of interference:

$$z = \frac{\Delta c}{\Lambda} \, [\text{m/m}] \tag{A1}$$

with

Δc = distance between the central fringe c1 in one direction of rotation and the central fringe c2 in the other direction of rotation.

Λ = interfrange = interval between two dark lateral fringes f (cf middle of paragraph 6 of G. Sagnac's article).

He then obtains as a formula of z:

Equation (1) $\quad z = \frac{16\pi NS}{\lambda c} \, [\text{m/m}]$ $\qquad$ **(A2)**

with

S surface swept by the light beam.

N number of revolutions per second [rps].

Considering the speed of rotation Ω:

$$\Omega = 2\pi N \, [\text{rad/s}] \tag{A3}$$

we are getting

$$z = 8\frac{S\Omega}{\lambda c} \, [\text{m/m}] \tag{A4}$$

Note 1:

z is similar to Fringe Shift, except that we usually take the distance between the central fringe c1 according to a direction of rotation and the central fringe c0 of the immobile disk, *i.e.* $\Delta c/2$.

Thus

$$FS = \frac{\Delta c/2}{\Lambda} \tag{A5}$$

$$FS = \frac{z}{2} \tag{A6}$$

$$\text{Equation (2)} \quad FS = 4\frac{S\Omega}{\lambda c}\,[\mathrm{m/m}] \tag{A7}$$

Note 2:

This formula appears coherent, although dissimilar on the sufaces, with that found in the scientific literature [6]:

$$FS = 4\frac{A\Omega}{\lambda c}\,[\mathrm{m/m}] \tag{A8}$$

with A the Area of the disc.

APPENDIX B: Relativistic Explanations

Relativity theoriy could explain Sagnac from different ways:

a) By the relativity of the simultaneity [8]:

A simultaneous event in one frame is not in another frame. Two light rays can meet simultaneously in a frame (in motion) and not in another frame (motionless): it is the "temporal" shift (*).

This was put into equation first by Paul Langevin in 1921 [9] [10] [11]:

$$\begin{cases} t_+ = \dfrac{2\pi R + \Omega R t_+}{c} = \dfrac{\Omega R t_+}{v} \\ t_- = \dfrac{2\pi R - \Omega R t_-}{c} = \dfrac{\Omega R t_-}{v} \end{cases} \tag{B1}$$

b) By time dilatation:

Sagnac effect can be attributed to the difference in the time dilation (or phase change) [12].

c) Length variation

With the rotating disc, the lengths depend on the direction of travel [13].

*: Discussion about the "temporal" shift:

The difficulty of the "temporal" shift explanation is that it is not compatible with the interference of the Young slits(**): the central line corresponds to the same optical path, it moves according to the variation of optical path (and not according to a variation of time, to the relativity of simultaneity or to a "temporal" shift). For the central peak, whatever its movement (at the same light celerity):

$$t_+ = t_- = t_i \tag{B2}$$

and so

$$\begin{cases} ct_i = 2\pi R \\ \Omega R t_i = 0 \end{cases} \tag{B3}$$

$$\begin{cases} t_i = \dfrac{2\pi R}{c}\,! \\ t_i = 0\,!! \end{cases} \tag{B4}$$

: Principle of the interference peak of Young slits: see **Figure 5.

Peak of interference intensity where the 2 paths (at the same light celerity) are equal, where the difference in path is zero.

$$FS = \frac{\delta L}{\lambda} = \frac{a}{\lambda D} x \, [\text{m/m}] \tag{B5}$$

APPENDIX C: Neo-Newtonian Derivation

To detail the neo-Newtonian explanation, we will proceed in two steps:

- First we will simplify the experience of G. Sagnac to half a turn.
- Then we will return to the initial case with a complete turn.

First step: simplification of the experimental scheme

The simplification relates to two points:

1) We replace the polygonal surface S by a circular surface.
2) And we change the location of the "opposite" photographic receiver on the disc of the light source (**see Figure 6**). The distance traveled by the beams being then half less, the offset is then in this assembly half less.

Hypotheses: in (Ro) frame,

- From the geometry of the circle:

$$A_0 I^+ + I^- A_0 = P \tag{C1}$$

with P for Perimeter, or light path.

- Disc in rotation:

$$V = \Omega R \tag{C2}$$

$$A_0 A_1 = \Omega R t_I \tag{C3}$$

So $B_0 B_1 = \Omega R t_I \tag{C4}$
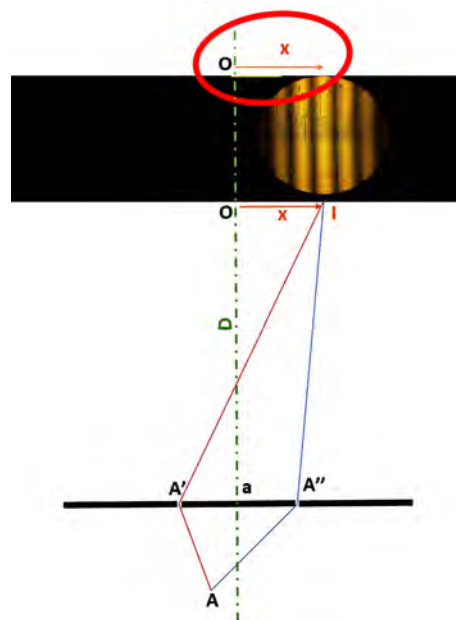
Figure 5. Young interference.
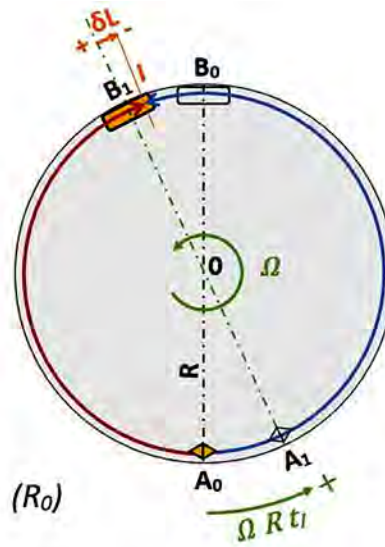
A: the emitter of the (synchronous) light beams
B: the centre of the photographic receiver receiving the light rays
I: the central fringe, the meeting point of the two synchronous light rays
δL: is the difference of light path, the shift of the central line I with respect to the centre B of the photographic receiver [m]
t_I : the travel time of the light rays from A_0 to I
A_0 : the emitter of the (synchronous) light beams at time t=0
B_0 : the centre of the photographic receiver, receiving the rays at time t=0
A_1 : the emitter of the (synchronous) light beams at time t=t_I
B_1 : the centre of the photographic receiver, receiving the rays at time t=t_I

Figure 6. Simplification of the experimental setup.

- Trajectory of the two light rays:

$$A_0 I^+ = c^+ t_I \tag{C5}$$

and

$$A_0 I^- = -c^- t_I \tag{C6}$$

as defined

$$\delta L = B_1 I \tag{C7}$$

- In Neo-Newtonian Mechanics:

$$c^+ = c + \varepsilon \quad \text{with} \quad \varepsilon \cong 0 \tag{C8}$$

$$c^- = c - x \cdot V \quad \text{with} \quad 0 < x < 1 \tag{C9}$$

Consequence:
From (C7)

$$\delta L \left(\frac{1}{2} \right) = B_1 B_0 + B_0 I \tag{C10}$$

$$\delta L \left(\frac{1}{2} \right) = B_0 I - B_0 B_1 \tag{C11}$$

By geometry

$$A_0 I = A_0 B_0 + B_0 I \tag{C12}$$

$$\text{So} \quad B_0 I = A_0 I - A_0 B_0 \tag{C13}$$

$$\text{So} \quad B_0 I = A_0 I - P/2 \tag{C14}$$

From (C11), (C14)

$$\delta L = A_0 I - P/2 - B_0 B_1 \tag{C15}$$

From (C4), (C5)

$$\delta L\left(\frac{1}{2}\right) = c^+ t_I - \pi R - \Omega R t_I \tag{C16}$$

From (C1), (C5), (C6)

$$c^+ t_I + c^- t_I = P \tag{C17}$$

$$t_I = \frac{P}{c^+ + c^-} \tag{C18}$$

From (C8), (C9)

$$t_I \cong \frac{P}{2c - x \cdot V} \tag{C19}$$

From (C8), (C16), (C19)

$$\delta L\left(\frac{1}{2}\right) = (c - \Omega R)\frac{P}{2c - x \cdot V} - P/2 \tag{C20}$$

$$\delta L\left(\frac{1}{2}\right) = \frac{Pc - P\Omega R - cP + Px \cdot V/2}{2c - x \cdot V} \tag{C21}$$

$$\delta L\left(\frac{1}{2}\right) = \frac{-P\Omega R + Px \cdot V/2}{2c - x \cdot V} \tag{C22}$$

$$V \ll c \quad \delta L\left(\frac{1}{2}\right) = \frac{-PR\Omega + Px \cdot V/2}{2c} \tag{C23}$$

From (C2)

$$\delta L\left(\frac{1}{2}\right) = \frac{-PR\Omega + Px \cdot R\Omega/2}{2c} \tag{C24}$$

$$\delta L\left(\frac{1}{2}\right) = -\frac{PR\Omega}{2c}\left(1 - \frac{x}{2}\right) \tag{C25}$$

Comment: with $x < 1$ then $\delta L < 0$.

The sign "minus" means that the peak of interference occurs in the vicinity to the right of B1 (cf Figure)

$$\text{With} \quad x \ll 1 \; \delta L\left(\frac{1}{2}\right) \approx -\frac{PR\Omega}{2c} \tag{C26}$$

IV.2 Second step: full rotation

Second step: Now let's go back to the un-simplified case with a full rotation.

In that case you have to double the path and therefore the Equation (C28) to:

$$\textbf{Equation 6} \quad \delta L\left(\text{Neo-Newtonian}\right) = -\frac{PR\Omega}{c} \tag{C27}$$

- Remark 1: in the case of a circle

$$PR = 2\pi R^2 = 2A \tag{C28}$$

$$\delta L\left(\text{Circle / Neo-Newtonian}\right) = -2\frac{A\Omega}{c} \tag{C29}$$

➢ It is <u>half</u> what the theory of Relativity predicts for a circle!
- <u>Remark 2:</u> in the case of a square

$$P = 4\sqrt{2}R \tag{C30}$$

$$\delta L\left(\text{Square / Neo-Newtonian}\right) = -4\frac{\sqrt{2}R^2\Omega}{c} \tag{C29}$$

Drawing Kerr

Rainer Burghardt

A-2061 Obritz 246, Obritz, Austria

Email: arg@aon.at

Abstract

The Kerr metric is analyzed using strictly geometrical elements. A 4-dimensional surface representing the geometry of the Kerr model is embedded into a 5-dimensional flat space. The field strengths of the model are explicitly worked out and understanding of the theory is supported by numerous figures. The structure of the field equations is analyzed.

Keywords

Kerr Geometry, Geometrical Interpretation, Kerr Surface

1. Introduction

The metric of a rotating stellar object was found by Kerr [1] in 1963, albeit in a form that was hard to process. Two years later the metric was rewritten with the help of elliptical-hyperbolical coordinates by Boyer and Lindquist [2]. Enderlein [3] has given a good representation of the elliptical-hyperbolical coordinate system and Krasinski [4] has looked more deeply at the problem. We have analyzed the Kerr model in a series of papers, with a clear presentation in [5] and [6]. Nevertheless, we believe that the Kerr model is still too little understood. Thus, we have decided to present a very detailed presentation, supplemented by numerous drawings.

2. Basics of the Kerr Metric

The Kerr metric in the form of Boyer-Lindquist

$$\mathrm{d}s^2 = \frac{\rho^2}{\Delta}\mathrm{d}r^2 + \rho^2\mathrm{d}\vartheta^2 + \frac{\sin^2\vartheta}{\rho^2}\Big[\big(r^2+a^2\big)\mathrm{d}\varphi - a\,\mathrm{d}t\Big]^2 - \frac{\Delta}{\rho^2}\Big[\mathrm{d}t - a\sin^2\vartheta\,\mathrm{d}\varphi\Big]^2 \quad (2.1)$$

$$\Delta = r^2 - 2Mr + a^2, \quad \rho^2 = r^2 + a^2\cos^2\vartheta$$

is nowadays the standard form of the Kerr metric used in the literature. r, ϑ, and φ are quasi-polar coordinates and t the coordinate time. However, we ar-

gue that the elements in this metric do not disclose the geometric structure of the model. Therefore we have put the metric into the form

$$ds^2 = dx^{1^2} + dx^{2^2} + \left[\alpha_R dx^3 + i\alpha_R \omega \sigma dx^4\right]^2 + a_S^2\left[-i\alpha_R \omega \sigma dx^3 + \alpha_R dx^4\right]^2$$

$$dx^1 = \alpha_S a_R dr, \quad dx^2 = \Lambda d\vartheta, \quad dx^3 = \sigma d\varphi, \quad dx^4 = idt = \rho_S di\psi \qquad (2.2)$$

With the definitions

$$\alpha_S = \frac{A}{\delta}, \quad a_S = \frac{\delta}{A}, \quad A^2 = r^2 + a^2, \quad \delta^2 = r^2 + a^2 - 2Mr,$$

$$\Lambda^2 = r^2 + a^2 \cos^2 \vartheta, \quad \sigma = A \sin \vartheta, \quad \omega = a/A^2, \qquad (2.3)$$

$$a_R^2 = 1 - \omega^2 \sigma^2 = \frac{\Lambda^2}{A^2}, \quad \alpha_R = 1/a_R, \quad \rho_S = a_R A \sqrt{\frac{2r}{M} \frac{r^2 + a^2}{r^2 - a^2}}$$

we will realize that a geometric meaning can be assigned to the quantities of the metric (2.2). We will discuss this in the following.

First, we want to make clear that the line element

$$ds^2 = \frac{\Lambda^2}{A^2} dr^2 + \Lambda^2 d\vartheta^2 + A^2 \sin^2 \vartheta d\varphi^2 \qquad (2.4)$$

can be interpreted as a line element on an oblate ellipsoid of revolution represented in quasipolar coordinates $x^\alpha = \{r, \vartheta, \varphi\}$ in a 3-dimensional flat space. The connection to Cartesian coordinates $x^{\alpha'}, \alpha' = 1', 2', 3'$ is given by

$$x^{3'} = A \sin \vartheta \cos \varphi$$

$$x^{2'} = A \sin \vartheta \sin \varphi \qquad (2.5)$$

$$x^{1'} = r \cos \vartheta$$

The quasipolar coordinate net is given by confocal ellipsoids, hyperbolae as their orthogonal trajectories, and circles as horizontal slices of the ellipsoids of revolution. The coordinate surfaces are given by the equation of the ellipsoids and hyperbolae

$$\frac{\left(x^{2'}\right)^2 + \left(x^{3'}\right)^2}{A^2} + \frac{\left(x^{1'}\right)^2}{r^2} = 1, \quad \frac{\left(x^{2'}\right)^2 + \left(x^{3'}\right)^2}{a^2 \sin^2 \vartheta} - \frac{\left(x^{1'}\right)^2}{a^2 \cos^2 \vartheta} = 1$$

Enderlein [3] has depicted this coordinate net as shown in **Figure 1**.
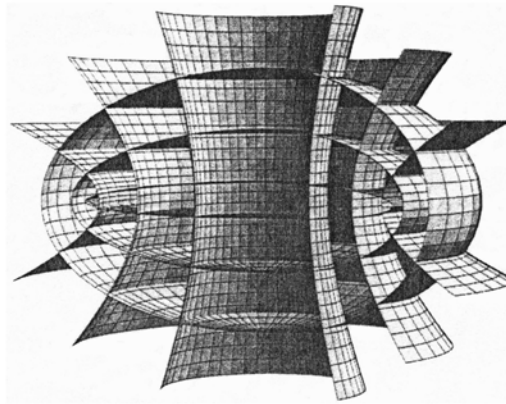
Figure 1. Elliptic-hyperbolic coordinate system by Enderlein.

A slice of the ellipsoid of revolution should make understandable the position of the coordinate lines and is shown in **Figure 2**.
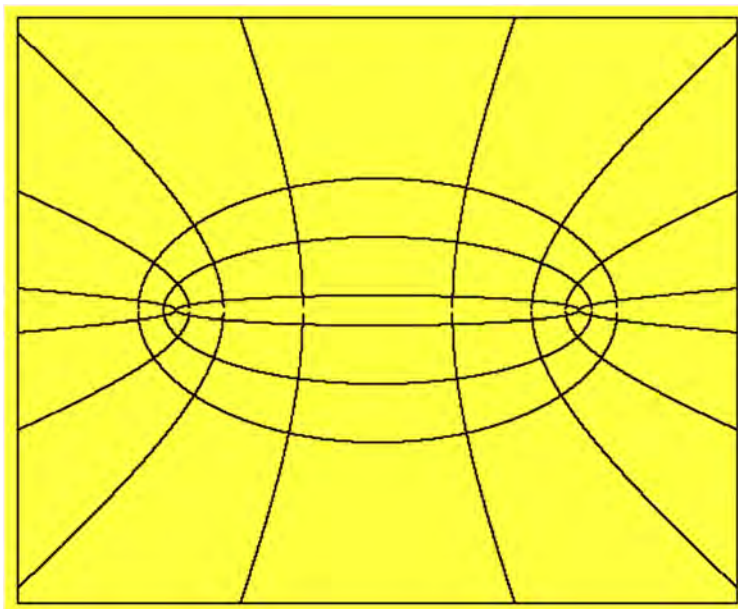
Figure 2. The elliptic-parabolic coordinate system.

In order to work out the meaning of the quantities in (2.2), we first deal in detail with the ellipses by reducing the problem to two dimensions

$$
\begin{aligned}
x^{1'} &= r \cos \vartheta \\
x^{2'} &= A \sin \vartheta
\end{aligned}
\tag{2.7}
$$

Evidently r and A are the minor and major axes of the confocal ellipses. Although the coordinate r is not the radial direction of the system, the historical notation is maintained. The meaning of the quasi-polar angle ϑ can be found in **Figure 3**.
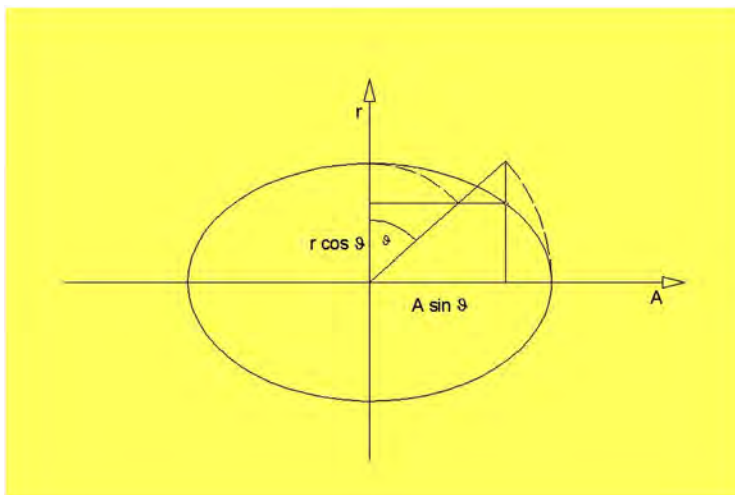
Figure 3. Basic elements of an ellipse.

Further properties of the ellipses can be made accessible. If one draws the focal rays s_1 and s_2 from the foci of an ellipse to any point of the ellipse, one finds, with **Figure 4**, the relations

$$s_1^2 = x^{1'2} + \left(x^{2'} + a\right)^2, \quad s_2^2 = x^{1'2} + \left(x^{2'} - a\right)^2$$
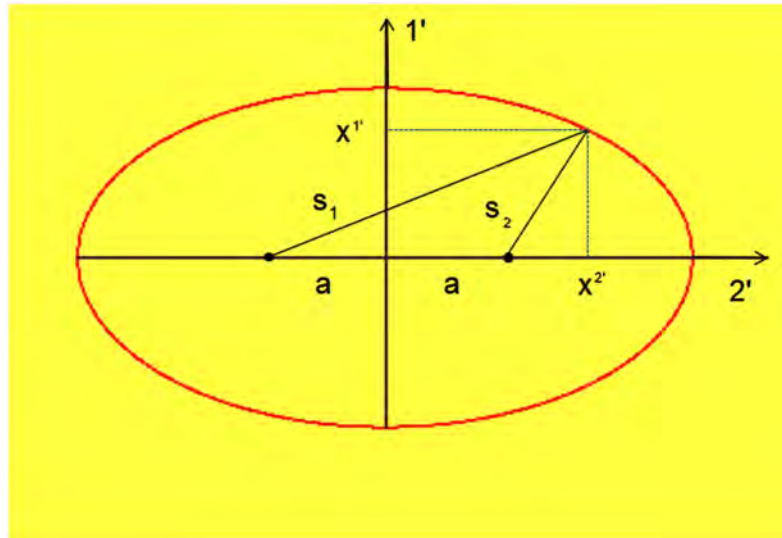
Figure 4. Focal rays and eccentricity.

and then

$$s_1 = A + a\sin\vartheta, \quad s_2 = A - a\sin\vartheta$$
$$s_1 s_2 = A^2 - a^2\sin^2\vartheta = r^2 + a^2\cos^2\vartheta$$

Thus, the fundamental quantities of the ellipses can be represented as the geometric and the arithmetic means of the focal rays

$$\Lambda = \sqrt{s_1 s_2}, \quad A = \frac{s_1 + s_2}{2} \tag{2.8}$$

The factor ahead of $\mathrm{d}r^2$ in (2.4) has to be examined in more detail. At $\vartheta = 0$, *i.e.* at the minor axes of the ellipses, this factor $\left(r^2 + a^2\cos^2\vartheta\right)/\left(r^2 + a^2\right)$ is equal to 1, so that the radial part of the metric is reduced to $\mathrm{d}r^2$. At $\vartheta = \pi/2$ the factor is r^2/A^2. It follows that the radial arc element has the value $\mathrm{d}A$ at this position. Thus, the quantity Λ/A describes the varying distance of two neighboring confocal ellipses; at the minor axis this distance is $\mathrm{d}r$ and at the major axis it is $\mathrm{d}A$. This proves that several quantities of the geometry show this behavior, so that it is sufficient to compute these quantities at one of the minor axes, and then to multiply them by this factor, which we call *elliptical factor*. However, these quantities offer a further surprise. With

$$a_R^2 = \frac{\Lambda^2}{A^2} = 1 - \frac{a^2}{A^2}\sin^2\vartheta = 1 - \omega^2\sigma^2, \quad \omega = \frac{a}{A^2} \tag{2.9}$$

one recognizes that within these relations are buried the angular velocity ω, and the orbital speed $\omega\sigma$ of a potentially rotating model. The BL system al-

ready makes available the fundamental quantities for a rotating system. Not surprisingly, the Kerr geometry is built on an elliptical system.

From the equations of the ellipses and hyperbolae one gets the nonvanishing components of the curvature vectors

$$\rho_\alpha^E = \{\rho_E, 0, 0\}, \quad \rho_\alpha^H = \{0, \rho_H, 0\}, \quad \rho_E = \frac{\Lambda^3}{rA}, \quad \rho_H = -\frac{\Lambda^3}{a^2 \sin\vartheta \cos\vartheta} \quad (2.10)$$

$\alpha = 1, 2, 3$ is a tetrad index. The two vectors are perpendicular and are in each case tangent to the other family of curves. In this way the term radial is defined in this geometry. "Radial" refers to the directions which are specified by the tangents of the hyperbolae.

Facing the 3$^{\text{rd}}$ dimension, $\sigma = A \sin\vartheta$ is the curvature radius of the circles, the parallels of the ellipsoid of revolution. Finally, one has the *curvatures* of the coordinate lines

$$B_\alpha = \left\{\frac{1}{\rho_E}, 0, 0\right\}, \quad N_\alpha = \left\{0, \frac{1}{\rho_H}, 0\right\}, \quad C_\alpha = \left\{0, 0, \frac{1}{\sigma}\right\} \quad (2.11)$$

These quantities and their derivatives constitute the curvature equations of the system and satisfy the "field equations" $R_{\alpha\beta} = 0$, where $R_{\alpha\beta}$ is the 3-dimensional Ricci for the parabolic-hyperbolic system.

3. The Kerr Surface

So far, we have associated geometrical meaning to the quantities of the flat metric (2.4), written in elliptic-hyperbolic coordinates. Now we return to the metric (2.2), but we omit the timelike part. To explain the factor $\alpha_S = A/\delta$ in the radial arc element, we extend (2.5) with the extra dimension $x^{0'}$

$$
\begin{aligned}
x^{0'} &= -\int \tan\varepsilon \, dr \\
x^{1'} &= r \cos\vartheta \\
x^{2'} &= A \sin\vartheta \cos\varphi \\
x^{3'} &= A \sin\vartheta \sin\varphi
\end{aligned}
\quad (3.1)
$$

We will show that (3.1) provides an embedding of a surface into a 5-dimensional flat space, which we will discuss in more detail.

We define the angle ε by

$$\sin\varepsilon = -\frac{r}{A}\sqrt{\frac{2M}{r}}, \quad \cos\varepsilon = \frac{\delta}{A}, \quad \tan\varepsilon = -\frac{\sqrt{2Mr}}{\delta}, \quad (3.2)$$

where ε has the orientation cw. Evidently $\tan\varepsilon$ tends to infinity for $\delta = 0$. The solution to r of this equation is

$$r_H = M + \sqrt{M^2 - a^2} \quad (3.3)$$

r_H settling the event horizon of the Kerr model. Finally, the integral in (3.1) reads as

$$x^{0'} = \int_{r_H}^{r} \sqrt{\frac{2Mr}{r^2 + a^2 - 2Mr}} \, dr \quad (3.4)$$

The solution does not have a closed form; however, the integral can be evaluated numerically. If one suppresses the φ-dimension the surface appears as shown in **Figure 5**.
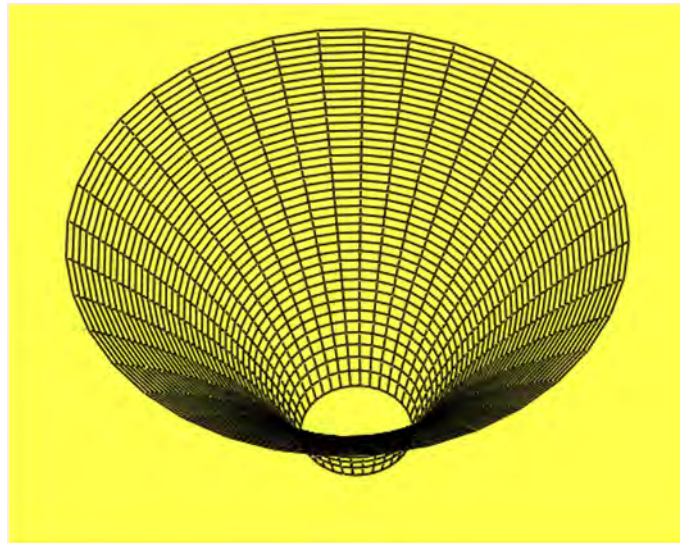
Figure 5. The surface with suppressed φ-dimension.

The surface looks like a "funnel". Its horizontals are ellipses. The ellipse fixed by r_H is the ellipse at the waist of the funnel and is the "end" of the geometry. $\delta = 0$ marks the limit of the model. The projection of the funnel onto the base planes shows ellipses crossed by hyperbolae. Thus, the integral lines (3.4) have a 1st and 2nd curvature. We note that the ansatz (3.1) still does not provide the Kerr metric. We have to add further ingredients to gain the metric (2.2). But **Figure 5** shows a lot of the properties that the genuine Kerr surface will have.

This surface is closely related to the Schwarzschild surface, *i.e.* Flamm's paraboloid. For $a = 0$ the metric (2.2) is reduced to the Schwarzschild metric and the elliptical coordinate system breaks down to the spherical polar system. The integral lines are parabolae and their projections onto the base plane are straight lines.

If one extends to the φ-dimension and suppresses the ϑ-dimension, the surface builds up on concentric circles and is even more closely related to Flamm's paraboloid.

We must bear in mind that dr is the increase of the minor axes of the ellipses on the base plane. In contrast,

$$\mathrm{d}x^1 = a_R \mathrm{d}r \tag{3.5}$$

is the distance of two neighboring ellipses and depends on the angle ϑ. If one pulls up elliptical cylinders on two of such ellipses, one can see that their cutting curves with the surface do not lie on the horizontal slices of the surface. During a circulation on the surface the points of the cutting curve oscillate. From

$$\mathrm{d}x_{hol}^{0'} = -\tan\varepsilon\,\mathrm{d}r = -\tan\varepsilon\,\alpha_R\left(r,\vartheta\right)\mathrm{d}x^1 = -\tan\chi\,\mathrm{d}x^1 \tag{3.6}$$

one gets the augment of the height of the surface into the extra dimension.

It is evident that the tangent related to the auxiliary angle χ which points to the next higher point of the surface depends on the angle ϑ. A short calculation would show that one does not arrive at the desired seed metric by using (3.6) either. For our model only the horizontal elliptical slices of the surface are of importance. If one follows the normal vector of the surface along an ellipse, one will discover that this vector also oscillates on its way, because the walls of the surface are round about differently scarped. In order to be able to use the surface, it has to be equipped with an additional structure. On the minor axes of the ellipses the elliptical factor is $a_R = 1$ and the geometry is Schwarzschild-like. That is where we start: we define a *rigging vector* in such a way that it coincides with the normal vector at this position, and that it always encloses the same angle with the base plane during its circulation. Then this rigging vector is no longer vertical to the surface and its vertical planes are no longer tangent to the surface. The family of all of these planes—and if one adds the φ-dimension, the family of the 3-dimensional hyperplanes—represents our graphic space, if we assume that we live in such a world. Those hyperplanes are anholonomic, as will be shown.

Now we replace the holonomic differential (3.6) by an anholonomic one

$$\mathrm{d}x_{anh}^{0'} = -\tan \varepsilon \, a_R(r,\vartheta)\mathrm{d}r = -\tan \varepsilon \mathrm{d}x^1 \qquad (3.7)$$

that is no longer integrable. We call the family of hyperplanes that are orthogonal to these differentials and that are no longer V_3-forming *physical surface*. It is the area of all possible physical observations.

However, the structure of the $[r, \varphi]$-part of the surface is simple. On this patch no elliptical properties and hence no anholonomies arise. It corresponds to Flamm's paraboloid of the Schwarzschild geometry. Sharp [7] has searched for such a surface for $\vartheta = \pi/2$. However, he did not start from the seed metric, but incorporated rotational parts of the Kerr metric into his computations. Hence, his result differs substantially from ours. From

$$\mathrm{d}s^2 = \mathrm{d}x^{0'^2} + \mathrm{d}x^{1'^2} + \mathrm{d}x^{2'^2} + \mathrm{d}x^{3'^2}$$

one indeed obtains with

$$\mathrm{d}s^2 = \left(\tan^2 \varepsilon + 1\right)\frac{\Lambda^2}{A^2}\mathrm{d}r^2 + \Lambda^2 \mathrm{d}\vartheta^2 + A^2 \sin^2 \vartheta \mathrm{d}\varphi^2$$

the desired seed metric, which serves as a basis for the actual Kerr metric. From the definition $a_S = \delta/A$ in (2.3) and the introduction of $\cos \varepsilon = \delta/A$, and with the definition of the elliptical factor a_R we obtain the spatial part of the Kerr metric

$$\mathrm{d}s^2 = \alpha_S a_R \mathrm{d}r^2 + \Lambda^2 \mathrm{d}\vartheta^2 + A^2 \sin^2 \vartheta \mathrm{d}\varphi^2 \qquad (3.8)$$

and the surface related to this metric we will call *Kerr surface*.

The anholonomic construction will be examined in more detail. Figure 6 shows the constellation of the holonomic and anholonomic vectors, namely the

two "radial" vectors, the vector[1] dx^1_{hol} in the tangent planes of the surface and the associated vector dx^1_{anh} in the anholonomic hyperplanes, which have the same projections onto the basic plane.
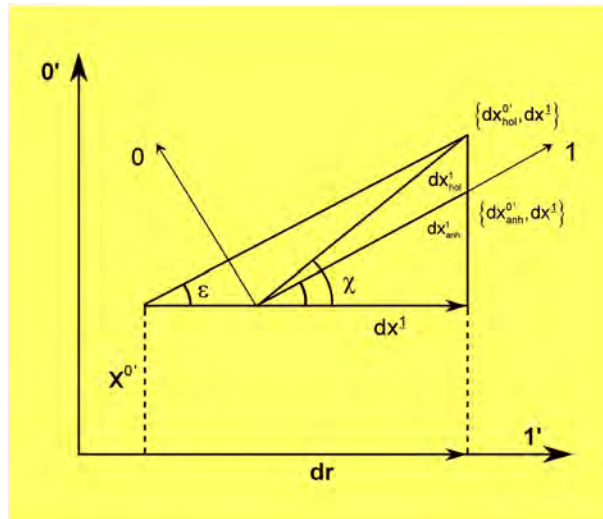
Figure 6. Holonomic and anholonomic differentials.

Having explained the structure of the Kerr metric, we return to Equation (3.2) and recognize that the ascent of the integral curve is $-\tan\varepsilon = \infty$ for $\delta = 0$, *i.e.* at $\varepsilon = \pi/2$. Thus, the integral lines are normal to the base plane at r_H. For $\varepsilon = 0$ the ascent is $\tan\varepsilon = 0$ and the geometry will be flat in the infinite.

We also read from (3.2) that for vanishing eccentricity a of the ellipses, *i.e.* $a = 0$, we get with $A = r$

$$\sin\varepsilon = -\sqrt{\frac{2M}{r}}, \quad \cos\varepsilon = \sqrt{1 - \frac{2M}{r}}, \quad \frac{1}{\cos\varepsilon} = \frac{1}{\sqrt{1 - \frac{2M}{r}}}$$

Thus, in this case $\sin\varepsilon$ is the velocity of a freely falling observer in the Schwarzschild model and $1/\cos\varepsilon$ the related Lorentz factor.

We have good reasons to interpret

$$v_S = \sin\varepsilon = -\frac{r}{A}\sqrt{\frac{2M}{r}}, \quad \alpha_S = \frac{1}{\sqrt{1 - v_S^2}} = \frac{A}{\delta} \tag{3.9}$$

as velocity of a freely falling observer in the exterior field of a rotating stellar object and α_S as the correlated Lorentz factor of this motion. r/A is the ratio of the axes of the ellipses. This means that the velocity of a freely falling observer depends on position in relation to the ellipses.

At the waist of the Kerr surface $(\delta = 0)$ is $v_R = -1$, *i.e.* the observer has (asymptotically) reached the velocity of light, measured with his proper time independently of his former position on the ellipse. Since we do not assume that

---

[1] All the other components of the vector except the mentioned one vanish in the local reference system.

velocities higher than the velocity of light can occur, we have to realize that the waist of the Kerr surface is not only a geometrical limit, but also a physical limit of the model. No object can cross the event horizon r_H.

In addition, we have to bear in mind that a radial motion in the fields of rotating objects in free fall is not possible. Since frame dragging acts on observers, the motion of an observer will get a circular component. Due to Einstein's law of composition of velocities the velocity of an observer will asymptotically reach the velocity of light before reaching the event horizon. The limit in this case is the ergosphere, as we have shown in [5] [6]. Our point of view is supported by similar circumstances in the Schwarzschild model. In contrast to the claims of Misner, Thorne, and Wheeler [8], we have shown in several papers and in [5] [6] that an observer starting from an arbitrary position can reach the Schwarzschild radius only asymptotically in infinite proper time. We have also shown [9] that the surface of a collapsing star, described by the Schwarzschild interior solution, collapses eternally, reaching the inner horizon of the model asymptotically in infinite proper time. Thus the final state of a collapsing non-rotating stellar object is an ECO (Eternally Collapsing Object) [10].

Thus, if we believe that this geometrical description of a rotating star is a good description of Nature, we have to dismiss the possibility of the formation of rotating black holes. We have supplemented the Kerr solution with an interior solution [11] [12], which has the property of developing into the interior Schwarzschild solution for $a = 0$. However, we have made no attempt to implement a collapse for this model and we have not found any effort in the literature in this regard. If such an approach is possible, a RECO (Rotating Eternally Collapsing Object) would be expected.

4. Curvatures of the Elliptic-Hyperbolic Geometry

So far we have shown that the Kerr model is based on an elliptic-hyperbolic system, endowed with an integral surface with elliptical horizontals, which could be envisaged as an elliptically deformed Flamm's paraboloid. The Boyer-Lindquist coordinate system, with its curved coordinate lines, contributes to Einstein's field equations, which have little to do with the physical content of the model but are incorporated in the connexion coefficients of the physical quantities and must be treated for this reason.

Still suppressing the timelike part of the seed metric, we have to deal with the curvature vectors

$$\rho_a^S = \{\rho_S, 0, 0, 0\}, \quad \rho_a^E = \{0, \rho_E, 0, 0\},$$
$$\rho_a^H = \{0, 0, \rho_H, 0\}, \quad \rho_a^C = \{0, 0, 0, \rho_C\}, a = 0, 1, 2, 3 \tag{4.1}$$

ρ_E and ρ_H are the components of the curvature vectors of the ellipses and hyperbolae. They have been mentioned in (2.10). $\rho_C = \sigma = A \sin \vartheta$ is the radius of the circles of the parallels of the ellipsoids of revolution. ρ_S is the curvature radius of the integral lines and was calculated in [5] [6][2].

---

[2]The interested reader should have at hand one of these monographs.

The inverse quantities of (4.1) are the curvatures in vector form. Their tetrad components related to BL-coordinates are

$$M_a = \{1,0,0,0\} \frac{1}{\rho_S}, \quad B_a = \{\sin\varepsilon, \cos\varepsilon, 0, 0\} \frac{1}{\rho_E}, \quad N_a = \{0,0,1,0\} \frac{1}{\rho_H},$$

$$C_a = \{\sin\varepsilon\sin\theta, \cos\varepsilon\sin\theta, \cos\theta, 0\} \frac{1}{\rho_C}, \tag{4.2}$$

where

$$\sin\theta = \frac{r}{\Lambda}\sin\vartheta, \quad \cos\theta = \frac{A}{\Lambda}\cos\vartheta. \tag{4.3}$$

All the quantities in (4.2) obey the structure

$$\frac{\mathrm{d}}{\mathrm{d}r}\frac{1}{r} + \frac{1}{r^2} = 0. $$

The "field equations" for B, N and C refer to the elliptic-hyperbolic system and drop out from Einstein's field equations. But we cannot omit these quantities, because we need them for the covariant derivative of the physical quantities which we will discuss later on.

We start with the detailed discussion of these quantities. The quantity B is related to the curvature radii ρ_E of the ellipses. We know that the curvature B is normal to the ellipses. Thus, we introduce an auxiliary reference system $a'' = 0'', 1'', 2''$ and suppress the φ-dimension for the sake of simplifying the problem. In this system B has only one component

$$B_{a''} = \{0,1,0\} \frac{1}{\rho_E}, \tag{4.4}$$

as seen in **Figure 7**. For the sake of simplicity, the holonomic Kerr surface is used for some of the quantities for the drawings.
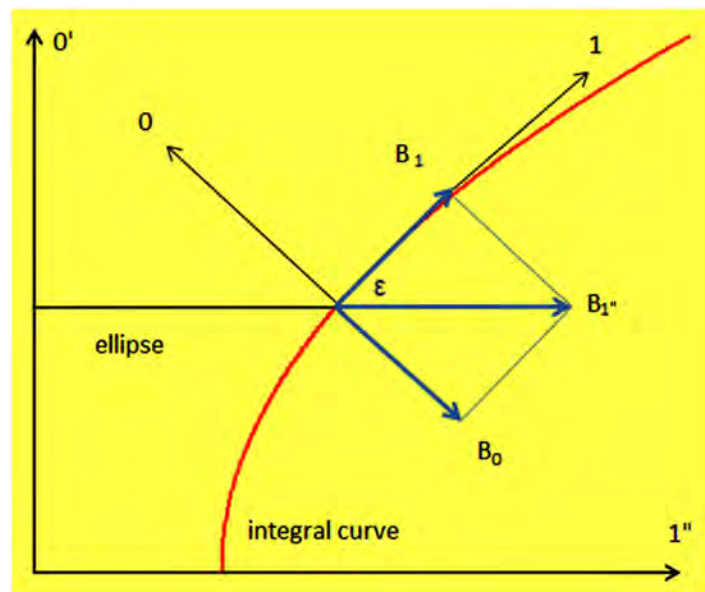
Figure 7. Vertical splitting of $B_{1''}$

It is evident that $B_{1''}$ can be split into two components with respect to the BL system. One component (B_1) is tangent to the integral curve and the other one (B_0) is normal to the curve, pointing in the 0-direction, *i.e.* the local extradimension. Thus, one has

$$B_a = \{\sin\varepsilon, \cos\varepsilon, 0\}\frac{1}{\rho_E}. \qquad (4.5)$$

$B_1 = \frac{1}{\rho_E}\cos\varepsilon$ is the very component an observer can measure in his physical space, B_0 is hidden to him.

Furthermore, we ask for the components of B in the Cartesian coordinate system of the embedding space. We obtain

$$B_{a'} = \{0, \cos\theta, \sin\theta\}\frac{1}{\rho_E}. \qquad (4.6)$$

The components of $B_{a'}$ are depicted in **Figure 8**:
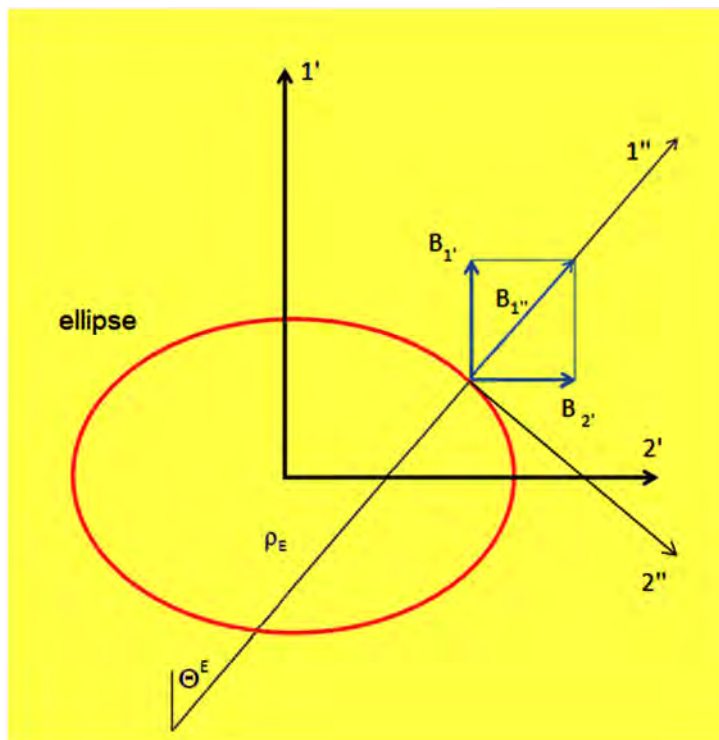
Figure 8. Horizontal splitting of $B_{1''}$.

From the figure it can be seen that θ_E is the angle of ascent of the curvature radius of the ellipse and can be calculated by (4.3), setting $\theta_E = \theta$. With $\{\rho_E, \theta_E\}$ one can describe the elliptical system instead of $\{r, \vartheta\}$. Alternatively, one can describe the hyperbolic system with $\{\rho_H, \theta_H\}$, where $\theta_H = \pi/2 - \theta_E$, bearing in mind that the ellipses and hyperbolae are orthogonal trajectories.

Now we turn to the quantity N, which is related to the curvature radii ρ_H of the hyperbolae. We find the hyperbolae in the horizontals of the Kerr surface.

Again, the auxiliary reference system is chosen in such a way that the 1"-direction is tangent to the hyperbolae and the 2"-direction is tangent to the ellipses. Thus, the curvature N has only one component in this system

$$N_{a''} = \{0,0,1\}\frac{1}{\rho_H} \tag{4.7}$$

as can be seen in **Figure 9**.
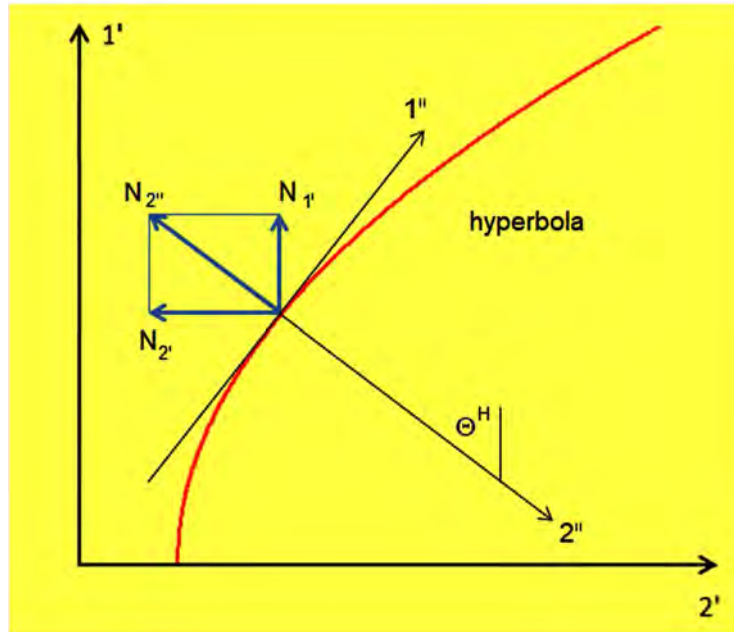
Figure 9. Horizontal splitting of N.

In the Cartesian reference system N has the components

$$N_{a'} = \{0,-\sin\theta,\cos\theta\}\frac{1}{\rho_H} = \{0,\cos\theta_H,-\sin\theta_H\}\left(-\frac{1}{\rho_H}\right), \tag{4.8}$$

recalling that ρ_H is a negative quantity and that $\theta_H = \pi/2 - \theta$. In the BL system one has

$$N_a = \{0,0,1\}\frac{1}{\rho_H}. \tag{4.9}$$

Next, we discuss the quantity C, which is related to the curvature radii of the circular parallels of the ellipsoids of revolution, *i.e.* $\rho_C = \sigma = A\sin\vartheta$. Thus, C has only one component in the Cartesian system lying in the 2'-direction

$$C_{a'} = \{0,0,1\}\frac{1}{\sigma}. \tag{4.10}$$

But two components occur in the auxiliary system a''

$$C_{a''} = \{0,\sin\theta,\cos\theta\}\frac{1}{\sigma} \tag{4.11}$$

as seen from **Figure 10**.
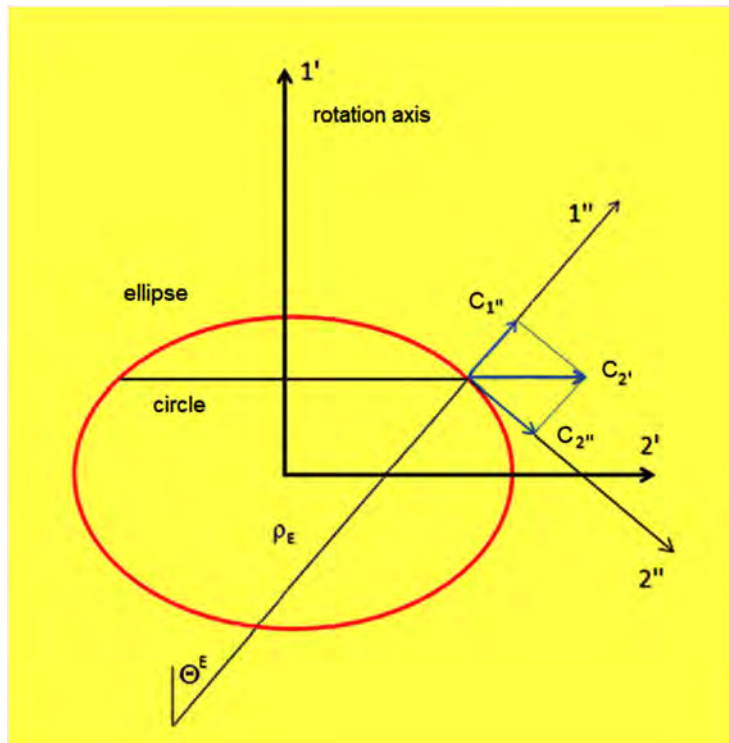
Figure 10. Horizontal splitting of *C*.

Finally, the component $C_{1''}$ has a projection onto the tangent of the integral curve and onto the local extradimension

$$C_a = \left\{\sin \varepsilon \sin \theta, \cos \varepsilon \sin \theta, \cos \theta\right\} \frac{1}{\sigma}.$$ (4.12)

This is depicted in **Figure 11**.
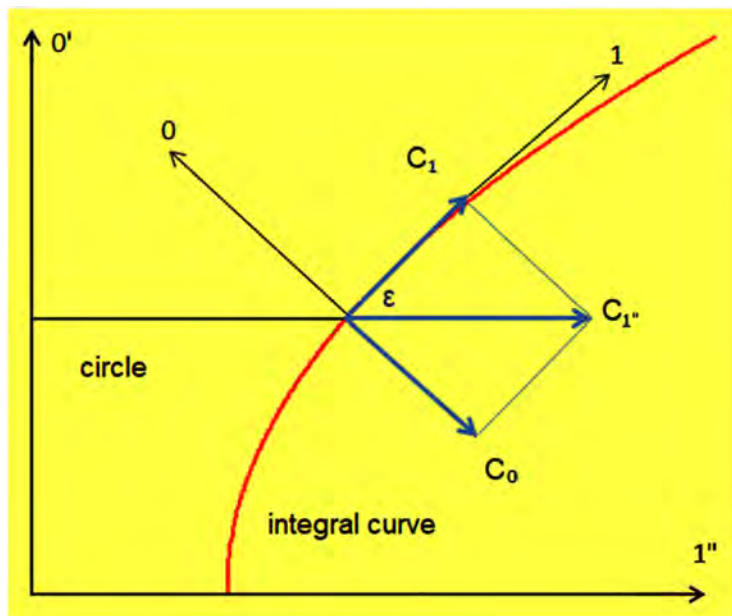
Figure 11. Vertical splitting of *C*.

Recall that the angle ε is cw and thus C_0 is pointing into the opposite direction of the local extradimension x^0.

The quantity M still needs to be discussed. It does not belong to the elliptic-hyperbolic system, but to the integral surface. M is related to the curvature radii of the integral lines and has the components

$$M_a = \{1,0,0\}\frac{1}{\rho_S}, \quad M_{a'} = \{\cos\varepsilon, \sin\varepsilon\cos\theta, \sin\varepsilon\sin\theta\}\frac{1}{\rho_S},$$

$$M_{a''} = \{\cos\varepsilon, \sin\varepsilon, 0\}\frac{1}{\rho_S} \tag{4.13}$$
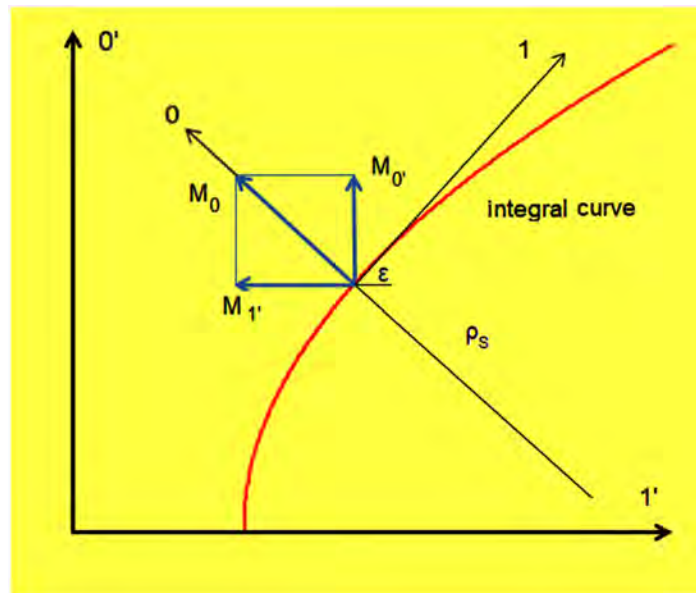
Figure 12. Vertical splitting of M.

M is situated in the direction of the local extradimension as shown in Figure 12. The quantity is only important for the use of 5-dimensional covariant derivatives. Since we do not use this formalism in this paper, we will not discuss this quantity in detail.

So far we have intuitively derived various representations of the fundamental quantities by drawing figures. For the interested reader we note the transformation matrices

$$\Lambda^a_{a''} = \begin{pmatrix} \cos\varepsilon & \sin\varepsilon & \\ -\sin\varepsilon & \cos\varepsilon & \\ & & 1 \end{pmatrix}, \quad \Lambda^{a''}_{a'} = \begin{pmatrix} 1 & & \\ & \cos\theta & \sin\theta \\ & -\sin\theta & \cos\theta \end{pmatrix}$$

$$\Lambda^a_{a'} = \begin{pmatrix} \cos\varepsilon & \sin\varepsilon\cos\theta & \sin\varepsilon\sin\theta \\ -\sin\varepsilon & \cos\varepsilon\cos\theta & \cos\varepsilon\sin\theta \\ & -\sin\theta & \cos\theta \end{pmatrix} \tag{4.14}$$

With the help of these one can calculate all the expressions of this section.

Now we are prepared to discuss the full seed metric for the Kerr model. One has

$$ds^2 = \alpha_S^2 a_R^2 dr^2 + \Lambda^2 d\vartheta^2 + A^2 \sin^2 \vartheta d\varphi^2 + a_S^2 \rho_S^2 di\psi^2 . \tag{4.15}$$

Therein dx^4 is evidently defined by

$$dx^4 = idt = \rho_S di\psi . \tag{4.16}$$

The metric is written in the original Hilbert notation with index 4, *i.e.* (++++) and the timelike element is interpreted as an arc on a pseudo circle, shown as a pseudoreal representation in **Figure 13**.
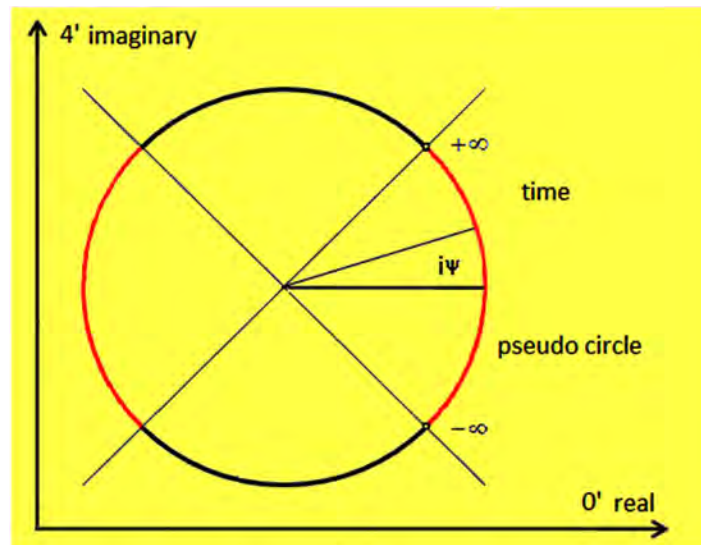
Figure 13. The geometrical definition of time.

We have to bear in mind that when using a real and an imaginary axis the pseudo circle cannot be drawn or even imagined. The time we measure with our clocks is the real accessory number of an imaginary angle and the flow of time is the arc of a pseudo circle. The infinite past and the infinite future are the points on the 45˚ axes in the figure.

Sometimes another pseudoreal representation is used, a hyperbola instead of a circle. This has the advantage that the infinite can be better visualized, but the hyperbola shows a position-dependent curvature, while the pseudo circle has a constant curvature, including the infinite. Therefore a pseudo circle is also called *hyperbola of constant curvature*. Unfortunately the pseudoreal representation with hyperbolae misleads some authors to take the hyperbolae literally, but this hinders a geometric explanation of the Kerr metric with the help of an embedding.

We call the factor a_S in (4.15) *gravitational factor*. Its derivative leads us to the force of gravity $E_1 = \dfrac{1}{\rho_S} \tan \varepsilon$ and is a member of the Ricci-rotation coefficients of the seed model. From (2.3) we see that if the rotational parameter is $a = 0$ the elliptical factor is $a_R = 1$, and also $A = r$. Thus, taking ρ_S from (2.3) we obtain $\rho_S = \sqrt{\dfrac{2r^3}{M}}$, the curvature radius of Flamm's paraboloid of the Schwarz-

schild geometry. In this case, $E_1 = \dfrac{1}{\rho_S}\tan\varepsilon$ will be the gravitational force of the Schwarzschild model. Since the angle ε is cw, the gravitational force is pointing inwards.

Now we analyze the geometrical meaning of this quantity. In the 5-dimensional embedding space it has the components

$$E_a = \left\{-\frac{1}{\rho_S}, \frac{1}{\rho_S}\tan\varepsilon, 0\right\} = \left\{\cos\varepsilon, -\sin\varepsilon, 0\right\}\left(-\frac{1}{\rho_S\cos\varepsilon}\right),$$

$$E_{a'} = \left\{1,0,0\right\}\left(-\frac{1}{\rho_S\cos\varepsilon}\right) \tag{4.17}$$

From **Figure 14**
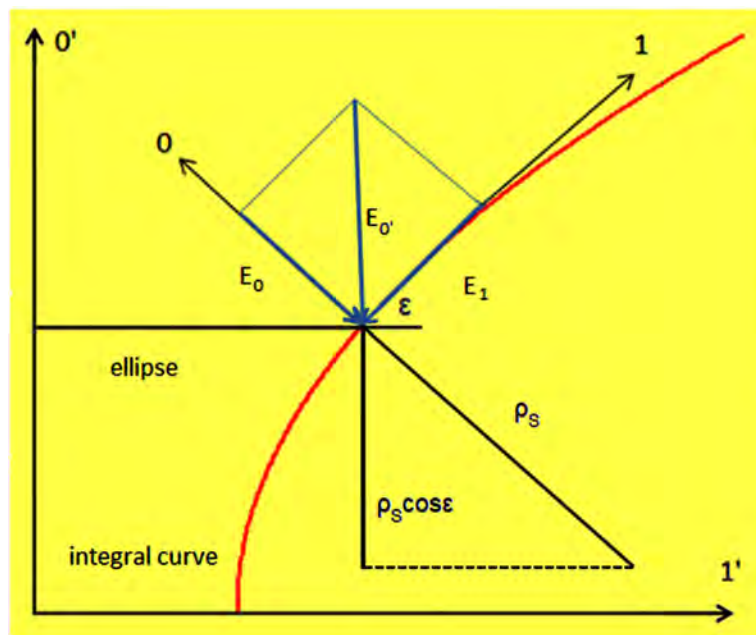
Figure 14. The gravitational force.

we can see that $\rho_S\cos\varepsilon$ are the projections of the curvature radii ρ_S into the extradimension $0'$ of the embedding space. $E_{0'}$ is the inverse of $\rho_S\cos\varepsilon$. It is split into the components with respect to the local BL reference system a. E_1 is tangent to the integral curves. It is the very quantity a physical observer can experience. The second component is hidden to him.

Having explained the fundamental quantities of the seed metric with curvatures, we reformulate the metric with the help of curvature radii. For the flat elliptic-hyperbolic system we have

$$\mathrm{d}s^2 = \rho_H^2 \mathrm{d}\theta_H^2 + \rho_E^2 \mathrm{d}\theta_E^2 + \rho_C^2 \mathrm{d}\varphi^2$$

and for the seed metric with $\rho_\psi = \rho_S\cos\varepsilon$ we have

$$\mathrm{d}s^2 = \rho_S^2 \mathrm{d}\varepsilon^2 + \rho_E^2 \mathrm{d}\theta_E^2 + \rho_C^2 \mathrm{d}\varphi^2 + \rho_\psi^2 \mathrm{d}i\psi^2.$$

5. The Field Equations

All the quantities B, N, C, E discussed in the previous section are members of the Ricci-rotation coefficients and satisfy the subequations of Einstein's field equations. For a detailed discussion we again refer to [5] [6]. Here we restrict ourselves to noting some relations. For the elliptic-hyperbolic basic system we obtain

$$B_{1|1} + B_1 B_1 = \Omega^2, \quad N_{2|2} + N_2 N_2 = -\Omega^2 .$$

The occurrence of the quantity Ω is the second surprise of the elliptic-hyperbolic system. It is a second-rank tensor describing rotational effects which we will meet with the genuine Kerr metric. Evidently the sum of the above equations vanishes. In a covariant form the curvature equations of the elliptic-hyperbolic system can be written as

$$\left[N^s_{\underset{2}{\|s}} + N^s N_s \right] + \left[B^s_{\underset{2}{\|s}} + B^s B_s \right] = 0, \quad \left[C^s_{\underset{3}{\|s}} + C^s C_s \right] = 0, \quad s = 1, 2, 3, 4. \qquad (5.1)$$

Thus, these subequations of the Ricci drop out from Einstein's field equations. The only quantity of physical interest is the force of gravity. It is contained in Einstein's field equations with the structure

$$E^s_{\underset{4}{\|s}} - E^s E_s , \qquad (5.2)$$

i.e. the field of gravity is coupled to itself, due to the non-linearity of Einstein's field equations.

To get the Equations (5.1) and (5.2) we have skipped the tedious procedure of *dimensional reduction*, *i.e.* getting rid of all 0-components and all 0-derivatives of the fundamental quantities, and we have restricted ourselves to the flat basic system, the shadow on the horizontals of the Kerr surface. Thus, we are left with 4-dimensional quantities and their *graded derivatives* [5] [6]. We will only briefly remark on how the quantity Ω comes into the theory. We have extensively used coordinate systems with ellipses and their curvature vectors, which represent a kind of polar system. But we have to bear in mind that the pole of this system is not fixed, but moves on the evolute of the ellipses, if the curvature vector moves on the ellipses. Thus, the change of ρ_E and of the related curvature B has two contributions, the one by motion of the tip of the curvature vector on the evolvente, the other one by motion of the tail of the curvature vector on the evolute. The latter produces the term Ω^2. The same holds for ρ_H and the related curvature N.

The seed metric does not provide a vacuum solution, it is an auxiliary metric, a forerunner to better explain the Kerr metric. Thus, we will not continue with this model but will turn to study the rotational effects in the next section.

6. Rotation

Starting with the seed metric (4.15), we define an anholonomic transformation

$$\Lambda_3^{3'} = \alpha_R, \quad \Lambda_4^{3'} = i\alpha_R\omega, \quad \Lambda_3^{4'} = -i\alpha_R\omega\sigma^2, \quad \Lambda_4^{4'} = \alpha_R$$

$$\Lambda_{3'}^3 = \alpha_R, \quad \Lambda_{4'}^3 = -i\alpha_R\omega, \quad \Lambda_{3'}^4 = i\alpha_R\omega\sigma^2, \quad \Lambda_{4'}^4 = \alpha_R. \tag{6.1}$$

$$\omega = \frac{a}{A^2}, \quad \omega\sigma = \frac{a}{A}\sin\vartheta$$

Operating on the coordinate indices of the tetrads, we get the genuine Kerr metric

$$ds^2 = dx^{1^2} + dx^{2^2} + \left[\alpha_R dx^3 + i\alpha_R\omega\sigma dx^4\right]^2 + a_S^2\left[-i\alpha_R\omega\sigma dx^3 + \alpha_R dx^4\right]^2 \tag{6.2}$$

$$dx^4 = \rho_S di\psi = idt$$

ω is the angular velocity and $\omega\sigma$ the orbital velocity of an observer subjected to frame dragging by the field of a rotating source. The 4-bein system obtained in this way is named system C after Carter and is one of the preferred reference systems attributed to the Kerr model. The coordinate system is oblique-angled, the Carter tetrads are mutually perpendicular by definition.

In contrast, if we perform a Lorentz transformation

$$L_3^{3'} = \alpha_R, \quad L_4^{3'} = i\alpha_R\omega\sigma, \quad L_3^{4'} = -i\alpha_R\omega\sigma, \quad L_4^{4'} = \alpha_R \tag{6.3}$$

operating on the tetrad indices of the seed metric, we obtain instead of

$$ds^2 = \alpha_S^2\alpha_R^2 dr^2 + \Lambda^2 d\vartheta^2 + dx^{3^2} + a_S^2 dx^{4^2}, \quad dx^3 = A\sin\vartheta d\varphi \tag{6.4}$$

the metric

$$ds^2 = \alpha_S^2\alpha_R^2 dr^2 + \Lambda^2 d\vartheta^2 + \left[\alpha_R dx^3 + i\alpha_R\omega\sigma dx^4\right]^2 + \left[-i\alpha_R\omega\sigma dx^3 + \alpha_R a_S dx^4\right]^2 \tag{6.5}$$

which differs from the genuine Kerr metric (6.2) only by the position of the gravitational factor a_S concerning the last brackets. Although the two metrics are very similar, they have a quite different physical interpretation. While in (6.2) the rotation is inherent, the metric (6.5) is still static, but observers are rotating around the source producing the exterior field. We use the similarities of the metrics to make clearer the structure of the rotational effects of the Kerr metric.

It will be shown that the metrics (6.2) and (6.5) exhibit the same fundamental rotational structures. Since it turns out that (6.5) is much easier to treat, we make use of this property, and we will compare the results for both metrics at the end of the section.

Evidently, it is sufficient to consider the [3,4]-piece of the metric. We make a further simplification: we put $a_S = 1/\alpha_S = 1$, i.e. we switch off the gravitational force. Thus, we are left only with rotational effects and we get

$$ds^2 = \alpha_R^2 dr^2 + \Lambda^2 d\vartheta^2 + \left[\alpha_R dx^3 + i\alpha_R\omega\sigma dx^4\right]^2 + \left[-i\alpha_R\omega\sigma dx^3 + \alpha_R a dx^4\right]^2, \tag{6.6}$$

the metric for the elliptic-hyperbolic base system, the shadow of the Kerr system on the parallels, a flat system with rotating observers. The Ricci-rotation coefficients of this metric contain new forces derived from the orbital velocity $\omega\sigma$ and the associated Lorentz factor α_R. From (2.9) we know that the angular velocity ω depends on r. It is decreasing outwards and zero at infinity. Thus, one

has a *differential rotation law*, a property of the model being a condition for a physically functional rotating model.

From the Lorentz factor α_R from the orbital motion we get with

$$\frac{1}{\alpha_R}\alpha_{R|\alpha} = F_\alpha + D_\alpha \tag{6.7}$$

the relations

$$F_\alpha = \alpha_R^2\omega^2\sigma\sigma_\alpha, \quad D_\alpha = \alpha_R^2\omega\omega_{|\alpha}\sigma^2. \tag{6.8}$$

Evidently the first quantity in the above formulae is the relativistic generalization of the centrifugal force; it is normal to the rotation axis. The second emerges from the differential law of rotation $\omega = \omega(r)$. It has only one component and is pointing inwards. From the orbital velocity we derive

$$H_{\alpha\beta} = 2i\alpha_R^2\omega\sigma_{[\alpha}c_{\beta]}, \quad D_{\alpha\beta} = i\alpha_R^2\omega_{|\alpha}\sigma c_\beta, \quad c_\beta = \{0,0,1\}. \tag{6.9}$$

H is antisymmetric and is the relativistic generalization of the Coriolis field strength. The quantity D is a consequence of the differential law of rotation and is asymmetric ($D_{3\beta} = 0$). Both quantities are summarized to

$$\Omega_{\beta\alpha} = -H_{\alpha\beta} - D_{\alpha\beta}. \tag{6.10}$$

By the decomposition of Ω into an antisymmetric and a symmetric part

$$\Omega_{\beta\alpha} = -\left[H_{\alpha\beta} + D_{[\alpha\beta]}\right] - D_{(\alpha\beta)} \tag{6.11}$$

one obtains the total rotational field strength and the deformation field strength. Ω is the very quantity we met at the end of Section 5 when considering the motions of the curvature vectors on the evolutes of the ellipses and hyperbolae. The symmetric part represents the shears

$$u_{(\alpha\|\beta)} = -D_{(\alpha\beta)}, \quad u_m = \{0,0,0,1\} \tag{6.12}$$

that should be understood as the observers sliding past each other on account of the different speeds on neighboring circular paths, whereby shears of the surrounding volume elements arise. The new quantities satisfy the relations

$$u_{m\|n}u^n = F_m, \quad u_{\alpha\|\beta} = \Omega_{\alpha\beta}, \quad \alpha = 1,2,3, \quad m = 1,2,3,4, \tag{6.13}$$

where the double strokes indicate the ordinary covariant derivative in tetrad representation.

From Einstein's field equations $R_{mn} \equiv 0$ one obtains equations of Maxwell type

$$F^m_{\ \|m} - F^mF_m - \Omega^{mn}\Omega_{nm} = 0$$

$$\Omega^{mn}_{\ \|m} + 2\Omega^{[nm]}F_m = 0 \tag{6.14}$$

The centrifugal force is coupled to the field energy, which is composed of quadratic terms. The quantity Ω is coupled to the Poynting vector $2\Omega^{[nm]}F_m$. Further, the relations

$$F_{[m\|n]} + D_{[m\|n]} = 0, \quad F_{[m\|n]} + 2\Omega_{3[m}\Omega_{n]3} = 0$$
$$\Omega_{[mn\|s]} + \Omega_{[mn}F_{s]} = 0 \tag{6.15}$$

are satisfied. They are Maxwell-like as well. The conservation laws

$$\frac{\partial}{\partial t}\left(F^m F_m + \Omega^{mn}\Omega_{nm}\right) = 0, \quad \left(2\Omega^{[nm]}F_m\right)_{\|n} = 0 \tag{6.16}$$

are valid. In the formulae above we used the 4$^{\text{th}}$ graded derivative [5] [6]. It corresponds to the spatial covariant derivative.

If we drop the restriction $a_S = 1$ we obtain the gravitational force E_m entering Einstein's field equations with the structure (5.2). In the above equations E will accompany the centrifugal force F_m, which has the opposite orientation but not the same direction.

Now we compare the simplified equations with the one of the genuine Kerr metric

$$E^s_{\ \|s} + F^s_{\ \|s} - \Omega^{rs}_C\Omega^C_{sr} = 0 \tag{6.17}$$

$$F_{[m\|n]} + D_{[m\|n]} = 0, \quad F_{[m\|n]} = 2\Omega_{3[n}\Omega_{n]3}, \quad E_{[m\|n]} = 0 \tag{6.18}$$

$$\Omega^C_{[mn\|s]} = \Omega^C_{[mn}D_{s]} - \Omega^C_{[mn}E_{s]} = 0 \tag{6.19}$$

$$\left[E^s_C E^C_s + \Omega^{sr}_C\Omega^C_{rs}\right]_{|4} = 0, \quad \left[2\Omega^{[ms]}_C E^C_s\right]_{\|m} = 0, \quad E^C_n = E_n + F_n \tag{6.20}$$

The tag C indicates the quantities of the Carter system, where some of the new quantities differ from the quantities of the simplified system by a factor. In the first brackets one finds terms quadratic in the field strengths. They represent the field energy and are conserved. The second brackets contain the divergence-free Poynting vector. We recognize that the simplified rotational piece of the Kerr model is very close to the genuine Kerr theory.

For a better understanding of the above equations we make a further simplification by putting $\omega = const.$. In this case the quantities D_α and $D_{\alpha\beta}$, referring to the differential rotation law, vanish. Only the centrifugal force F_α and the vorticity $H_{\alpha\beta}$ remain. The field equations for these quantities are Maxwell-like.

First, we define the axial vector

$$H^\alpha = -\frac{i}{2}\varepsilon^{\alpha\beta\gamma}H_{\beta\gamma}, \quad H^{\alpha\beta} = i\varepsilon^{\alpha\beta\gamma}H_\gamma \tag{6.21}$$

and we obtain

$$H^\alpha = \alpha_R^2 \omega\tau^\alpha, \quad \tau^\alpha = \{\cos\theta, \sin\theta, 0\}. \tag{6.22}$$

Having transformed this vector into Cartesian coordinates we have

$$H^{\alpha'} = \alpha_R^2 \omega\tau^{\alpha'}, \quad \tau^{\alpha'} = \{1, 0, 0\}. \tag{6.23}$$

Since $\tau^{\alpha'}$ is a unit vector lying in the 1'-direction, it is parallel to the rotation axis of the ellipsoids as can be seen from Figure 15.
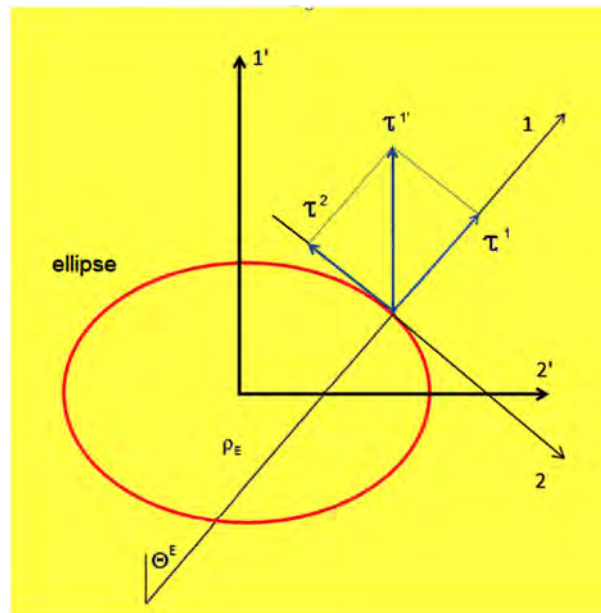
Figure 15. The axial unit vector.

Thus, one can write in vector notation

$$div\,\boldsymbol{F} = \boldsymbol{F}^2 + 2\boldsymbol{H}^2, \quad rot\,\boldsymbol{F} = 0$$
$$div\,\boldsymbol{H} = 0, \qquad rot\,\boldsymbol{H} = \boldsymbol{F} \times 2\boldsymbol{H} \tag{6.24}$$

wherein *div* is the 3-dimensional covariant divergence and *rot* the 3-dimensional covariant rotator. The centrifugal force $\boldsymbol{F}$ has as a source the field energy, the Coriolis force $\boldsymbol{H}$ is coupled to the Poynting vector. The conservation laws take the form

$$\frac{\partial}{\partial t}\left(\boldsymbol{F}^2 + 2\boldsymbol{H}^2\right) = 0, \quad div\left(\boldsymbol{F} \times 2\boldsymbol{H}\right) = 0. \tag{6.25}$$

Evidently, the field equations have a similar structure to the Maxwell equations of electrodynamics. The genuine Kerr Equations (6.14)-(6.20) also have almost the same structure. The similarity of gravitation and electrodynamics was first discovered by Lense and Thirring [13] and Thirring [14] [15] [16] in weak field approximation and treated in general form by Hund [17]. In the last decades this problem was investigated by many authors and called gravito-electromagnetism (GEM).

7. Kerr Interior Solution

Several authors have tried to complement the Kerr solution with an interior model. Although the results have been unsatisfactory to date, the search for a solution is still ongoing. We [11] [12] have proposed an interior solution which goes over into the Schwarzschild solution by setting the rotational parameter *a* to zero. For this model we did not solve Einstein's field equations but instead constructed the model in terms of geometrical methods.

The interior metric

$$ds^2 = dx^{1^2} + dx^{2^2} + \left[\alpha_R dx^3 + i\alpha_R \omega\sigma dx^4 \right]^2 + a_T^2 \left[-i\alpha_R \omega\sigma dx^3 + \alpha_R dx^4 \right]^2$$

$$dx^1 = \alpha_I a_R dr, \quad dx^2 = \Lambda d\vartheta, \quad dx^3 = \sigma d\varphi, \tag{7.1}$$

$$dx^4 = i dt, \quad \alpha_R = \frac{1}{a_R}, \quad a_R^2 = 1 - \omega^2\sigma^2$$

has the same form as the exterior (2.2). It differs by the geometrical factor

$$\alpha_I = \frac{1}{a_I}, \quad a_I^2 = 1 - \frac{r^2}{\mathcal{R}^2} \tag{7.2}$$

and the gravitational factor

$$a_T = \frac{1}{2} \left[\left(1 + 2\Phi_g^2\right)\cos\eta_g - \cos\eta \right] \Phi_g^{-2}$$

$$\Phi_g^2 = \frac{r_g^2 + a^2}{r_g^2 - a^2}, \quad \cos\eta_g = \sqrt{1 - \frac{r_g^2}{\mathcal{R}^2}}, \quad \cos\eta = \sqrt{1 - \frac{r^2}{\mathcal{R}^2}} = a_I \tag{7.3}$$

$\mathcal{R}$ and the rotational parameter a are constants. All quantities with the subscript g are the constant values of the variables at the boundary surface matching the exterior solution. Evidently, for $a = 0$, $\Phi_g^2 = 1$ the gravitational factor has the form of the Schwarzschild interior solution. The spacelike piece of this model is a cap of a sphere with radius $\mathcal{R}$ and the aperture angle η_g. The cap matches Flamm's paraboloid at $r_g = \mathcal{R}\sin\eta_g$.

The embedding for the spacelike piece of the Kerr model is

$$x^{0'} = \pm\sqrt{\mathcal{R}^2 - r^2}$$

$$x^{1'} = r\cos\vartheta$$

$$x^{2'} = A\sin\vartheta\cos\varphi \tag{7.4}$$

$$x^{3'} = A\sin\vartheta\sin\varphi$$

depicted in **Figure 16**.
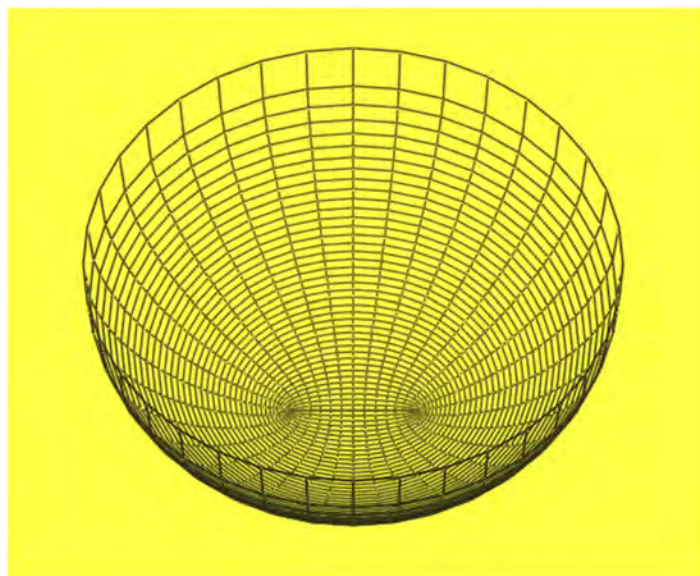
Figure 16. The interior Kerr geometry.

From this surface a band has to be cut off and the remaining surface has to be matched horizontally to the auxiliary surface of the Kerr metric. $\mathcal{R}$ is the radius of the circular arc at the minor axes of the ellipses. All individual 'radial' curves have hyperbolic contributions in their properties. For $r = 0, A = a$ the horizontal ellipses reduce to a distance which is clamped by the common foci of the ellipses. If one now adds the third dimension, these points rotate through φ. For $\vartheta = \pi/2$ a circle emerges. The radius of curvature of the ellipses is zero on this circle and the assigned field strengths are infinitely large. This is the Kerr ring singularity.

Since the junction condition is satisfied, both solutions, the interior and the exterior, match, as can be seen in Figure 17. The Kerr interior shows centrifugal, Coriolis, and gravitational forces, which can be geometrically explained as we have done with the forces of the exterior solution. The interior has a complicated stress-energy-momentum tensor, consisting of gravitational energy, current, and stresses. All that is treated in [5] [6] in detail.
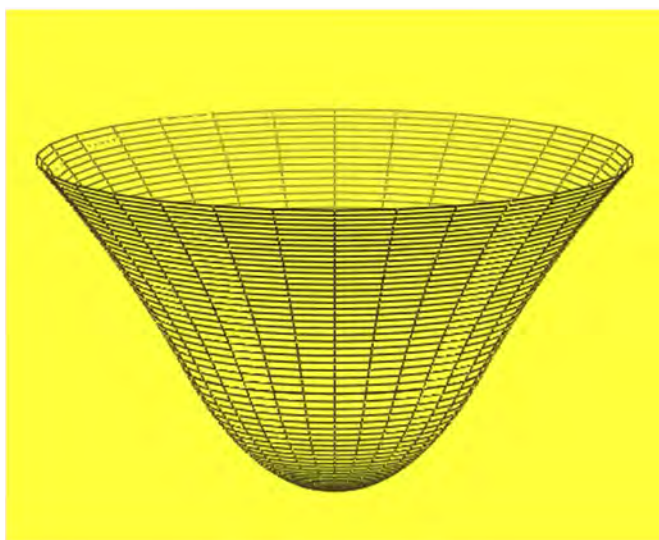
Figure 17. The complete Kerr solution.

8. Summary

We have revisited the Kerr model with the methods of tetrads. These are orthogonal local reference systems. The components of the field quantities represented in these systems are measurable quantities and have a clear geometrical or physical meaning. We have visualized the curvature of space with surfaces and have demonstrated how these quantities emanate from geometrical structures with several drawings.

In addition, we have separated the quantities B, C, and C describing the curvature of the elliptic-hyperbolic system from the physical quantities E, F, Ω, and D describing the physical content of the model. We have shown that the field equations of these physical quantities satisfy Maxwell-like equations. Thus, there is hope for a better understanding of the Kerr model.

Conflicts of Interest

The author declares no conflicts of interest regarding the publication of this paper.

References

[1] Kerr, R. P. (1963) *Phys. Rev. Lett.* **11**, 237-238.
https://doi.org/10.1103/PhysRevLett.11.237

[2] Boyer, R. H., Lindquist, R. W. (1965) *Proc. Camb. Phil. Soc.* **61**, 531

[3] Enderlein, J. (1997) Am. J. Phys. 65, 897-902.
https://doi.org/10.1016/0003-4916(78)90079-9

[4] Krasinski A. (1978) *Ann. Phys.* **112**, 22-40.
https://doi.org/ 10.1016/0003-4916(78)90079-9

[5] Burghardt, R. (2005) Spacetime Curvature.
http://members.wavenet.at/arg/EMono.htm

[6] Burghardt, R. (2005) Raumkrümmung. http://members.wavenet.at/arg/Mono.htm

[7] Sharp, N. A. (1981) *Can. J. Phys.* **59**, 688-692. https://doi.org/10.1139/p81-086

[8] Misner, C. W., Thorne K. S., Wheeler J. A., (1973) Gravitation, San Francisco.

[9] Burghardt, R. (2015) *Journ. Mod. Phys.* 6, 1895-1907.
https://doi.org/10.4236/jmp.2015.613195

[10] Mitra, A., (2006) Black Holes or Eternally Collapsing Objects: A Revue of 90 Years of Misconception. Focus of Black Hole Research. Nova Science Publishers, New York, 1-97.

[11] Burghardt, R. (2007) *Sitz. Ber. Leib. Soz. Wiss.* **92**, 51-60.
http://members.wavenet.at/arg/WKerr7.pdf

[12] Burghardt, R. (2007) *Sitz. Ber. Leib. Soz. Wiss.* **92**, 61-70,
http://members.wavenet.at/arg/WKerr8.pdf

[13] Lense, J., Thirring H. (1918) *Phys. Z.* **19**, 156-163.

[14] Thirring, H. (1918) *Phys. Z.* **19**, 33-39.

[15] Thirring, H. (1921) *Phys. Z.* **22**, 29-30.

[16] Thirring, H. (1918) Phys. Z. **19**, 204-205.

[17] Hund, F. (1947). *Z. f. Phys.* **124**, 742-756.

Reviewing Michelson Interferometer Experiment and Measuring the Speed of Starlight

Jingshown Wu[1*], Hen-Wai Tsao[1], Yen-Ru Huang[2]

[1]Department of Electrical Engineering, National Taiwan University, Taipei, Taiwan
[2]Materials and Electro-Optics Research Divisions, National Chung-Shan Institute of Science and Technology, Taoyuan, Taiwan
Email: *wujsh@ntu.edu.tw

Abstract

The wave-aether model was proposed long time ago. We study Michelson interferometer experiment and find that its theoretical calculation erroneously neglected the aether drag effect. We take the drag effect into account and reanalyze the theoretical interference pattern shift. The result is null because the drag coefficient of aether is zero. Such that the wave-aether model fulfills all light propagation characteristics. We design and implement a system to measure the starlight speed by comparing to that from a local source. We observe that the arrival times are different. It implies the apparent speeds of starlights are not equal to *c*.

Keywords

Wave-Aether Model, Michelson Interferometer, Speed of Light

1. Introduction

The speed and the propagation model of light are interesting subjects. The speed of light was considered as a very important physical parameter which is used to estimate the distance, mass etceteras. A few propagation models have been proposed since the ancient days [1] [2] [3] [4]. Among them, the wave-aether model attracts most attention, because this model satisfies many light propagation characteristics such as polarization, refraction, diffraction, interference, stellar aberration, etceteras. However, this model involved the existence and drag effect of aether [1] [3] [4] [5] [6]. Michelson-Morley used an interferometer to test the aether wind and they obtained a null result of interference pattern shift [1] [3] [4] [5]. The theoretical calculation gave a significant interference shift value.

Both are inconsistent, which was a major obstacle for the wave-aether model. Because the Michelson-Morley experiment is an important milestone in modern physics, it still attracts some attention recently [6] [7] [8].

Lorentz and others proposed a hypothesis that the length of a moving object along its motion direction contracted by the factor of $\left(1 - v^2/c^2\right)^{\frac{1}{2}}$, then the original Michelson's calculation interference pattern shift value agreed with the measured data [1]. In 1932, Kennedy and Thorndike performed an experiment using different arm lengths of an interferometer to test the Lorentz-Fizeau contraction [9]. The result showed the contraction might exist. Most people therefore gradually forgot and even abandoned this model.

In 1818, Fresnel predicted that the light would be dragged by the luminiferous medium [1] [2]. In 1725, Bradley discovered the stellar aberration. Fizeau and others used an apparatus to confirm the drag effect and the drag coefficient [1]. Now let us review Michelson's theoretical interference pattern shift calculation. We find that in his calculation, the drag effect was neglected, which yielded a significant shift value. When we take the drag effect into account to reanalyze the theoretical pattern shift value, we obtain a null result. So the measured data and the theoretical value are consistent. Thus we remove the major obstacle of the wave-aether model which now satisfies all light propagation characteristics. We may say that the wave-aether model is well-suited for describing the light propagation.

According to the wave-aether model, the motion of a light source will not communicate to the light speed *i.e.* the velocity of the light source is irrelevant to the speed of light but it will change the spectrum and wavelength.

Many observations and experiments have used moving light sources to test or prove the constancy of the speed of light.

In 1913, W. de Sitter observed some binary stars [10]. He concluded that the speed of light is independent of the speed of the light source and therefore the speed of light is constant. The wave-aether model explains his first conclusion. However, he did not consider the motion of the earth. The constancy of the speed of light conclusion conflicts with the wave-aether model and further evaluation is needed.

Around spring equinox each year, the earth is leaving away from Capella, Aldebaran, and Betelgeuse but approaching to Vega. We assume that the earth is moving in the aether, the starlight propagates with speed c in the aether. We setup a system including a transmitter and a receiver. The transmitter simultaneously modulates starlight and light from a local source into pulses. These pulses are detected by a distant receiver. We compare the arrival times of these two kinds of pulses. However, the receiver has relative motion with respect to the aether, the apparent speed of starlight may be related to the motion of the earth according the wave-aether model. We find the arrival times are different. The system setup and measurement will be described in Section 3.

2. Michelson-Morley Experiment and Aether Wind

Michelson invented the interferometer to test the aether wind. **Figure 1** shows the sketch of Michelson interferometer [1].

The two arms of Michelson interferometer are perpendicular. The length of the first arm is l_1 and a second one is l_2. The light from the source is incident upon the beam splitter B which splits the light into two parts. Assume that the thickness of the beam splitter is zero. One part of light travels along the first arm and is reflected back by the mirror M1. Then it travels along the same path and partially reflected by the beam splitter B incident upon the observer. According to Michelson calculation, the round trip time is

$$t_1 = \frac{l_1}{c-v} + \frac{l_1}{c+v} = \frac{2l_1}{c^2 - v^2} \tag{1}$$

where v is velocity of the aether wind [1].

Similarly the round trip time along the second arm is

$$t_2 = \frac{2l_2}{\left(c^2 - v^2\right)^{\frac{1}{2}}} \tag{2}$$

Note that in the nineteenth century, the fluid mechanics was well developed and understood. The velocity of wave propagating in a fluid current, e.g. flowing water in a river, is vector addition. Probably, Michelson adopted the concept of fluid mechanics to formulate the light wave travelling times expressed as (1) and (2) which had neither theoretical basis nor experimental evidence.

The time difference of t_1 and t_2 is

$$\Delta = t_1 - t_2 \approx \frac{2\left(l_1 - l_2\right)}{c} + \frac{2l_1 v^2}{c^3} - \frac{l_2 v^2}{c^3} \tag{3}$$

As shown in **Figure 1**, the aether wind blows along l_1, we turn the interferometer 90°, the aether wind will blow along l_2, such that the round trip times along l_1 and l_2, *i.e.* t_1 and t_1, will be reversed and become t_1' and t_2'. Now the time difference is
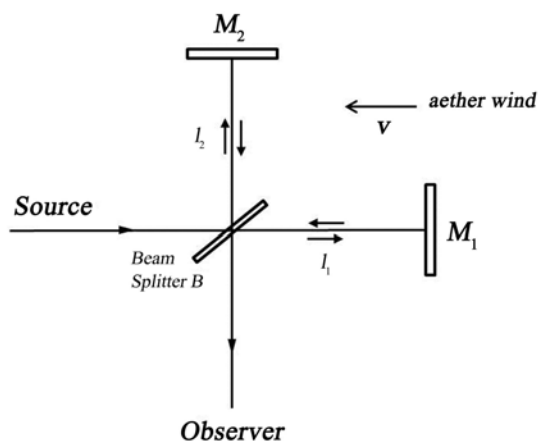
Figure 1. Sketch of Michelson interferometer.

$$\Delta' = t_1' - t_2' \approx \frac{2(l_1 - l_2)}{c} + \frac{l_1 v^2}{c^3} - \frac{2l_2 v^2}{c^3} \tag{4}$$

The difference $\Delta - \Delta'$ would yield an interference pattern shift by δ fringes

$$\delta = \frac{c(\Delta - \Delta')}{\lambda} = \frac{(l_1 - l_2) v^2}{\lambda c^2} \tag{5}$$

If $l_1 = l_2$, then

$$\delta = \frac{2(v/c)^2}{\lambda/l} \tag{6}$$

where λ is the wavelength, v is the orbit speed of the earth [1].

Michelson used light with $\lambda = 6 \times 10^{-7}\,\text{m}$, $l = 1.2\,\text{m}$.

Then according to (6) [1]:

$\delta = 0.04$ fringes.

However, Michelson didn't observe this interference pattern shift. Later Michelson and Morley extended the arm length to 11.0 m to have more accurate result. They obtained 0.01 fringes. The theoretical interference shift is 0.40 fringes *i.e.* the difference of the theoretical value and the experimental data is ever bigger [1]. In about next three decades, many physicists used various arm lengths and still observed no significant interference pattern shift [1] [3] [4]. In those days, many physicists including Lorentz, etceteras believed that the aether might exist and the earth truly moved in the aether [1]. The mother nature had a magical power thus that the length of a moving object along its moving direction with respect to the aether contracted by a factor of $\left(1 - v^2/c^2\right)^{\frac{1}{2}}$ [1].

Then (1) became

$$t_1 = \frac{2l_1}{\left(c^2 - v^2\right)^{\frac{1}{2}}} \tag{7}$$

and t_2 remained unchange as

$$t_2 = \frac{2l_2}{\left(c^2 - v^2\right)^{\frac{1}{2}}} \tag{8}$$

Therefore

$$\Delta = \Delta' \tag{9}$$

The theoretical value agreed with the experimental data.

In 1727, Bradley discovered the stellar aberration of γ-Draconis [11]. In 1871, Airy used a telescope in which the whole tube was filled with water, to observe the stellar aberration then he found the light drag effect, and gave the drag coefficient as [1] [11]

$$f = 1 - \frac{1}{n^2} \tag{10}$$

which is known as Fresnel's drag coefficient, n is the refractive index.

Fizeau designed the apparatus as shown in **Figure 2** to affirm the drag coeffi-

cient as expressed in (10) [1]. For air, $n = 1.0003$, the drag coefficient is 0.0006. Imagine that if we fill the tubes of Fizeau's apparatus by a luminiferous medium with unit refractive index, such as aether, then $f = 0$.

Based on previous discussion, readers may be aware of that using interferometer to test aether wind will yield a null result. Bearing the drag effect in mind *i.e.* $n = 1$, $f = 0$, we rewrite (1) and (2) as

$$t_1 = \frac{l_1}{\dfrac{c}{n} - vf} + \frac{l_1}{\dfrac{c}{n} + vf} = \frac{2l_1}{c} \tag{11}$$

and

$$t_2 = \frac{l_1}{\left(\dfrac{c^2}{n^2} - v^2 f^2\right)^{1/2}} = \frac{2l_2}{c} \tag{12}$$

(11) and (12) show that the round trip times of lights travelling along the two arms are irrelevant to the velocity of aether wind. The theoretical value and the experimental data are consistent. The wave-aether model therefore fulfills all light propagation characteristics such as interference, polarization, stellar aberration, especially the null result of Michelson interferometer experiment.

In other words, the wave-aether model should be valid. Based on the wave-aether model, we design a system and perform the experiment to measure the speed of starlight.

3. Measuring the Speed of Starlights

In the wave-aether model, the speed of light is irrelevant to the speed of the source but is influenced by the motion of the observer. The principle of our measurement system is simple. We use a chopper to modulate the continuous starlight ray and a local light ray into pulses. The speed of the local light, c, is known [12]. We compare the arrival times of the starlight pulses and the local light pulses at the receiver. Then we can obtain the speeds of the starlights.

Figure 3 shows the latter version of this experimental setup. At the transmitter, for the main optical path, we use the Lulin One-meter Telescope (LOT) to collect the starlight. The first end of a multimode optical fiber is placed at the focal point of LOT and the other end is firmly fixed at the focal point of the off-axis parabolic mirror P1. The collimating ray is incident on the rotating mirror, M1, and then is incident on a second off-axis parabolic mirror P2. A 100 μm wide slit is put at the cofocal point of P2 and the third off-axis parabolic mirror P3 which makes the ray collimating again. When M1 spins, light pulses are generated after the slit. These pulses travel along the path P3, M2, M3, P4 and P5 then are incident on the photomultiplier tube (PMT) which converts the light pulses into electrical pulses. The end of the pigtail of an infaray light source is fixed at T1 to have a collimating ray which is merged into the main optical path by the beam splitter B1. After M1, the beam splitter B2 separates the infaray

which is focalized at the end of another multimode fiber in T2. The multimode fiber plays as a slit and transmits the infaray pulses. At the receiver, the photodiode (O/E) converts the infaray pulses into electrical pulses as used for the reference and the trigger in the oscilloscope. The total distance from the transmitter to the receiver is 4302 m. During the measurement, we alternately connect the first end of the multimode fiber to the LOT and the white light source to calibrate the system. We measured the arrival time of the light pulses from Capella, Aldebaran, Betelgense, and Vega in 2010, 2011, 2012, 2013 and 2014.

The details of the measurement setup, operation, data analysis, calibration, are described in References [13] [14] [15] [16].

Table 1 lists the delays of the starlight pulses respect to the white light pulses, which shows the arrival times of the starlight pulses different from the white light pulses. Note that negative delay of the starlight pulses implies that the speed of the starlight is faster than c and positive delay indicates the speed of the starlight is slower than c. The trends of these results are roughly consistent with the wave-aether model qualitatively. Vega is approaching to the earth, so the negative delay with respect to the local white light was obtained. The delays were positive when the stars are leaving away from the earth, such as Capella, Betelgeuse, and Aldebaran. The orbital speed of the earth is about 30 km/s on the ecliptic plane, so the delay is estimated about 1.4 ns. The variation of measured delays may be caused by the system errors from temperature, humidity, and air dispersion [16], but the trends remain the same over the years.

Table 1. The delays of the starlight pulses with respect to the local white light pulses (unit: ns).

Date	The delays of the starlight pulses (ns)			
	Capella	Betelgeuse	Aldebaran	Vega
2010/3/15	1.61			
2010/3/16	2.1/1.5			
2010/3/18	3.9	1.2		−3.2
2011/2/28	3.0/2.7	1.8		−7.4
2011/3/4	2.5			
2011/3/12	3.8			
2012/2/18	4.6			
2013/3/8			2.1	−1.3
2013/3/9			2.2	−1.9
2013/3/12	1.2			
2014/1/20	1.4		1.8	
2014/1/22			1.9/2.2	
2014/1/23			2.1	
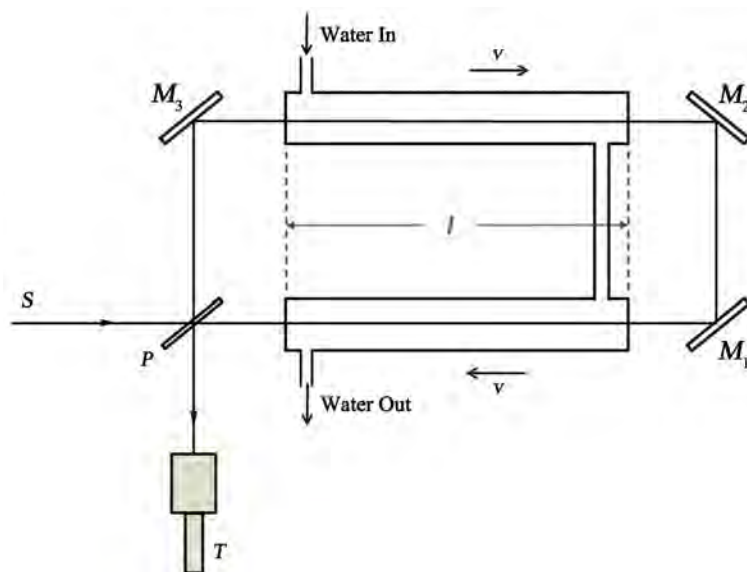
Figure 2. Sketch of Fizeau's drag apparatus.
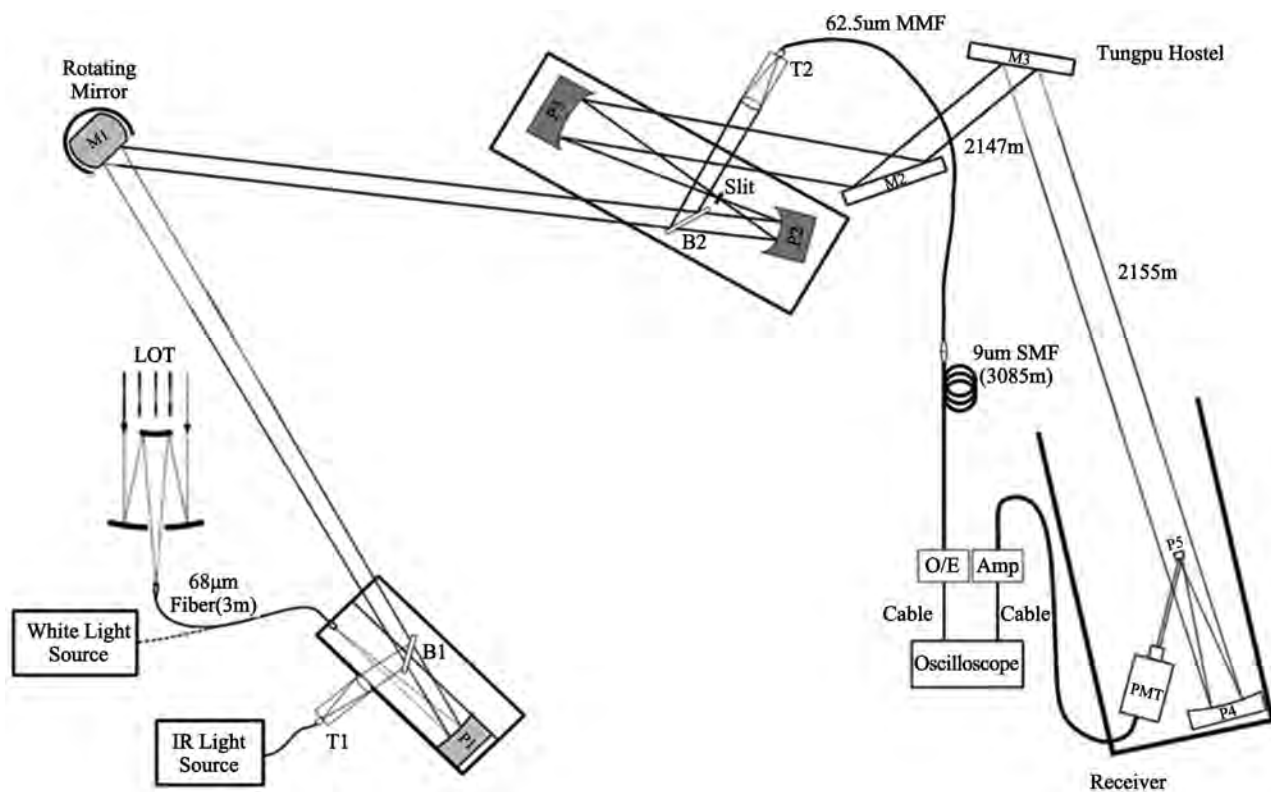
Figure 3. Sketch of the latter version of the experiment setup.

4. Conclusions

We study Michelson interferometer experiment and search the causes of disputation between the experimentally measured null interference pattern shift and the significant theoretical calculation value. We find that Michelson formulated the light travelling times along the two arms of the interferometer neglecting the

drag effect. We take the drag coefficient into account to reanalyze the theoretical interference pattern shift value and obtain a null result. We prove that the measured data and the theoretical value match very well. Previously the disputation of Michelson interference pattern shift is a major concern of the validation of the wave-aether model for light propagation. Now this issue is solved and the wave-aether model satisfies all light propagation characteristics such as straight line transmission, polarization refraction, etceteras. We can conclude that the wave-aether model is valid.

Based on the wave-aether model, we consider that the earth moves in the aether. We setup a system on the earth to measure the speed of starlight *i.e.* the system moves in the stationary aether. Because the system including the observer is moving, the apparent measured speed of the starlight may not be equal to *c*. we design a transmitter to modulate the starlight and the light from a local source into pulses. Note that the speed of the local light pulses is *c*, these starlight and the local light pulses travel over a distance and reach the receiver. We compare the arrival times of these two kinds of pulses. We find that the arrival time of the starlight pulse is different with that of the local light pulse. It indicates that the apparent measured speeds of the starlight vary from the well known *c*. In general, our experiment fits the wave-aether model well qualitatively.

Acknowledgements

Supporting Information

Conflicts of Interest

The authors declare no conflicts of interest regarding the publication of this paper.

References

[1] French, A.P. (1968) Special Relativity. W. W. Norton & Company Inc., New York.

[2] Huygens, C. (1690) Treatise on Light.

[3] Cassidy, D.C., Holton, G. and Rutherford, F.J. (2002) Understanding Physics, Birkhaiiser.

[4] Panofsky, W.K.H. and Phillips, M. (1962) Classical Electricity and Magnetism. 2nd Edition, Addison-Wesley, Boston.

[5] Consoli, M., Matheson, C. and Pluchino, A. (2013) *The European Physical Journal Plus*, **128**, 71. https://doi.org/10.1140/epjp/i2013-13071-7

[6] Consoli, M., Pluchino, A. and Rapisarda, A. (2016) *EPL*, **113**, Article ID: 19001. https://doi.org/10.1209/0295-5075/113/19001

[7] Smid, T. (2017) *European Journal of Physics*, **38**, Article ID: 065302. https://doi.org/10.1088/1361-6404/aa82f8

[8] Su, C.-C. (2001) *EPL*, **56**, 468. https://doi.org/10.1209/epl/i2001-00502-1

[9] Kennedy, R.J. and Thorndike, E.M. (1932) *Physical Review*, **42**, 400. https://doi.org/10.1103/PhysRev.42.400

[10] de Sitter, W. (1913) *Proceedings of the Royal Netherlands Academy of Arts and Sciences*, **15**, 1297.

[11] Bradley, J. (1729) *Philosophical Transactions of the Royal Society*, **35**, 637.

[12] Froome, K.D. and Essen, L. (1969) The Velocity of Light of Radio Waves. Academic Press, New York.

[13] Wu, J., Huang, Y.-R., Chang, S.-T., Tsao, H.-W., Lee, S.-L. and Lin, W.-C. (2016) *Springer Proceedings in Physics*, **177**, 81.

[14] Wu, J., Chang, S.-T., Tsao, H.-W., Huang, Y.-R., Lee, S.-L., *et al.* (2013) *Proceedings of SPIE*, **8832**, Article ID: 883203. https://doi.org/10.1117/12.2023127

[15] Huang, Y.-R., Wu, J., Chang, S.-T., Tsao, H.-W., Lee, S.-L. and Lin, W.-C. (2014) *JPS Conference Proceedings*, **1**, Article ID: 014019.

[16] Huang, Y.-R. (2012) Measurement of Differences and Relativity between Speeds of Light from Various Stars. PhD Dissertation, National Taiwan University of Science and Technology.

Missing Mass and Galactic Dust with a Size Greater than 200 Microns, Minimum Size of the Micrometric Dust around the Sun

Marc Mignonat

Société d'Astronomie des Pyrénées Occidentales, Pau, France
Email: mmignonat@libertysurf.fr

Abstract

The studies of the glaciologists show that, since 30,000 years, the Earth receives every year approximately 40,000 tons of dust, dust with an average size about 200 microns. By determining of which volume these 40,000 T come and by showing that the density of this volume is significant within the density of the milky way, I have tried to estimate the mass of dust contained in the Galaxy. To support that this density close to earth is representative, arguments are given: 1) the distribution of great dust is largely homogeneous in the galaxy (what does not exclude the existence of gas or dust clouds with different densities in the milky way); 2) there would be a minimum size that I have calculated for micrometeorites in the solar environment, and so there would be a lack of the micrometeorites with a size between 5 and 50 microns. So the density would not be greater in the solar system. Next, a very simple rough calculation (as the one made by the observatory of Paris in 1910) allows estimating this mass near 4 times that of the dark matter. So, the interstellar dust with a large size (>200 μ) could it be the missing mass? A verification method is proposed to confirm or refute this hypothesis.

Keywords

Dark Matter, Dust, Galaxies: ISM

1. Introduction

Every year, the Earth receives 40,000 T of dust and this figure has not varied since at least 30,000 years [1]. A study, in 2016 [2] of the marine sediments shows there is not variation of this value since about 40 million years with a maximum at the end of Eocene (35 Myr) and at the end of Miocene (8.2 Myr).

In her thesis of 2010, Dobriča [3] specifies that on every m², it falls an average of one micrometeorite every year (or 30.000 tons against only 10 tons of macroscopic meteorites). They are too small so that we notice it (their size is about 200 microns). For example, during a collection in Antarctica in 2006, in 24 m³ of the filtered snow were extracted more than 1300 micrometeorites. This average size of 200 microns does not correspond to what we suppose on the dark matter.

The dark matter is a category of hypothetical matter, used to explain astrophysical observations where there is a missing mass, (for instance the element abundances predicted by nucleosynthesis, the detailed form of anisotropies in the cosmic microwave background particularly at redshift 1000, the estimations of mass of the galaxies and of the clusters of galaxies to promote the initial structure formation). But we can note that, in all these "particulate" or "gaseous" observations, we do not find measures about dust greater than the micron.

Various hypotheses are explored on the composition of dark matter: molecular gas, dead stars, brown dwarfs in large numbers, black holes, etc. As we do not find enough visible matter, astrophysicists suppose a non baryonic matter with other particles, (e.g. neutrinos, axions, perhaps superpartners such as the neutralino). These other particles are grouped in the generic name of "WIMP".

The MOND theory is an alternative recipe for the missing mass [4]. This theory says that this dark matter would not exist, and makes the hypothesis that its existence would be due to a partial ignorance of laws of gravity.

Astrophysicists like Magnan, [5] consider that dark matter does not exist, that it is an error resulting from a too big uncertainty which exists on the measures of speeds and masses within the galaxies.

So, I had the curiosity to try to estimate the global mass of the dust in the Galaxy with the approach used by the observatory of Paris in 1910 and compare it with the mass of the dark matter. But first, we have to know if the density in the solar environment would be representative of that of the Galaxy. For that, we have to question the homogeneous distribution of dust and see if the size of dust would be representative.

2. Dust Distribution in the Galaxy and Size of Dust

2.1. Global Homogeneity in the Galaxy

1) The calculation, resulting from the observation (estimation in 1910 of 10,000 T/year on the Earth [6]), gives an absorption of 2 magnitude by Kpc (what means that a star situated near the galactic center in 8.5 Kpc undergoes an extinction about 16 magnitudes and thus is often invisible). This extinction, proportional to the distance, involves a homogeneous distribution of the dusts between us and the galactic center.

2) We can cite the thesis of e.g. Arab [7] about the evolution of interstellar dust. In this exhaustive thesis, he considers that the interstellar medium is constituted by all the matter filling the space between the stars. This matter is made of an extremely tenuous mixture of gas and dust of an atom/cm³. The dusts are

solid particles with a size between the nanometer and the micron. Their small size near the wavelengths of emission (<100 nm) explains their hotter temperatures or around 17 k or around 30 k. There is a homogeneous distribution but the dusts with a size greater than the micron are not considered.

3) Zagury [8] already finds incompatibilities between the standard theory of the interstellar extinction and the observations. With the observations resulting from the International Ultraviolet satellite, the extinction in the UV spectrum with the 2200 Å bump, .was studied for the nebulae, and in directions of low and very low reddening. It is found that extinction occurs linear function from the near IR to the extreme UV, what is incompatible with the standard theory of the interstellar extinction. He notes that the observation of the reddened light from the stars, is contaminated by the diffused light with a very low angle of diffusion. He says this questions all the models of dust actually used since the consequence is that there are no differences in average properties of the interstellar dust in different directions. It is always written that "the interstellar dust represents a very low part of the interstellar matter, essentially gaseous". The quantity of dust is constant, most probably because the distribution of the dust is at first glance, homogeneous within the Galaxy.

4) Studies [9] [10] show an agitation of the dust and suggest a fragmentation of the clouds of gas: on a line of sight, it is noticed that the intensity of the absorption lines of H_2CO varies from one year to the next (the recording was made during 18 years). It suggests turbulent movements of the interstellar matter which cause a slow renewal on the line of sight which the authors attribute to the movement of the earth around the sun and to the movement of the sun in the Galaxy (20 km·s^{-1} in the direction defined by $\alpha \approx 18$ h and $\delta \approx 30°$). But even if the gaseous concentrations are variable, for the authors, "It seems thus finally that in this type of cloud, the dusts are distributed in a relatively uniform way and that there are no strong fluctuations".

2.2. Size of the Dust

1) The old studies of the 1950s, for the particles "very large relative to the wavelength", determined from the measures of the color indices [11], and from the ratios of the absorption coefficients that there was no place for neutral absorption in the milky way [12]. However, there were few isolated studies as that of Alter [13] which, depending on the galactic longitude, found a larger coefficient of 0.83 mag/Kpc (instead of 0.17), which required a much higher mass of dust. The conclusion by Delay in 1954 [14] of these studies is that, from the study of the only absorption it is impossible to deduce what is the nature of the particles responsible for the absorption.

2) It is written in 1946 that the dust cannot exceed a few thousand of angstrom [15]. Gyngard [16] finds 25 microns in 2018 or Gregory in 2005 [17] gives an approximate mass of 10^{-17} kg. The reason of the small size of the particles is explained by a balance between the growth of grains possible for every atom except H and He when the temperature is greater than 10 - 20°K and the

destruction by shocks or evaporation [15].

3) Also old studies show that the radiation pressure Pr on particles much larger than the wavelength prevent the presence in space of particles of few tens of microns. The particles are in balance between the radiation pressure Pr and the gravitational force Fg; these two forces diminish with the square of the distance, so the ratio between Pr and Fg is constant [14]; when Pr overcomes, the grains are pushed back to several parsecs from the star [18].

4) It is, however, interesting to determine the minimum radius r of grains that will not be pushed back and will remain in the solar environment. A simple calculation (see calculation in Appendix) allows setting the minimum radius r to $r = 3\sigma T^4 R_0 / 8 G M_0 \rho$ (with σ constant of Stefan, T temperature of the star, Ro radius of the star with a mass Mo, G constant of gravitation and ρ density of the grain); for the sun, $r \approx 120\rho$ (so a radius of 120 μ or a size around 240 μ for an object with density 1, a size of 64 μ for a chondrite with a density 3.8 or 50 μ for a siderite with density 4.8). This minimum size is in conformity with the samples taken by Dobrica in Antarctica(3), as well as the latest studies from the Cassini spacecraft with the collection of 36 micrometeorites from outside the solar system [19] and from the collection of dust in 2017 on the rooftops of several European cities [20].

2.3. Finally about Homogeneity and Size

From these studies cited above in paragraphs 2-1 and 2-2, it appears: first, it is reasonable to believe that the distribution of the dust is globally homogeneous (what does not exclude the existence of gas or dust clouds) and that the observed rate of dust impinging the Earth is representative of the Galaxy. We can note that the recent hypotheses made only from the studies upon the gases (where we do not find dust greater than the micron) cannot explain the 40,000 T annually falling on the earth.

Second, there would be no a higher dust density around the sun since a category for dust is under-represented. The old studies show the difficulty in studying the neutral dust and determine for the small grains a maximum size near the wavelength. It is important to note that a minimum size of micrometeorites can also be calculated in the terrestrial environment. So, the particles of an approximate size between 6 and 50 μ would be under-represented. More specifically, taking into account the increasing density, there would be a gradual decrease of the quantity of dust from 240 μ to arrive at a near absence to a size of 50 μ (since only the particles with a density greater than 5 could be smaller). It is thus assumed that these particles of intermediate size would be more abundant at equidistance from the stars.

3. Approximate Calculation of the Mass of Dust of the Galaxy

3.1. At First, the Volume of the Galaxy Is to Determine

In the usual way for our Galaxy, its form can be approximated by an ellipsoid of

revolution whose the equatorial radius is $R' = 50{,}000$ ly and the polar radius R'' = 5000 ly. So, we obtain the volume Vg by multiplying twice the equatorial radius R' by the polar radius R''.

$$Vg = (4/3)\pi R'^2 \times R'' = 5 \times 10^{61}\,\mathrm{m}^3 \tag{1}$$

3.2. Secondly, It Is Necessary to Determine the Volumetric Concentration of the Dust of the Galaxy

For calculating this value, we have to estimate from which volume come the 40,000 T of dust, every year received by the earth.

The earth in one year, is going to sweep the volume of a torus whose the large radius R is the radius of the earth orbit and the small radius r of the torus is the radius of the sphere in which the attraction of the earth is applied. This radius r is difficult to estimate.

If we are considering that the dusts are in solar orbit, then it is necessary to take the maximal radius of gravitational influence, with the points of Lagrange L1 and L2 situated in approximately 0.01 UA = 1.5 millions km. But, this maximalist hypothesis can be ruled out because then, year after year, the Earth passing approximately in the same place, the collected quantity of dust would had decreased and approached zero.

A possible calculation to have the largest volume, is to consider that the component of the speed of the dust is zero in the plan of the ecliptic; and to take as maximal distance the time to go to the Earth during its time of passage. At a given point, we can supposed the earth have a maximal influence during its time of passage Tp. Tp = diameter/speed ≈ 12,000/30 = 400 s. This influence being inversely proportional to the square of the distance, we are going to avoid an integral calculation by making the approximation that the time of influence t will be multiplied by two, so t = 400 s × 2 = 800 s.

The concerned dust will go to the Earth during this journey of 800 s. Even by supposing the acceleration g of the gravity equal to that is to the surface of the earth, so g = 10 m·s^{-2} what is excessive, we arrive only at a traveled distance d of 3200 km (d = gt^2/2).

Then, we shall have, in priori a surface of sweeping in a high range by supposing a small radius of the torus of 9500 km swept by the earth. (A similar calculation had already been made in 1911 by Salet [6] of the Observatory of Paris who, trying to calculate the absorption from the quantity of dusts annually received by the earth (estimation in 1910 of 10,000 T every year), had made an estimation of the volume of space of which came these dust. He estimated the earth received the dust in a radius x/x^2 = 1.2 ρ^2 with ρ the radius of the earth and he multiplied by 5 the amount of dust to take into account the attraction of the sun. So, he had found an equivalent radius of 11,914 km what is lightly superior to the value I find, but in 1910, the galactic movement was not known and the sun was supposed motionless.

The volume of the torus Vt in which the dusts are collected by the earth is:

$$Vt = 2\pi r 2R = 2\pi 2\left(9.5 \times 10^6\right) 2 \times 1.5 \times 10^{11} \approx 2.7 \times 10^{26}\,\mathrm{m}^3.$$

So, the volumetric concentration ρg of the dusts in the space is:

$$\rho g = 4 \times 10^7 / 2.7 \times 10^{26} \approx 1.5 \times 10^{-19}\,\mathrm{kg \cdot m^{-3}} \tag{2}$$

This value is very high (we usually count for the interstellar space an atom by cm³ or approximately ($1.67 \times 10^{-21}\,\mathrm{kgm^{-3}}$).

3.3. The Total Mass Mt of the Dust in the Galaxy Can Be Estimated

$$(1)(2) \geq Mt = Vg \times \rho g \approx 7.5 \times 10^{42}\,\mathrm{kg}$$

The visible mass of the Galaxy is considered near $4 \times 10^{41}\,\mathrm{kg}$ [21] [22].

So, that of the dark matter, nearly 5 times larger, would be $2 \times 10^{42}\,\mathrm{kg}$, *i.e.* approximately 4 times smaller than the value that I have just calculated. However this value has the same order of magnitude.

4. Hypotheses and Conclusion

The orders of magnitude, obtained by the calculations that have just been made, invite reflection. They induce me to consider that the missing mass could be found with a much more elaborate classical gravitational calculation than the one I have just outlined, particularly with the inclusion of the detailed structure of the Galaxy, an improvement by the glaciologists or geologists of the calculation of the dust amount annually received by the Earth and the measurement in the space of the quantity of dust with a size greater than micrometer.

I am not the only one to question about the dark matter. But, perhaps, it is the first study which estimates the galactic dust mass from the dust (>200 μ) received by the Earth and in this study, I am assuming the distribution of dust in the Galaxy is globally homogeneous (what does not exclude local variations with great clouds of gas or dust). This global homogeneity, even if I have cited several studies in its favor, questions the standard theory of the interstellar extinction, so, we have to be prudent. Other reason is that I am supposing the dust comes from the outside of the solar system because the quantity of dust is constant since 40 million years, but 40 million years is not a long time on the astronomical scale.

We can note that the calculation allows finding that the mass would exceed the known values of the missing mass by at least four orders of magnitude. So, to explain this excess of matter, we have to suppose that, either we are by chance in an area of the Galaxy with a high density (it is unlikely), or the dust is mainly in the interplanetary zone (this area could go very far beyond the Oort cloud). It is then logical to think that this dust exists around each star. By multiplying this amount of interplanetary dust by the number of stars, we would then find more precisely the missing mass. This hypothesis has the advantage of preserving the mechanisms already known from the observations on galaxies and their formation.

A point for a hypothetical origin from the outside of the solar system is that the IR radiation of the dusts is larger in the galactic plan and no in the ecliptic plan (and so we could assume the maximum of micrometric dust is not in the ecliptic plan).

But the best verification about these hypotheses could be given by the collection directly in the space and, so by the measurement of the density of the dust inside the solar system. The minimal radius r of the dust in the solar environment would be around $r \approx 120 \mu / \rho$ (ρ = density of the micrometeorite).

And, if the dust is interplanetary, the density would be higher in the ecliptic plan; if the dust is coming from a region more distant from the solar system, so the density of the micrometric dust inside various points of the solar system (e.g. inside and outside of the ecliptic plane) would be approximately constant.

Conflicts of Interest

The author declares no conflicts of interest regarding the publication of this paper.

References

[1] Winckler, G. and Fischer, H. (2006) *Science*, **313**, 491.
https://doi.org/10.1126/science.1127469

[2] Chavrit, D., Moreira, M. and Moynier, F. (2016) *Earth and Planetary Science Letters*, **436**, 10-18.

[3] Dobriča, E. (2010) Micrométéorites concordia: Des neiges antartiques aux glaces cométaires. Thèse Paris 11 en partenariat avec Université Paris-Sud. Faculté des Sciences d'Orsay.

[4] Tortora, C., Jetzer, P. and Napolitano, N.R. (2012) Dark Matter and Alternative Recipes for the Missing Mass.

[5] Magnan, C. (2014) Le théorème du jardin.

[6] Salet, P. (1911) *Bulletin Astronomique*, **28**, 241-251.

[7] Arab, H. (2012) Evolutions des poussière interstellaires: Apport des données de l'observatoire spatial Herschel. Thèse, Université Paris Sud., Paris, XI.

[8] Zagury, F. (2000) *New Astronomy*, **5**, 285-298.

[9] Boissé, P. and Thoraval, S. (1990) La distribution des poussières à l'échelle de l'unité astronomique dans les nuages interstellaires. A and A 228, 483.

[10] Marscher and Als (1993) *Astrophysical Journal*, **419**, L101.
https://doi.org/10.1086/187147

[11] Stebbens, J. and Whitford, A.E. (1936) *Astrophysical Journal*, **84**, 132.
https://doi.org/10.1086/143755

[12] Greenstein, J.L. and Henyey, I.G. (1939) *Astrophysical Journal*, **89**, 647.
https://doi.org/10.1086/144088

[13] Alter, G. (1949) Memoirs and Observ. Czechoslovak astr. Soc., Prague, No. 10.

[14] Dufay, J. (1954) Nébuleuses galactiques et matière interstellaire. Albin Michel Ed., Paris.

[15] Oort, J.H. and Van de Hulst, H.C. (1946) *Bulletin of the Astronomical Institutes of the Netherlands*, **10**, 187.

[16] Gyngard, F., Jadhav, M., Nittler, L.R., Stroud, R.M. and Zinner, E. (2018) *Geochi-*

mica et Cosmochimica Acta, **221**, 60-86.

[17] Gregory, L. and Matloff, L.J. (2005) Applications of the Electrodynamic Tether to Iinterstellar Travel.

[18] Schalén, C. (1929) *Astronomische Nachrichten*, **236**, 249. https://doi.org/10.1002/asna.19292361602

[19] Altobelli, N. and Als (2016) *Science*, **352**, 312-318. https://doi.org/10.1126/science.aac6397

[20] Genge, M.J., Larsen, J., Van Ginneken, M. and Suttle, M.D. (2017) *Geology*, **45**, 119-122. https://doi.org/10.1130/G38352.1

[21] Andreas, Küpper, H.W., Balbinot, E., Bonaca, A., Johnston, K.V., Hogg, D.W., Kroupa, P. and Santiago, B.X. (2015) *Astrophysical Journal*, **803**, 80. https://doi.org/10.1088/0004-637X/803/2/80

[22] McMillan, P.J. (2011) *Monthly Notices of the Royal Astronomical Society*, **414**, 2446-2457. https://doi.org/10.1111/j.1365-2966.2011.18564.x

Appendix: Calculation of the Minimal Size of the Dust around a Star

We have a body A with a size much larger than the wavelengths of the electromagnetic waves emitted by the star (otherwise the calculations are not valid). The movement of this body A will be linked to the balance between the attraction force Fg of the star and the force Fr of the radiation flow from the star. The force Fr will be proportional to the surface of the body A exposed to the flow and will also depend on the albedo of A. We simplify the problem by considering that the body A is spherical with an average radius r and we do not consider the albedo. So, the surface of A which receive the energy is a hemisphere with a surface $\pi r^2/2$. The received energy Er by the body A is:

$E_r = \left(F_0 R_0^2 / R^2 \right)\left(\pi r^2/2 \right)$. $\left(F_0 R_0^2 / R^2 \right)$ is the stellar flux at the la distance R between the star and the body A (Fo: stellar flux at the stellar radius Ro). The gravitational energy E_g is: $E_g = \left(GM/R \right)\left(4\pi r^3 \rho/3 \right)$ with M mass of the star, G constant of gravitation, ρ density of the body A. By equalizing E_r and E_g and by posing $Fo = \sigma T^4$, we obtain: $r = 3\sigma T^4 R_0^2 / 8GMR\rho$ (3) with T temperature of the star, Ro radius of the star, σ = cte of Stefan. We want to calculate the minimum radius r that allows the movement of an object towards the star. In this case $R = Ro$, and so (3) becomes $r = 3\sigma T^4 R_0 / 8GM\rho$ (4) For the sun (4) can be written $r \approx 1.26 \times 10^{-4}/\rho$ meters or $r \approx 0.12\text{mm}/\rho$ (with $T = 5778\text{K}$, $Ro = 695.5 \times 10^6 \text{m}$, $M = 1.99 \times 10^{30}\text{kg}$).

A Quantum Representation of the Homogeneous 5D Manifold and the Perelman Mappings of 5D onto Non-Homogeneous Lorentz 4D Manifolds

Kai Wai Wong[1*], Peter Chin Wan Fung[2], Wan Ki Chow[3]

[1]Department of Physics and Astronomy, University of Kansas, Lawrence, USA
[2]Department of Physics and Centre on Behavioral Health, University of Hong Kong, Hong Kong, China
[3]Department of Building Services Engineering, The Hong Kong Polytechnic University, Hong Kong, China
Email: *kww88ng@gmail.com

Abstract

The expression of the Maxwell magnetic monopole was employed to correlate the space to space projection that gives rise to the Gell-Mann standard model, and space to time projection which gives the leptons; and how does it correlate to the Perelman mappings from the homogeneous 5D manifold to the Lorentz 4D manifold, together with correlating the physical consequences caused by the breaking of the Diagonal Long Range Order [DLRO] of the monopoles quantum states affected by the motion of massive particles in the Lorentz 4D boundary of the 5D manifold, which leads to gravitons and the gravity field via the General Relativity covariant Riemannian 4D curvatures metric equation.

Keywords

5D Homogeneous Manifold, Perelman Mappings, Magnetic Monopoles, Space Projections and Topological Symmetries, Covariant Riemannian Curvature and Gravity

1. Introduction

The homogeneous 5D manifold was presented several years back [1] to explain mainly how the Gell-Mann standard model [2] can be created from the homogeneous symmetry breaking via space dimension reduction projections. The quantitative results derived for the hadrons were subsequently reported [3] [4] [5]. However, there remains mathematical gaps without more investigations into

the correlations between the quantum picture and the Perelman topological mappings [6] [7] [8]. To start with, we revisit the properties of fields in the homogeneous 5D manifold.

The homogeneous 5D manifold obeys Fermat's Last Theorem [9].

$$[ct]^2 = r^2. \tag{1.1}$$

Any energy expressed in terms of $2h\nu$, would generate a monopole of strength $\pm 2ec$ [10] [11] outward along "r", leading to the 5th component Maxwell magnetic monopole, with strength $M = 2ec$, at $r = 0$, potential

$$\pm 2 \frac{\vec{M}\mu}{r}. \tag{1.2}$$

The factor 2 comes from total spin 0 degeneracy of the pair of $e, p, s; -e, -p, -s$, where s is up or down spin of the massless spinors, and momentum p is along r such that this $\vec{M}$ state is in the DLRO and μ is the magnetic permeability. The potential has the conventional unit of Joule.

In order to understand properly the process of physical generation of mass and charges from the homogeneous 5D space-time manifold, it is essential to first construct this 5th component of the Maxwell magnetic monopole potential.

The 5D homogeneous space-time manifold, together with the uncertainty principle, results in the presence of 5 vector components potential fields. The first 4 vector potentials $A(0)$ to $A(3)$ are those of the Maxwell electro-magnetic vector potentials, while the 5th component $A(4)$ is explicitly derived recently for the representation of the 5D as specified by the massless spinor fields expressible in tU3D × 1D [11]. Topologically, the Maxwell potentials can be represented by a product of two domains: 4D × 1D, such that the monopole potential is orthogonal to the other 4 Maxwell vector potentials, which was originally coined by Maxwell as the magnetic mono-potential [10], and expressed in the recent Physics Essays paper as positive and negative outward spherical radial (generalized) current with a strength of $M = 2ec$, having the unit of ampere-meter. In fact $A(4)$ does not have the same dimension as $A(0)$ to $A(3)$, although the potential energy $MA(4)$ must be the same in unit as $eA(0)$. This magnetic monopole can be viewed as a combination of numerous M vectors propagating outward along all radial unit vectors at the same rate c, while the 5D manifold expands. Therefore, it carries any momentum $\dfrac{h\vec{v}'}{c}$ where $\vec{v}'$ has no relationship to the frequency v of the pair of charged massless spinors, with its values only dictated by the Fermat's amplitude r, like the photon that may be emitted from the Coulomb potentials and also obeys Gauss Theorem, with the $\vec{M}$ vector replacing the electric field vector $\vec{E}$. These monopole strengths M arise from the outward radial currents due to opposite momentum pairs of $e, -e$ massless spinors created from pure energy, where the massless charges $e, -e$ represent the coupling constants between the vector fields and the spinor fields solutions of the equation with the homogeneous 5D energy-momentum quadratic operator acting on the wave function of the system. Such that these vector and spinor fields obey gauge invariance. Hence, $\vec{M}$ and $-\vec{M}$ are quantum Bosons composed of 3D

radial outward massless $e, p, s; -e, -p, -s$ current states naturally created from energy at the center of the 5D manifold. As long as the 5D manifold is not totally enclosed by matter, the vectors $\vec{M}$ and $-\vec{M}$ and hence the magnetic monopole will exist. Mathematically, these vectors $\vec{M}$ and $-\vec{M}$ are massless bosonic states with strength $2ec$ that represents the magnetic monopole. In fact, the constituent vectors representing the monopole expand spherically outward like photons in the 4D homogeneous EM space-time manifold, except they carry only energy with arbitrary momentum, only fixed by the b.c. of the Fermat's amplitude *r*. Hence they must be in the Diagonal Long Range Order (DLRO) Bose-Einstein (BE) condensate state. Because of this B.E. ground state, we could also see certain similarities between a 4D space-time manifold with the *M* and $-M$ Bose condensate states and the Higg's theory Bose-Einstein condensed ground state/vacuum filled with Higgs fields [12]. Of course the premises of these two theories are quite different.

Should we be able to add a net linear momentum, from the motion of a massive nuclear in the $r = 0$ 5D frame, with charge 0 or *q* to the monopole inducing current magnitude *M* and $-M$, The currents generating magnetic field will be replaced by $q\vec{v} + \vec{M}N(+)$ and $q\vec{v} - \vec{M}N(-)$, where $\vec{v}$ is the velocity of charge *q*. Where $N(+)$ and $N(-)$ are the energy integrated weight factors, then these two opposite magnetic monopoles will give raise to an attractive quantum well in the 5D manifold, as it changes the monopole strength to $M' = q\vec{v} + \vec{M}N(+)$ and $-\vec{M}'' = q\vec{v} - \vec{M}N(-)$ Where $\vec{v}$ need not be along "*r*". Unlike *M*, which is a Boson state, the nuclear charge $+q$ can be either a Fermion or a Boson. Hence the Fermionic and Bosonic statistics of $\vec{M}', \vec{M}''$ is broken and gives us the attracting effect on the massive "*q*" by a *V*(5) monopole-monopole potential well:

$$V(5) = -\frac{M'M''\mu}{r} \cong -\frac{[2ec]^2 N(+)N(-)\mu}{r} \tag{1.3}$$

with "*r*" fixed by *ct*, irrespective of whether *t* is fixed or not.

The term $(qv)^2$ can usually be neglected, as it is normally extremely small for the nucleus of *q* charge as $N(+)$ and $N(-)$ are canonical ensemble generated, temperature-dependent, large thermal quantities. As such *V*(5) is valid only for a macro thermal system, not the initial space dimension projections that created the basic leptons and hadrons, similar to the Perelman-entropy mapping. However when $q\vec{v}$ exist, the boundary conditions of $\vec{M}'$ and $-\vec{M}''$ are altered, and $\vec{M}'$ as well as $-\vec{M}''$ are no longer Bosonic and hence in the Bose condensate state.

It should be pointed out that due to the Pauli exclusion on the *e*-trino, anti-*e*-trino, the repulsive magnitude M^2 is given by the products of $(e, p) \times (-e, -p) \times (e, p') \times (-e, -p')$. Where (e, p) and $(-e, -p)$ represents the *e*-trino and anti-*e*-trino spinors with *p* and -*p* momentum, that is only radially outward, so sign cannot be changed. Note that *e*-trino state commutes with anti-*e*-trino states, while anti-commutes with another *e*-trino state. Thus

M^2 can be expressed as

$$\frac{1}{4}\left\{(e,p)\times(e,p')-(e,p')\times(e,p)\right\}\times\left\{(-e,-p)\times(-e,-p')-(-e,-p')\times(-e,-p)\right\}.$$

The e-trino and anti-e-trino pair states are Boson. But due to its antisymmetry form for arbitrary p and p', its thermal average has 0 net weight.

On the other hand the attractive monopole-monopole magnitude comes from the product between M and $-M$, where the $-M$ vector is obtained by interchanging e with $-e$ and vice versa in the definition of M giving by the radial current $2ec$. This change will no longer lead to the antisymmetry of the e-trino pairs and the thermal weight factor is not 0.

Since the 5D manifold irrespective of "t" is given by Fermat's sum, and with charge conservation, therefore irrespective of the 4D space as long as there is a finite size of the opening for the 1D subspace that allows for r along that 1D expansion, $N(+)=N(-)=N$. In other words, the monopole potential well becomes space inhomogeneous. In fact N would be proportional to the ratio of the solid angle "S" of the opening as compared to the spherical solid angle 4π, and is a linear function of the temperature, as M (having the unit of ampere-meter) represents a boundary-condition-dependent Bosonic state, with degenerate energy E. $V(5)$ is thus modified by $s=S/4\pi$. And for first order approximation we should modify $N(+)N(-)$ by $N(+)N(-)s$. And we can get from the Bose distribution the thermal number of such M states

$$N=a. \tag{1.4}$$

where a is derived from integrating the Bose distribution over $\dfrac{dE}{kT}$ from $\dfrac{h}{t}\left(\dfrac{n}{kT}\right)=C$, where n is an arbitrary number, such that at $t=t_o$, the time of the Big Bang, we have $\dfrac{nh}{t_o}=hv(o)$ which must exceed the rest energy of the quark rest mass energy $m(Q)c^2$, such that at least it is enough to create both electrons and protons and neutrons in the Lorentz boundary domain, while maintaining net charge neutrality. The higher the temperature T, the smaller will be C when $hv(o)$ is fixed, leading to a larger N number and thereby more massive particles created in the Lorentz boundary domain which implies in the nucleus more fusion, and in the stars and planets more mass, even implying a larger galaxy. Hence the quantity C corresponds to the chemical potential of the grand canonical ensemble. Should $t\to 0$, $C\to\infty$, $a\to 0$, implying without extra input of starting creation of the monopole potential fields at a finite initial $t(o)>0$ value, the homogeneous 5D manifold cannot have any M as well as Maxwell EM potentials, irrespective of the uncertainty principle, because there were no sources in the 5D manifold. However with $C>0$ and finite

$$N=\frac{4\pi kT}{h}\sum\nolimits_{j=1}^{\infty}\frac{e^{-jC}}{j}<\infty \tag{1.5}$$

where j is a positive integer.

This sum "*a*" is finite, and proportional to *T*, the absolute temperature, implying also that the quantum well cannot be completely cancelled by a finite number of + or − massive charges created. On the other hand, if the monopoles M and $-M$ are replaced by M' and $-M''$ the Bose statistic, and the Bose condensation is broken, similar to a physical feature employed by Higg's theory. With the quantum well potential completely changed by equal number of relativistic massive charges of opposite signs in the 4D Lorentz boundary domain.

The mass associated with the $+q = ne$ charge is not necessarily equal to that of the sum of $n-e$ massive spinors. Both masses from the 5D field theory are the result from space projection into 4D Lorentz manifolds via the space to time projection P_0, and the pure space dimension reduction projection from 4D to 3D through P_1 enacted during the creation of the 5D universe, at $t(o) > 0$ the instant of the Big Bang, when the monopoles must be created. It was assumed in the 5D book such projections will not happen again in later time [1]. The modification of the monopole M by the massive charge term $q\vec{v}$, changes the resultant monopole statistics and thus no longer can be in Bose-Einstein condensation, unless we transform to the stationary frame of the massive *q*. It is this frame transformation, that recovers the quantum well, thus brings on the total enclosure of the 5D by matter via nuclear fusion into a heavy nucleus and eventually with a 5D time frozen center void.

The difference between $\vec{M}'$ and $-\vec{M}''$ comes from the symmetric pairs of *e* and $-e$ within $\vec{M}$ and $-\vec{M}$ with different energy values partly converted into $q = +en$ massive nucleus of mass $m(+)$ or $n, -e$ massive electron spinors, with electron mass $m(e)$ via P_0 the 4th space component projection onto the time axis, mapping 5D into Lorentz 4D × SU(2), where SU(*n*) represents the semi-simple compact Lie Groups of *n*′ dimensions, and from $+e$ massive spinors [the proton] via P_1 the 4th space component onto the remaining 3 space components, making up the protons and neutrons of the nucleus, such that the proton is defined by the gauge confined u, u, d quarks, and the neutron as u, d, d quarks; where *u* is the $\frac{2e}{3}$ up quark, and *d* is the $-\frac{e}{3}$ down quark. Or breaking 5D into Lorentz 4D × SU(3). Hence $m(e)n \ll m(+)$ where $m(e)$ is the lowest energy state, the electron rest mass $m(e)$ as the nucleus creation takes far more energy than the n electrons creation from the energy of the homogeneous 5D Fermat energy-momentum manifold, breaking the quantum homomorphic $\vec{M}$ and $-\vec{M}$ distribution and the Bose-Einstein condensation over the 4D homogeneous space, as given by the third phase angle of 0 to 4π in the Fermat's representation. Such a breaking of the homogeneity of the 5D manifold must occur first before the deformation of the 5D space-time into separated 5D manifolds with separated 4D Lorentz manifolds in the topology of 3D space of doughnut shapes as given by the Perelman-Ricci flow mapping. In fact it is important mathematically to realize the change of $\vec{M}$ and $-\vec{M}$ along "*r*" of the 3D homogenous space to $\vec{M}N + q\vec{v}$ and $-\vec{M}N + q\vec{v}$, where the massive *q*

charge velocity $\vec{v}$ is an arbitrary 3D vector. This implies the resulting monopole current is no longer necessarily along "r" and will no longer obey Gauss Theorem. It is this feature that implies that the monopole vector potential must be expressed in a covariant representation due to the motion of the massive charge q, similar to the treatment of the Coulomb potential of a charge q. It is this correlation that leads us to the Riemannian curvature for the Lorentz space-time due to the dynamic distribution of masses within, even when these masses can be considered as charge-less on the classical scale, and as the monopole quantum well vanishes when s becomes 0, or by the change in frame to v, when

$$s[MN]^2 = [qv]^2 = [nev]^2 \qquad (1.6)$$

representing the charge neutral mass case when the simultaneous condition on both the positive q and negative $-ne$ massive charges having the same Fermat's amplitude value r, which is the quantum well "r". Since N is linear in T, hence the right hand side of (1.6) which includes v^2 must also varies as sT^2. When that happens, the charge neutral moving mass in the Lorentz 4D domain observes no monopole well effect, and the nuclear fusion ceased, and the remaining binding is replaced by the forming of atoms by Coulomb attraction between the nucleus and its orbiting electrons. But most important it gives us a relationship between how $s \to 0$ due to v^2 of the nucleons in the nucleus mass shell, forming the Poincare sphere, as evolved through the Perelman-entropy mapping. Using the expression for N as an infinite series sum as given by (1.5) the relationship between s and N, can be expressed as a double sum series equation

$$\sum_{j=1}^{\infty} \sum_{j'=1}^{\infty} \frac{s(j,j')}{jj'} e^{-(j+j')C} = K, \qquad (1.7)$$

where K is a constant.

As $\vec{M}$ and $-\vec{M}$ are by uncertainty principle required to be along the same vector $\vec{r}$ of the 5D manifold so that $V(5) = MA(4)$ is also a solution of the 5D metric operator, hence $s(j,j')$ must be confined by a gauge restriction of $\frac{hc}{M} = \frac{h}{2e}$, which defines a gauge loop and thereby the Boson field M can be decoupled by a gauge transformation. This loop integration requires defining a z vector direction, and coupled to the conversion of $\vec{M}$ and $-\vec{M}$ into 2 closed current loops of J or $-J$, where the magnitude J is still $2ec$, but is no longer of DLRO, and made of the pair e, pxr', s; and $-e, -pxr', s'$, and separated along z, in a 2D × 1D space representation, where the spins s, s' are not necessarily opposite, and the gauge loop radius that decouples M from A(4) for $r' < r$, the Fermat's amplitude. Such a single closed J loop also leads to $e, -e$ annihilation, unless J is split into 2 parallel but separated ec closed loops, which would generate a magnetic dipole field, and obeys Chern-Simons gauge, leading thus to a Perelman-Ricci Flow mapping.

Hence $s(j,j')$ has a solution depending on

$$e^{-(j+j')C}, \tag{1.8}$$

where the chemical potential C is a positive number. In fact C must be related to the q and $\dfrac{ne}{kT}$ the open 5D core of 2D radius "r'". This form of $s > 0$ corresponds to the Bose condensation of N being broken by the presence of $q\vec{v}$. Therefore the higher the 3D × 1D core temperature the more nuclear and electron matter will have to be created on the final closed shell.

Its relationship to N is the physics that basically gives us the Perelman-entropy mapping from the Perelman-Ricci Flow open doughnut Lorentz manifold into the closed Poincare sphere, when the isolated monopole no longer exist. This triple relation between $q = ne, \dfrac{v}{c}$ and N, a function of increasing temperature will result in a phase diagram for elements formed at T. Hence the complete periodic table is reached in cool systems. Thereby, the pure gravity field observed by the observer must be derived from the covariant Riemannian 4D space-time, chosen fixed by the rest frame of the observer fixed on the moving masses formed by elements that gives us the Newtonian gravitation potential of a stationary mass as derived from the curvature metric equation according to General Relativity.

As we mentioned without defining a $t(o) > 0$ for the Big Bang, the 5D homogeneous manifold contains no fields of any kind. Hence in the process of creation of the monopoles at $t(o)$, there must be the total energy conservation given by

$$\langle E \rangle + V(5) = 0 . \tag{1.9}$$

The quantity $\langle E \rangle$ represents the total ensemble energy of creating the monopoles $\vec{M}$ and $-\vec{M}$. It is easy to see that both terms in (1.9) are proportion to T^2. Hence the temperature of the manifold cannot be determined, by C and s.

2. The Force Equation in the Non-Homomorphic 5D Manifold within the Magnetic Monopole Attractive Quantum Well for a Massive + *q* Charge

The presents of $V(5)$ creates an energy sink in the 3D × 1D space of the 5D manifold, hence any matter in the 4D Lorentz boundary domain would be attracted towards the center of the 5D manifold, the 2D $r' = 0$, similar to the presence of a black hole in 4D General Relativity theory. But in 5D theory, matter cannot exist inside the 1D monopole subspaces. This requirement can be achieved if the matter in the Lorentz 4D boundary domain has an angular momentum L, such that as its distance $R > r'$ to the void deceases towards r', of the 1D M domain, its energy increases so that its momentum ρ increases, leading to a centrifugal outward force sufficient to counter the monopole quantum well attractive strength, by converting part of the energy carried by the $\vec{M}, -\vec{M}$ states along r into coherent rotating $e, -e$ massless counter L state around r' to the revolving mass L, via the reducing of the covering solid angle ratio *s*, eventually *s*

becomes 0, enacting the Perelman-entropy mapping in the maintaining of balance of net $L = 0$ as the monopole M's energy distribution in the homogeneous 5D is reduced to 0. This feature was discussed earlier by us [13] as the origin for Astro objects having self rotation.

As discussed in the introduction a single isolated $m(+)$ massive nucleus with charge "$+q$" within the non-homomorphic 5D manifold is subjected to the quantum approximate well given by $V(5)$, thus at a given time t, it must be governed by the force balanced equation, equivalent to the introducing of the Lagrangian for the Ricci-Flow mapping given by Perelmann [7]. In fact there are Two separate Ricci Flow directions: One from the split of the 2 in phase rotation states of the e-trino and anti-e-trino from $M + (-M)$ 'which carries energy outward along r' [note all M are outward radial vectors] into either Lz or $-Lz$ angular momentum as BE of the monopoles is broken; the other is from breaking a $M = 2ec$ into 2 separated and perpendicular to z' parallel closed loops of in phase current ec each due to gauge that changes M to give a dipolar magnetic field Hz', or $-Hz'$ where z' is not aligned to z of Lz'' in the 5D domain. The non-selected opposite states for angular momentum and magnetic field values are then replaced by the responses from the masses in the Lorentz boundary domain. Thus giving the force balancing equation:

$$\frac{qHv}{c} - \frac{m(+)v^2}{r'} + \frac{dV(5)}{dr'} = 0 \tag{2.1}$$

The first term is the Lorentz force, due to a H field generated by all the moving charges within the 4D Lorentz manifold on q, and including the dipolar field generated by the non DLRO closed J or $-J$ loops. The dipole H field obtained from J or $-J$ is then given by the loop currents thermal averaged over product of two Fermi distributions of e, pxr' and $-e, -pxr'$; [see Fung and Wong [14] on the Hz field of stars, JMP for details] the second term is the $+q$ nuclei with mass $m(+)$'s centrifugal force, arising from the outward spiral of $m(+)$ as its Lz' changes caused by a $-Lz'$ of pairs of e-trino and anti-e-trino in phase rotation within the 5D core; note z' cannot be aligned with Hz as it will lead to the e-trino, anti-e-trino annihilation, while the last term comes from the magnetic monopole quantum well, that the charge current "qv" was created via the dimension reduction projection. Thus the "$+q$" charge sign nuclei Fermat's amplitude "r'" is given approximately according to (2.1) by

$$r' = \frac{\left(m(+)c^2\right)\left(\frac{v}{c}\right)}{2qH}\left\{1 + \sqrt{\left[1 - \frac{4M^2\mu sN^2 qH}{\left(m(+)c^2\right)^2\left(\frac{v}{c}\right)^3}\right]}\right\}. \tag{2.2}$$

There are 3 variables, namely qv, r and H. Hence there is no unique solution to "r'".

But since r' must be real and positive, it means

$$m(+)c^2\left(\frac{v}{c}\right)^{1.5} > 2MN\sqrt{s\mu qH} \tag{2.3}$$

As $q = ne$ and $m(+) > m(p)n$ where $m(p)$ is the proton rest mass, due to neutrons within the nucleus. Thus we have

$$H < \frac{\left(m(+)c^2\right)^2 (v/c)^3}{4\mu q M^2 s N^2} \tag{2.4}$$

As $\frac{v}{c}$ according to special relativity is bounded by 1, the nucleus mass $m(+)$ and the nucleus r then dictates the upper bound value of the magnetic field H.

Thus since the nucleus $r' > 0$, and small, it has an upper bound value $H = \frac{m(+)c^2 [v/c]}{qN}$. As $N \to \infty$ as $C \to 0$ and M is in the Bose condensate state, $H = 0$. Even not in the condensed state H value is relatively low because of large but not infinite N when the Bose condensation is broken making nuclear fusion from single proton to nucleus with $n > 1$ possible. While there is in general no lower bound on H limitation which is also valid in stars and planets as r increases to astronomical value.

For the electron force equation solution we replace with $-e(-v)$ replacing qv and r' changes from (2.2) to

$$r' = \frac{\left(m(e)c^2\right)\left(\frac{v}{c}\right)}{2eH}\left\{1 + \sqrt{\left[1 - \frac{4M^2\mu s N^2 eH}{\left(m(e)c^2\right)^2\left(\frac{v}{c}\right)^3}\right]}\right\}. \tag{2.5}$$

It is obvious "r'" for electron is greater than "r'" for the nucleus with $+q$ charges, even if $\frac{v}{c}$ is the same. Condition on H with N given by (2.4) is modified to

$$H < \frac{\left(m(e)c^2\right)^2 (v/c)^3}{4e\mu s M^2 N^2}. \tag{2.6}$$

Since $\frac{v}{c} < 1$, H must be inversely proportional to N^2. But for the nucleus charge q, it is inversely proportional to nN^2. Thereby the dipolar magnetic H 1D field has to be weak in heavy nuclei. Furthermore, since H is the same for both, it follows that $m(+)$ must be proportional to $nm(e)$. It should be noted that the r' solution for the electron is outside the nucleus "r'" by orders of magnitude, which further reduces the mass ratio $\frac{m(e)}{m(+)}$. This extra ratio comes from the SU(3) Lie Group generators. Therefore for general "r" solutions exceeding that for the $m(e)$ solution given by (2.6) as N and n become very large, would result in the 4D Lorentz domain with charge neutral matter and then be-

comes the pure classical topological Perelman mappings derived from the 5D homogeneous manifold. In conclusion, the nucleons, proton and neutron masses are mainly due to quantum gauge confinement of the repulsive gluon potential generated by the intermediate quark currents [1]. While the binding of the nucleons to form heavy nucleus arises from the attractive mono-pole quantum well until the matter shell closes to complete a Poincare sphere, as s becomes 0, the quantum well disappears.

Astronomical matters, such as galaxies, stars and planets the above force balanced equations is not strictly applicable not because s becomes 0, but rather that we are in a classical gravity domain, where some physicists believe in the graviton theory, where all matters are formed by charge neutral atoms, as the time frozen void 3D × 1D way exceeds the dimension of atoms, and with N being an integer, gravity is quantized, in a way similar to photons. Where the Lorentz force and as the monopole potentials no longer apply for the charge neutral matter. None the less, we believe it is the replacement for the monopole attractive quantum well by the Newtonian gravitation potential in the rest frame of the neutral mass $m(+)+m(-)$, with the curving of the Maxwell 4 vector potentials acting on a combined massive large number of charges q, and -ne forming atoms and molecules in a pure 4D Lorentz domain as explained in section 1, as the open surface area S of the Gauss surface shrinks due to the closing by the mass shell around the 3D × 1D space void it must be considered multiplied together with the infinite N^2 magnitude of the monopole well, [see eq. 1.5] due to the lower limit in its energy spectrum when in the specific rest mass 4D Lorentz frame such that the monopole quantum well strength in the mathematical limit $s \to 0$, as $N \to \infty$ when $C \to 0$, such that the quantum well sN^2M^2 strength is replaced by the attractive Newtonian gravity potential with strength $GM(0)$ where G is the Newtonian constant and $M(0)$ the mass of the Poincare sphere. Hence with relative moving masses, as given geometrically as Poincare spheres, the gravity potential field from multiple masses must be derived from the curvature arising from the covariant mass frames creating the warping of the 4D Lorentz-Riemannian covariant space-time caused by the dynamic distribution of all these masses in relative motions within the 5D universe, a result discussed in Einstein's General Relativity. Such a non-linear gravity potential equation without the masses having 3D × 1D voids must then possess a singularity independent to the mass corresponding to the N divergence. In fact it can be easily seen physically from the exact $q\vec{v}+N\vec{M}$ and $q\vec{v}-N\vec{M}$ moving charge currents given in (1.3) as $q\vec{v}$, which is on the Lorentz boundary domain becomes comparable to NM in magnitude, that the approximated $V(5)$ is no longer valid, and the shrinking of the open Gauss surface because of the finite sizes of the matter composed of atoms such that the Perelman entropy mapping takes over and closes the mass into a Poincare sphere, the monopole strength will decrease to zero, breaking the Bose-Einstein condensate state. In another word, N is a decreasing function of s and the final Poincare mass sphere should

enclose a time frozen 3D × 1D void, such as that suggested by Wheeler's worm hole [15]. As s shrink to 0, the expanding M along $r = z$ is cut-off. Due to expanding energy continuity, M must be converted into a pair of 180 degree off-phase photons, which carry no E, H amplitudes as it propagates along z. Thus such a beam can be detectable from newly formed stars, and could be interpreted as a graviton beam [16]. In fact this topological mapping result not only removes the Schwarzschild singularity of gravity, but it actually removes the concept of 'black holes' in the 5D universe. The idea of black holes in the universe had gained a lot of fantasy among physicists [17]. Recently there is a report of a so called photo sighting of a black hole, if correctly verified which would have to be a V(5) according to the 5D theory. Within an enclosed Poincare sphere, the new quantum perpetual states within the 3D × 1D void are no longer in M states, rather they are massless spinor pairs that give angular momentum, thus creates a self rotation of the mass shell, and the closed J or $−J$ parallel loops breaking parity that gives a finite dipolar Hz field as J is split into 2 parallel ec loop currents along z' values according to CP and as we had discussed in previous papers ([14], Fung and Wong, JMP). The key to finding these states in thermal equilibrium is the energy cut-off value, that must be put into the Bose distribution of the M and $-M$ states as s decreases which in turn will reduce sN^2M^2 to a finite number proportion to $GM(0)$ thus producing in the mass $M(0)$ rest frame the Newtonian gravitational potential.

3. The Break of the Homogeneity of the 4D Space, into a Cylindrical Representation Plus the Bending of M' and $−M''$ Magnetic Monopole States in the Entangled 4th Space Variable with z and r of the 3D Cylinder Variables

To mathematically understand how the eigen solutions of revolving charge within a dimension reduced space can be equivalent to the revolving charge's mass will give us further understanding on the importance of the monopole quantum well effect on the 4D covariant Lorentz space time Riemannian curvature.

It was proposed by Perelman that the Ricci Flow topological mapping of the 5D homogeneous space-time would result in a non-homogeneous 4D Lorentz manifold, with the 3D space in the geometrical shape of a doughnut, with a center 5D open core, such that the 4th space coordinate 1'D is the space coordinate through the vector addition from open z axis through the doughnut core center and the closed changing r as a function of z, of the doughnut tube variable around the core. It is such a 4D Lorentz manifold that properly represents the 4D space-time of a galaxy, where all the stars, planets and meteors are contained. In fact such a mapping can be quantized during the absolute beginning of the 5D universe matrix, by employing the P_0 and P_1 projections from this 4th 1'D entangled space representation dimension onto the t and 2D coordinates via P_0 and P_1 mapping. By using a 2D × 1D × 1'D space symmetry representation, the 3D

Lorentz gauge invariance must now be replaced by the 2D Chern-Simons gauge [18] [19]. While the net outward $\vec{M}'$ and $-\vec{M}''$ can be viewed physically like currents, which included the nuclear and electron currents on Lorentz boundary due to $qv = nev$ and nev from the charge cancelling electrons forces causes the $\vec{M}'$ and $-\vec{M}''$ bending along the curving 1'D through the 3D doughnut open center.

Without considering $\vec{M}'$ and $-\vec{M}''$ on the curving portion, it is interesting to investigate the Hamiltonian for the electron eigenstates just around the core at $z = 0$. This Hamiltonian is in 2D, $\vec{M}'$ and $-\vec{M}''$ are reduced to only $\vec{M}$ and $-\vec{M}$ along up and down z and making the monopole quantum well $V(5)$ resembles that of the relativistic 2D hydrogen, with Coulomb like potential 2D monopole-monopole attractive potential $-4\dfrac{e^2 c^2 \mu}{r} = -4\dfrac{e^2}{\varepsilon r}$ due to $\varepsilon\mu = \dfrac{1}{c^2}$.

Although the monopole-monopole quantum well is expression wise equivalent to the Coulomb attractive potential of $-4e^2$, topologically it is totally different. Nonetheless the eigen solution of a revolving massive electron would satisfy the Chern-Simons gauge. In the 2D Coulomb potential the charges are massive and the positive charge $+e$ is the proton at the origin $r = 0$, while the much lighter electron is in a relativistic ground state orbit, with the binding energy precisely equal to the electron reduced mass energy. In the case of the 2D quantum well produced by M and $-M$ along z, the massive electron ground state binding energy must then be precisely 4 times the electron rest mass [19]. Therefore, we can interpret it as the 2D × 1D quantum well containing an orbiting electron with energy equal to $4m(e)c^2$ on the 2D Lorentz boundary, or in another word the parity broken mono pole well can be cancelled by an energy cut-off to the Bose distribution equal to 4 electrons mass. This same potential well binding if applied to that of a revolving nearly 2000 times heavier proton say would be in a 2D non-relativistic orbital state similar to that given by nuclear shell model. Actually as according to (1.3), there are 4 choices for the 5D conversion into 4D × 1D mapping, thus the N value for the u, u, d quarks that makeup the proton should be weighted by the 3 axis P_1 choices 4 × 4 × 4, a result that also generate the gluon field via gauge confinement that gives the major portion of the proton mass. Hence the monopole quantum well strength should be weighted by 64 for the quarks. Note that all M monopole states are charge neutral. Therefore if a $-e$ massless spinor is projected onto t, and becomes an electron, then one $+e$ must also be projected by P_1 to form a proton. Hence because of the 1D having a 4 fold choice, in terms of the quark rest mass derived from $m(e)$, must be 4 × 4 × 4 $m(e)$, which is roughly 32 MeV. This value for the quark rest mass agrees well with data fitting for the mesons and baryons to within error due to the relativistic modification on the quark constituent masses within each hadron [3] [4] [5]. The relativistic lowest ground state from such a 2D potential irrespective of the monopole or the equivalent Coulomb strength under Chern-Simons gauge gives the binding exactly equal to that of the electron rest mass without change in the electron statistic.

Hence here the 2D relativistic ground state of the monopole quantum well is

$-4m(e)c^2$. Thereby the total 2D hydrogen like quantum well after creating the electrons has no more energy [19], The mathematical derivation given in those papers are valid also for the mono-pole quantum well, illustrating the gauge effect on the P_0 projection of creating electrons in the presence of Perelman-Ricci Flow mapping. In short, the electron mass $m(e)$ is created by the 2D monopole-monopole attractive quantum well under Chern-Simons gauge transformation via the Perelman-Ricci flow mapping same as the P_0 projection from the 4th space component onto time, resulting in an electron placed within a 4D Lorentz manifold. This interesting approximate result implies that the $\vec{M}, -\vec{M}$ 1'D like currents would be continuously ejected from the doughnut 5D core of a galaxy, according to the 5D homogeneous energy-momentum metric, at $t = 0$, E and p are infinite, hence despite the creation of numerous galaxies from the Big Bang, the galactic center of the galaxy will still have infinite amount of energy to create $\vec{M}$ and $-\vec{M}$ magnetic pole currents radiating outward along the 1'D, although these $\vec{M}$ and $-\vec{M}$ energetic bosons will not be projected to form new $SU(2) \times L$ and $SU(3) \times L$ manifolds they can excite the leptons and nucleons causing ionization as well as nuclear fission, and any star system that spirally revolves outward on the Lorentz doughnut surface, would periodically receive these $\vec{M}, -\vec{M}$ high energy like monopole beams. Since, $\vec{M}$ and $-\vec{M}$ with high energies above the electron and quark mass must preserve the equal numbers of electrons and protons, causing atomic ionization and nuclear fission, which upon thermal cooling afterward can lead to new nuclear fusion and the changes in the element composition in its matter shell, it means a planet, like earth, which star the sun revolves on the 4D Lorentz doughnut manifold would necessarily encounters intense periodic cosmic storms from the galactic core, the period length is equal to the revolving period of the star around the galactic center, which normally would be of the scale of millions of years. Such intense ec loop currents around the galactic core creating Hz' tilted to the galactic plane [20] as it cannot be aligned to the Lz states discussed earlier in section 2, that causes the stars to spiral outward from the core, would create the radiation belts at z' equatorial plane that in turn produces huge magnetic and atmospheric storms as earth revolves around the galaxy and enters, exists the radiation belt that would in turn severely affects its climatic pattern, including active volcanic eruptions inducing continental shifts during the early years of the solar system when the density of charge particles was more intense and even "ice age", when it gets out of the belt, such effects are far more intense than any changes in the contend of green house gas, such as CO_2 within the planet's atmosphere. Due to this cosmic effect on our earth's climate exists, recent climate changes on earth as solely due to human created CO_2 effect cannot be considered as conclusive. In fact we can make a crude model on this effect. Let us say the galactic core system orbital radius around the Milky Way core is R, and its revolving speed is "w".

Then the approximate period $T(o) = \dfrac{2\pi R}{w}$. The sun is however on the surface of the galactic doughnut tube of radius "r", and inclined to the galactic plane with angle theta.

Then the position of the sun to the galactic core is

$$R' = R + r\sqrt{\sin^2\theta + (1-\cos\theta)^2} = R + r\sqrt{2(1-\cos\theta)} \tag{3.1}$$

There are therefore periodic effects based on the J currents loops emitted from the core's curvature creation of a tilted radiation belt energetic particle hitting planets like earth as it enters and leaves the belt.

First because the solar system spirals outward from the galactic core R is an increasing function of time. Thus for each orbital period, a change of the period of $DT = \dfrac{2\pi}{w}\dfrac{dR}{dt}$ occurs.

Second, the effect of the direct free charge radiation trapped in the galactic radiation belt created by the J or $-J$ closed loops around the core, which must not be aligned with Lz, the galactic angular momentum due to annihilation forbidden path overlap of the e-trino states. Hence solar activity occurs only if the galactic belt hits on the solar system, and in turn causes the solar radiation periods, which as compared to the spiral period $T(o)$ is

$$T'(o) = T(o)\left[\frac{r}{R}\right]\sqrt{2(1-\cos\theta)} \tag{3.2}$$

For the Milky Way $\dfrac{r}{R} \gg 1$, however for the sun, θ is a small angle [20]. Thus $T'(o)$ can be actually greater or less than the speed of the spiral of the stars in the Milky Way. Very likely such galactic influence on earth's climate change is of order of millions of year apart. Also because R and r actually expand with time the J effect decreases with each change, hence earth's historic known major climate changes must be more severe than any that comes now, and in the future.

4. The Boundary Effects on the *e*-Trino and Anti-*e*-Trino Pair States within a Poincare Sphere of Matter

In the previous sections, we studied the e-trino, anti-e-trino opposite momentum 1'D monopole currents which are created from energy in the 5D manifold. For any totally matter enclosed sphere, the time frozen spherical boundary imposed on these pairs states would necessarily convert the open $\vec{M}, -\vec{M}$ like magnetic currents into perpetual ec closed loops. The perpendicular axis z' to the closed ec loops cannot be in exact alignment to the in phase e-trino, anti-e-trino rotating perpetual pairs as we had mentioned in section 3, that would generate a self rotation of angular momentum Lz, as it will cause $e, -e$ annihilation due to $t > 0$ only in the 5D metric. This is clearly observed in stars and planets. In fact this same restriction must also happen with the ec closed loop states around the doughnut shaped galactic core. Take the Milky Way, as example, the closed ec loops, would then generate a dipolar magnetic field Hz', that is tilted to the galactic plane. Hence, all charges trapped within this Hz' field created by the closed ec loops around the galactic core will give raise to a tilted radiation belt as is well known in the Milky Way to astronomers [20]. Except these trapped charges cannot spiral into the poles, unlike those charged particles in the earth's radiation belt because of the non-symmetric gravity changes for

the doughnut geometry. It is this galactic radiation belt, that will periodically affects the periodic large climate change, such as ice age, on earth as the solar system rotates in and out of the belt around the galaxy. In the closed matter sphere, pure radial *M* within the 3D × 1D time frozen void can no longer exist due to the reflective *M* state leads to annihilation of the massless spinor pair. Hence if such a time frozen core retains a lot of energy, at thermal equilibrium given by Temperature *T*, and if its equivalent energy density is higher than the dense quark mass then it will continue to create mass from formation of nucleus and electrons on the inner mass shell surface, until the core *T* is too cool to create more mass. We can treat the nuclear and electron mass formation on the inner surface of the astronomical void as if given by the magnetic monopole well in a local scale with open 5D topological representation, hence *N* in (1.5) is given by *T* derived from the *M* states Bose distribution. In another word, the 5D Fermat's sum can be expressed in energy-momentum, with energy via concept of entropy further replaced by temperature. Since currents also cannot cross, due to the annihilation of the $e, -e$ pairs, hence such closed *J* and $-J$ loops can only be on parallel and separated configuration as discussed in section 1. It is the closed *J* loop feature that make *M*, the monopole resembles the individual poles of a magnetic dipole [14]. Furthermore, the dipolar magnetic field Hz' generated will further requires that they be separated into north and south magnetic hemispheres due to the split of *J* along *r* into two *ec* parallel closed loops separated along z'. Thus all such spherical objects will carry a dipolar Hz' field. Though the Hz' field strength depends on the energies carry by these ec loops is not restricted. Hence dipolar magnetic field is always found in stars and planets. Not all energy within the 3D × 1D void is carried by the *ec* loops, we still have the pure non-charge angular momenta states carried by the $e, -e$ parallel in phase rotating pairs. Such pairs cannot be producing an angular momentum parallel to Hz'. In fact there is no alignment relationship. Of course, since the total 3D × 1D void including the matter shell cannot have a residual angular momentum as it is created from a 5D homogeneous manifold, it means the actual matter shell must provide the exact reverse angular momentum. It is this physics that makes stars and planets having a self rotation. We have published two detail papers on the data of stars and planets [13] [14]. Astronomical bodies like our moon, appears not to have a self rotation, and a dipolar H field. According to the Poincare sphere model, such an object, our moon must have a very cool or very small 3D × 1D void or both. Because of that, the moon could have been initially ejected from the earth's crust with one side of its surface totally exposed to the solar wind radiation, hence has very different temperatures on the sun facing side to that opposite side. These conditions, make it unsuitable for life irrespective of its absence of an atmosphere and water. Other solar planets, except Mars are not within the life habitable solar radiation range, and therefore cannot sustain life, unless may be on their associated moons. Not all moons of planets are like ours. In fact, those objects could have a self rotation and might even sustain life, if it also receives enough photo radiation not just from the sun, but also from the

planet it revolves around to keep part of its surface temperature at least some time above water freezing. It is always human's goal to populate outer space. But so far, our best bet is Mars. Unfortunately, Mars has a thin atmosphere, without enough oxygen and nitrogen, plus surface water, though it is not lack of water within its crust, as it's averaged surface temperature is below freezing. If our theory on the *e*-trino, anti-*e*-trino states in the core of planet Mars is valid, there might be possibilities for human to correct the planet's environment so as to make it suitable for the survival of life? To design the engineering on its climate modification we need to first study the physics of nuclear fusion that naturally occurs in stars and planets.

5. The Nuclear Shell Model, Leading to Fusion and Fission

Nuclear shell model [21] is consistent with the 5D field theory, as we discussed in section 2. Since the nucleon binding within a nucleus arises from the nucleon capture by the monopole quantum well that obeys Gauss Law, the quantum states of the nucleus must then resembles those of the atomic Bohr model. To show that we start with the projection mechanism of creating electrons and quarks, the lowest gauge confined quark states that gives us a Fermion are the proton and neutron, with its mass mainly due to the gauge constrain on the triple tensor products of the Maxwell 4 vector potentials generated by the fractional charged quark currents, known in the Gell-Mann standard model as gluon fields. Since both quarks, and the Maxwell 4 vector potentials exist only in the 4D space-time domain, both the proton and neutron are gauge invariant and of purely matters within the Lorentz 4D domain, thus they can only exist in a shell that could enclose a time frozen void of 3D × 1D. Their presence breaks the parity symmetry of the monopole-monopole quantum well strength. Of course the dimension of such a void has no upper and lower limits. For example, the alpha particle is like the single proton, it cannot geometrically form a closed shell, and hence do not contain a 3D × 1D void. The lowest form of a nucleus with a perfect spherical void is carbon 12 [22]. In short, only large and heavy nucleus has such a void. It is therefore geometrically clear that heavy nucleus requires a very energetic 3D × 1D void, and are formed from the fusion of the lighter nuclei through the Perelman-entropy mapping, and in the quantum sense the present of $V(5)$ accompanied by parity breaking of the quantum well strength. The physical reason is because *e*-trino with energy less than the threshold energy of the bare quarks masses cannot be lost instantaneous as the heavy nucleus is formed, as it can only be lost through the annihilation of $e, -e$ pairs, and emitted as photons, or as a counter example, we consider a Bethe decay of a nucleus. In this case, the neutron is converted into a proton, and an electron is emitted. Such a process changes q in the nucleus, and thus $-\vec{M}$ and $-\vec{M}''$ of the quantum well, together with the Lorentz force due to Hz' that breaks parity thus must further changes the $\vec{M}$ and $-\vec{M}$ parity as mentioned in ref.2. Hence nuclear Bethe decay process violates parity [23]. Unless we have such a void to house extra nucleons, and reduces the energy within the quantum well, as discussed in the previous section, such heavy nucleus cannot be created. With the same argument a super heavy nucleus would house more $e, -e$ massless

spinors, which must be in states that give us angular momentum, and thereby the centrifugal force, that might not be possible to be contained within the void, thus leading to radiation and even breakup causing nuclear fission, as the nuclear shell binding for heavy nucleus is weakened by the proton-proton repulsive Coulomb potential as $\frac{N!}{2}$, where N is the atomic number of the nucleus. Leading to instability in very heavy elements, such as Uranium. In conclusion, fission releases energy from the nucleus, while fusion reduces the overall energy of the nucleus and stabilized the void containing energy. In fact this phenomena carries over to astronomical objects, such as the inner shell surface of stars and planets. Thus if we wants to increase the planet's core energy, we may employ a controlled triggered nuclear fission process, that does not activates the outward thermal pressure significantly unevenly through volcanic eruptions and blow up too much of the planet's crest, yet raising the core temperature hot enough to trigger the nuclear fusion by forming from the nuclear residual fragments from fission into more stable non radiative heavy elements, such as iron and noble metals. In so doing we not only can activate the e-trino, anti-e-trino in phase angular momentum value, but also a change in the planet's moment of inertia from the shell mass density change, which is accompanied usually also by chemically changing the surface elements and in its atmosphere. In turn would even allow for increase in heat retaining CO_2 green house gas, plus changes in oxygen and nitrogen composition due to decomposition of oxides and nitrates from the crest. And with water vapor if the surface is above freezing, after cooling creates surface water pools, forming seas and lakes and streams. To achieve a man make planet core temperature change via nuclear fission and fusion for example on Mars, [see recent news article on Mars.] require solving many technical problems. For example, how to send a carefully controlled nuclear fission device into the planet's core intact and then trigger it. If we can achieve and solve these technical problems, then perhaps, it is the best humanitarian reward we earned from our previous technological development on creating nuclear weapons?

6. Conclusion—The Mathematical Theorems

It is best to summarize the important mathematical theorems that are employed in the 5D theory we present in this paper. First and foremost, all homogeneous manifolds satisfy the Fermat's Last Theorem. So does the 5D. Second, all space and time measurements must obey the uncertainty principle, thus the Fermat's sum gives the same dimensional homogeneous quadratic operator, with only plane wave solutions. The boundary on such a homogeneous space-time manifold is a manifold that is one space dimension lower. Thus for the 5D homogeneous space-time manifold, it is the 4D homogeneous Maxwell manifold. It is this theorem that provides us with the 5th component vector potential, the magnetic monopoles. The Perelman-Ricci Flow Theorem allows for the connecting of 4D Maxwell domains into a Lorentz 4D doughnut domain, thus chopping the single 5D universe into interconnected tU3D × 1D space-time topology with the initial absolute zero magnitude point of the Fermat's sum into a line of zero dimension, similarly, with the energy-momentum metric, the initial

single infinite energy point from the original 5D into disconnected multiple zero spread points of infinite energy. These mappings are mathematically profound, because only 0 and ∞ can be divided arbitrarily into, no matter how many and remain exactly 0 and infinite. Lastly, if in each 5D manifold, t is fixed, then it follows the 4D space that is arbitrarily divided and separated into Poincare spheres with time independent voids of $3D \times 1D$. Such topological subspaces are obtained via the Perelman-entropy mapping. Such mapping must follow from the closing up of the connected doughnut 4D manifolds. However, none of these mathematical theorems can give us the space to time and space to space dimension reduction projections, as projection transformation has no inverse, and must be enacted, meaning that it can only happen by command, an implication similar to the creation of the 5D metric itself, coming from the universe creator.

## Acknowledgements

Conflicts of Interest

The authors declare no conflicts of interest regarding the publication of this paper.

References

[1] Wong, K.W., Dreschhoff, G.A.M. and Jungner, H. (2014) The Five Dimension Space-Time Universe—A Creation and Grand Unified Field Theory Model. Scientific Research Publishing, USA.

[2] Gell-Mann, M. (1964) *Physical Review Letters*, **12**, 155. https://doi.org/10.1103/PhysRevLett.12.155

[3] Wong, K.W., Dreschhoff, G.A.M. and Jungner, H.J.N. (2012) The J/Ψ Meson and the Missing Heavy Baryon Octet. ArXiv:1204.0238v1.

[4] Wong, K.W., Dreschhoff, G. and Jungner, H. (2012) *Journal of Modern Physics*, **3**, 1450-1457. https://doi.org/10.4236/jmp.2012.310179

[5] Wong, K.W., Dreschhoff, G. and Jungner H. (2015) *Journal of Modern Physics*, **6**, 890-901. https://doi.org/10.4236/jmp.2015.67093

[6] Perelmann, G. (2002) The Entropy Formula for the Ricci Flow and Its Geometric Applications. arXiv:math.DG/0211159 [math.DG]

[7] Perelmann, G. (2003) Ricci Flow with Surgery on Three-Manifolds. arXiv:math.DG/0303109 2003a [math.DG]

[8] Diklan, J. (2019) You Are Disturbing Me—I'm Picking Mushrooms! Academia.edu. Jan. 2019.

[9] Aczel, A.D. (1997) Fermat's Last Theorem: Unlocking the Secret of an Ancient Mathematical Problem. Penguin, London, 147 p.

[10] Maxwell, J.C. (1864) A Dynamical Theory of the Electromagnetic Field. The Royal Society Transactions, Volume CLV. Printed in: The Scientific Papers of James Clerk Maxwell (W.D. Niven), Two Volumes Bound as One, Volume One, New York, Dover Publications, Inc., 1890, 526. Also refer to J. C. Maxwell (1865) *Philosophical*

Transactions of the Royal Society of London, **155**, 459-512.

[11] Wong, K.W., Dreschhoff, G., Jungner, H., Fung, P.C.W. and Chow, W.-K. (2018) *Physics Essays*, **31**, 493-495. https://doi.org/10.4006/0836-1398-31.4.493

[12] Higgs, P.W. (1964) *Physical Review Letters*, **13**, 508. https://doi.org/10.1103/PhysRevLett.13.508

[13] Fung, P.C.W. and Wong, K.W. (2015) *Journal of Modern Physics*, **6**, 2303-2341. https://doi.org/10.4236/jmp.2015.615235

[14] Fung, P.C.W. and Wong, K.W. (2017) *Journal of Modern Physics*, **8**, 668-746. https://doi.org/10.4236/jmp.2017.84045

[15] Wheeler, J.A. (1955) *Physical Review*, **97**, 511-536. https://doi.org/10.1103/PhysRev.97.511

[16] Goldstein, A. et al. (2017) *The Astrophysical Journal Letters*, **848**, L14. https://doi.org/10.3847/2041-8213/aa8f41

[17] Chernyakova, M. (2019) *Nature*, **567**, 318-320.

[18] Yang, X.L., Guo, S.H., Chan, F.T., Wong, K.W. and Ching, W.Y. (1991) *Physical Review A*, **43**, 1186-1196. https://doi.org/10.1103/PhysRevA.43.1186

[19] Gou, S.H., Yang, X.L., Chan, F.T., Wong, K.W. and Ching, W.Y. (1991) *Physical Review A*, **43**, 1197-1205. https://doi.org/10.1103/PhysRevA.43.1197

[20] Chen, X.D., *et al.* (2018) *Nature Astronomy*, **10**, 1038.

[21] Goldhammer, P. (1963) *Reviews of Modern Physics*, **35**, 40-107. https://doi.org/10.1103/RevModPhys.35.40

[22] Wong, K.W. (1964) *Journal of Mathematical Physics*, **6**, 537.

[23] Lee, T.D. and Yang, C.N. (1957) *Physical Review*, **105**, 1671-1675.
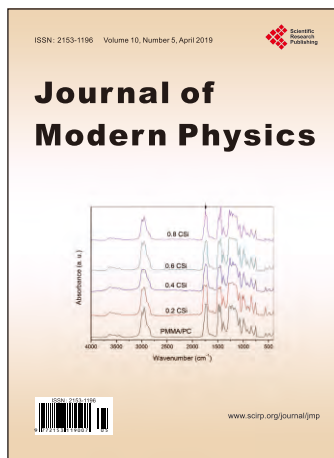
Journal of Modern Physics

Journal of Modern Physics (JMP) is an international journal dedicated to the latest advancement of modern physics. The goal of this journal is to provide a platform for scientists and academicians all over the world to promote, share, and discuss various new issues and developments in different areas of modern physics.

Editor-in-Chief

Prof. Yang-Hui He   City University, UK

Subject Coverage

Journal of Modern Physics publishes original papers including but not limited to the following fields:

Biophysics and Medical Physics	New Materials: Micro and Nano-Mechanics and Homogeneization
Complex Systems Physics	Non-Equilibrium Thermodynamics and Statistical Mechanics
Computational Physics	Nuclear Science and Engineering
Condensed Matter Physics	Optics
Cosmology and Early Universe	Physics of Nanostructures
Earth and Planetary Sciences	Plasma Physics
General Relativity	Quantum Mechanical Developments
High Energy Astrophysics	Quantum Theory
High Energy/Accelerator Physics	Relativistic Astrophysics
Instrumentation and Measurement	String Theory
Interdisciplinary Physics	Superconducting Physics
Materials Sciences and Technology	Theoretical High Energy Physics
Mathematical Physics	Thermology
Mechanical Response of Solids and Structures	

We are also interested in: 1) Short Reports—2-5 page papers where an author can either present an idea with theoretical background but has not yet completed the research needed for a complete paper or preliminary data; 2) Book Reviews—Comments and critiques.

Notes for Intending Authors

Submitted papers should not have been previously published nor be currently under consideration for publication elsewhere. Paper submission will be handled electronically through the website. All papers are refereed through a peer review process. For more details about the submissions, please access the website.

Website and E-Mail

http://www.scirp.org/journal/jmp   E-mail: jmp@scirp.org

What is SCIRP?

Scientific Research Publishing (SCIRP) is one of the largest Open Access journal publishers. It is currently publishing more than 200 open access, online, peer-reviewed journals covering a wide range of academic disciplines. SCIRP serves the worldwide academic communities and contributes to the progress and application of science with its publication.

What is Open Access?

All original research papers published by SCIRP are made freely and permanently accessible online immediately upon publication. To be able to provide open access journals, SCIRP defrays operation costs from authors and subscription charges only for its printed version. Open access publishing allows an immediate, worldwide, barrier-free, open access to the full text of research papers, which is in the best interests of the scientific community.

- High visibility for maximum global exposure with open access publishing model
- Rigorous peer review of research papers
- Prompt faster publication with less cost
- Guaranteed targeted, multidisciplinary audience

Scientific Research Publishing